Herbert Oertel
Sebastian Krittian

Modelling the Human Cardiac Fluid Mechanics

4th edition

KIT Scientific Publishing

Herbert Oertel, Sebastian Krittian

Modelling the Human Cardiac Fluid Mechanics

4th edition

Modelling the Human Cardiac Fluid Mechanics

4th edition

by
Herbert Oertel
Sebastian Krittian

KIT Scientific Publishing

Author

Prof. Prof. e.h. Dr.-Ing. habil. Herbert Oertel[1], Ordinarius
Dr. Ing. Sebastian Krittian[1/2]

[1] Computing Laboratory, University of Oxford
Wolfson Building, Parks Road, Oxford, OX1 3QD, United Kingdom

[2] Karlsruher Institut für Technologie, Institut für Strömungslehre (KIT)
Kaiserstr. 12, 76131 Karlsruhe, Deutschland

Impressum

Karlsruher Institut für Technologie (KIT)
KIT Scientific Publishing
Straße am Forum 2
D-76131 Karlsruhe
www.ksp.kit.edu

KIT – Universität des Landes Baden-Württemberg und nationales
Forschungszentrum in der Helmholtz-Gemeinschaft

Diese Veröffentlichung ist im Internet unter folgender Creative Commons-Lizenz
publiziert: http://creativecommons.org/licenses/by-nc-nd/3.0/de/

KIT Scientific Publishing 2012
Print on Demand

ISBN 978-3-86644-794-3

Contents

Preface

The fourth and final edition of this article on modelling and simulation of the flow in human hearts aims to supplement the previous and enclosed triology of the **Ka**rlsruhe **H**eart **Mo**del (KaHMo) by commenting on some long-term prospects of cardiovascular fluid mechanics.

Over a time-frame of more than one decade, KaHMo turned out to be a precise tool analysing the *status quo* of clinically relevant cases. Early heart models specified the movement of the active ventricle and its atrium by three-dimensional, time-dependent in vivo image data from nuclear spin MR tomography. The passive part of the virtual heart model has been represented by a model aorta and of two-dimensionally modelled heart valves. In order to understand ventricular function in more detail - and to allow for first *what-if* studies - an alternative fluid domain motion has then been introduced by a novel 'fluid-solid code-coupling approach'. In addition to treating the three-dimensional pulsing flow in the ventricle, this new method also calculated the active motion of the ventricular myocardium and its interaction with the flow. Both muscle fiber layers in the myocardium and its constitutive response has been taken into account. The flow resistance of the circulation through the body has been represented by a simplified circulation model. Based on these assumptions, virtual heart models can now be used to predict flow losses and flow structures due to pathological ventricle contraction defects.

Finally, we also want to discuss the opportunities related to 'integrative multi-physics approaches'. Leading edge research and technology cannot be based on particular research or national area any more; it must be multi-physics, inter-disciplinary and cross-national. We want to present some encouraging examples of integrated cardiovascular fluid mechanics, and discuss potential benefits to future cardiovascular research and the wider bio-medical community. With this final work we aim to share our vision of integrated computational simulation models across multiple disciplines of cardiovascular research, and emphasis yet again the importance of

Modelling the Human Cardiac Fluid Mechanics

within the framework of the international **STICH** study (**S**urgical **T**reatment of **I**schemic **H**eart **F**ailure).

Sebastian Krittian
Karlsruhe & Oxford 2011 Herbert Oertel

1 Introduction

Statistically, cardiac disease is the major cause of death in the western world. To improve diagnosis and therapy methods in the field of surgical failure treatment, the Institute for Fluid Mechanics, University of Karlsruhe, in cooperation with the Department of Cardio-Vascular Surgery, University of Freiburg, has developed KAHMO (**Ka**rlsruhe **H**eart **Mo**del), a patient-specific model of the human heart (Oertel et al. (2004), (2005), (2006), (2011), (2009), Doenst et al. (2009), Krittian et al. (2009), (2010a), (2010b), Schenkel et al. (2009), (2010)).

To predict the flow in the human heart, we need to model the time-dependent geometry of the ventricle, the atrium and the cardiac valves during one cardiac cycle. In the literature many approaches to modelling the electro-mechanical pump behavior of the heart are found (Fung (1997)). The structure of the muscle fibers of the human heart was published by Robb and Robb (1942) already in 1942. Hunter et al. (1996), (1998), Nash and Hunter (2000) developed a finite elasticity theory and a finite element method for analyzing ventricular electro-mechanics during the filling phase of the cardiac cycle, when cardiac muscle cells are not actively contracting. The orthotropic properties of the passive tissue are described by a constitutive law whose parameters are derived from a model of collagen fibers and in vitro stress measurements on animal hearts. A model of the active tissue properties, based on isolated animal muscle experiments, is also introduced in order to predict distributions of principal strain at the end of the contraction phase of the cardiac cycle. The mathematical modelling of the electrical activity of the heart has been summarized in the book by Pullan et al. (2005).

The calculation of the flow-structure coupling of the heart was introduced by Peskin and McQueen (1997), (2001). It approximates the muscle fibers of the heart as well as the cardiac valves in the Lagrangian description by considering discrete elastic fiber filaments embedded in the flow. The discretization of the fiber filaments is chosen to be so fine that they have no volume or mass, but can still be used for a continuum-mechanical description of the material. At each point of the filament-flow combination, a unique fiber direction is given. The degree of detail of the model structure is very high, and in particular the structure of the cardiac valves is modelled very precisely. The method was further developed by Lemmon and Yoganathan (2000), and applied with a simplified model to the left ventricle of the heart for the filling phase of the cardiac cycle. Watanabe et al. (2002), (2004), Cheng et al. (2004) and Vierendeels (1999), (2000) choose another approach to the flow-structure coupling

of the heart, based on a simplified electro-physical and muscle contraction model. The coupling of the flow with the mechanical structure model of the cardiac muscle takes place via the pressure.

Ecabert et al. (2008) specifically addressed aims to improve the diagnosis, planning, and treatment of cardiovascular disease based on computational models. More recently, Nordsletten et al. (2009), (2010), (2011) developed a cardiac fluid-solid mechanics approach for the investigation of diastolic and systolic ventricular function based on a non-conforming monolithic finite element method. Based on these techniques Smith et al. (2011) presented first results on personalized and integrated cardiac care. All these ventricular flow simulations, however, are still based on myocardial models of in vitro animal hearts or on simplified tissue modelling. Therefore, the results are not transferable to the living human heart. With the experimentally validated Karlsruhe Heart Model KAHMO, we present a time-dependent geometrical model of the ventricle and atrium for a complete cardiac cycle. KAHMO is based on patient-specific nuclear spin tomography MRT image data. The averaged inflow and outflow rates through the valves are adapted to magnetic resonance flux measurements.

The method used for the KAHMO MRT ventricle model is independent of but similar in approach to those presented by Jones and Metaxas (1998), Baccanie et al. (2002), (2003) and Saber et al. (2001), (2003), who defined the boundary configuration for a flow model for the left ventricle. Nakamura et al. (2003) presented a similar approach on the basis of velocity measurements during filling of the ventricle made with Doppler CMD-echocardiography. The determination of three-dimensional velocity fields in the long-axis plane of the ventricle has also been carried out by Houlind et al. (1994), Kim et al. (1995), Kilner et al. (2000) and Long et al. (2003). Furthermore, Kim et al. (1995) quantified the left ventricle vortex seen during diastole. Walker et al. (1996) measured the three-dimensional velocity field in multiple planes in the human heart. Pedrizetti and Domenichini (2005) showed that the intake jet generates a ring vortex behind the annular orifice of the mitral valve. Due to lateral displacement of the valve from the ventricle axis and the movement of the myocardium, the vortex grows asymmetrically in time. This vertebration during diastole is described correctly in most of the papers. Yet, none of them mention from a topological point of view the three-dimensional saddle-foci flow in the apex of the ventricle. This influences the time sequence of the outflow jet through the aortic valve at systole and is one of the topics of this publication. The flow topology has been investigated in eleven MRT data sets of healthy and unhealthy human hearts. One of the healthy data sets is described in detail and acts as a reference for flow simulations of human aneurysm ventricle defects. This publication presents the results of patient-specific simulations before and after surgery and furthermore indicates the potential of application in clinical use with the correlation of the dimensionless

ventricle pumping work.

As well as the flow in the ventricle, the KAHMO FSI flow-structure coupled heart model, recently developed, also calculates the motion of the ventricle myocardium during one cardiac cycle caused by the periodic relaxation and contraction of the cardiac muscle. To do this it is necessary to derive an anisotropic material law for the muscle fiber densities. We follow the approach of Glass and Hunter (1991), which was expanded by Holzapfel at al. (2000) using the constitutive description for orthotropic materials. Patient-specific indications for the locations of the fiber layers have been obtained by Kim et al. (1995), Kilner et al. (2000) and Jung et al. (2006) on the basis of echo-Doppler and MRT phase mapping methods. Applied to fluid mechanics, this method can also be used to derive subject-specific pressure fields in order to optimise both fluid and solid mechanics boundary conditions as described by Krittian et al. (2011).

The software used for the interface code-coupling approach requires a partitioned iterative coupling method. This method has been developed by Krittian et al. (2009), (2010a), (2010b) exclusively for the Karlsruhe heart model *KaHMo*. On the one hand commercial software packages show advantages in accuracy, speed and robustness. On the other hand, however, they also often represent a limiting factor for multi-disciplinary and multi-physics simulation of cardiovascular fluid mechanics. Open-source software frameworks (such as *OpenCMISS* described by Bradley et al. (2011)) allow a wide range of cardiovascular fluid mechanics analysis (e.g. shown among others by Krittian et al. (2011)) and will be able to perform whole heart cardiovascular simulations in the near future. The current challenge which is central to this project is to develop and effectively apply multi-physics solvers on high performance architectures such that they can address both scientific and clinical questions.

2 Anatomy & Physiology

2.1 Human Heart

The human heart of Figure 2.1 is a four chambered muscular organ that contracts and expands periodically while pumping 4 to 5 l per minute of blood into circulation. Returning from the systemic circulation, blood that is lacking in oxygen enters the right atrium and is passed on to the right ventricle to be delivered by contraction into the pulmonary circulation. The re-oxygenated blood returns to the left atrium and is passed through the left ventricle into the systemic circulation. To ensure that blood flows only one way and that the atria can be filled during contraction, four valves regulate the blood flow. These are located between the right atrium and the right ventricle (*tricuspid valve*), between the right ventricle and the pulmonary artery (*pulmonary valve*), between the left atrium and the left ventricle (*mitral valve*) and between the left ventricle and the aorta (*aortic valve*), respectively. Each valve has a set of flaps that open in only one direction due to pressure. The mitral valve has two flaps, while the others have three.

The pump cycle of Figure 2.2 is associated with changes in ventricular and arterial pressure, shown in Figure 2.3. As shown in the pressure-volume diagram, the cycle can be split into filling (1), isovolumetric contraction (2), expulsion (3) and isovolumetric relaxation (4). Phases (2) and (3) are known as *systole*, while phases (4) and (1) describe the *diastole*.

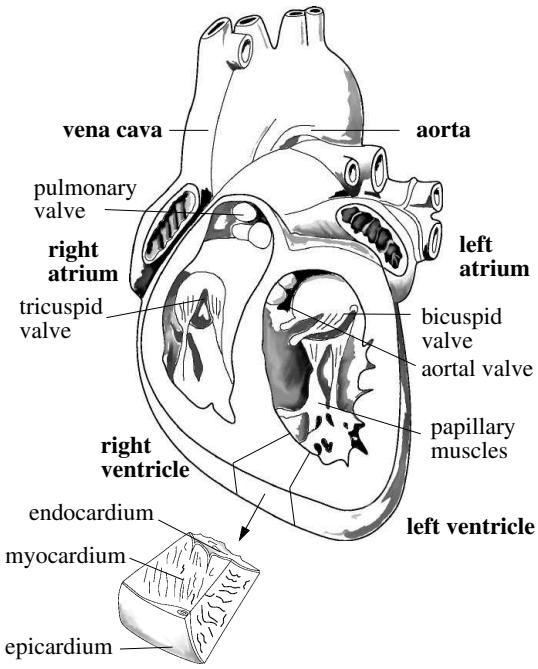

Fig. 2.1. Human heart

Owing to the slightly higher pressure in the left atrium than in the left ventricle, the mitral valve is open during the filling phase (1). While the ventricle expands and its pressure increases, the aortic pressure decreases continuously, corresponding with the blood flow in the arterial vascular system, but it still remains high enough that the aortic valve remains closed. With the start of contraction (phase 2), the ventricle pressure exceeds the atrium pressure, and as a consequence, the mitral valve closes. With both valves closed, isovolumetric contraction raises the ventricle pressure to 166 mbar, which exceeds the aortic pressure and forces the aortic valve open. Now a constant volume of 80 ml blood flows out into the aorta while pressure increases from its minimum value of 107 mbar to its maximum of 160 mbar. Due to relaxation (phase 3) the ventricle pressure drops again below the pressure in the aorta, and the aortic valve closes. Isovolumetric relaxation follows until the ventricle pressure

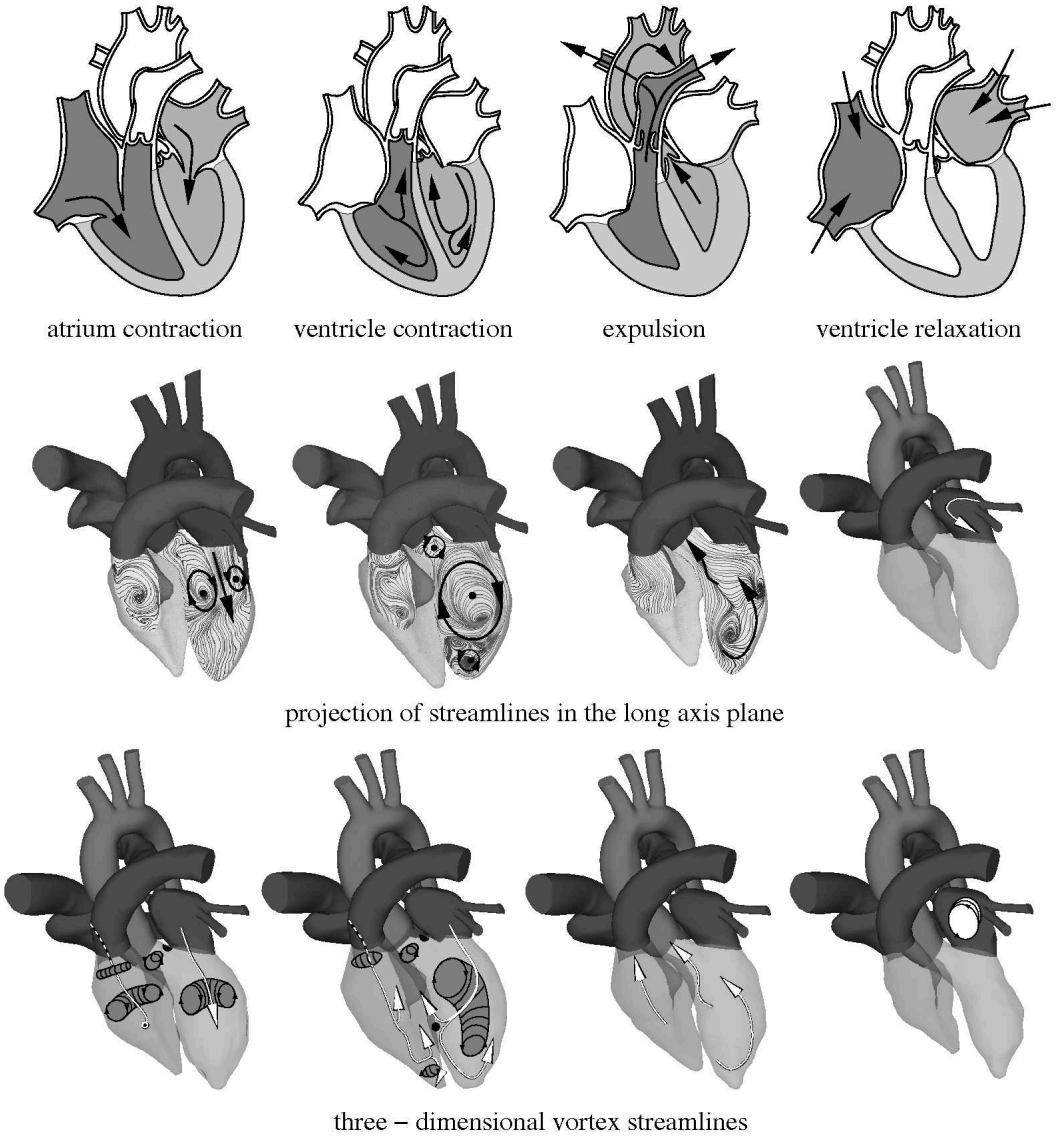

Fig. 2.2. Four phases of the cardiac cycle

is below the pressure in the atrium. The mitral valve opens and the cardiac cycle starts again. The pressure-volume diagram in Figure 2.3 shows the filling of the left ventricle.

The total volume of the heart is about 750 ml for a man and 550 ml ventricle volume for a woman. Using cardiovascular fitness training with the associated increase intake of oxygen during the load on the heart, the volume of the heart can made to increase to 1400 ml 1700 ml.

This can be expressed as a pressure-volume diagram. With increasing performance of the ventricle, the p-V curves are shifted to higher pressures and output volumes. They are bounded by the end-diastolic ED and end-systolic ES pressure-volume curves. The surfaces area within each p-V curve gives the work done by the ventricle. The *Frank-Sterling law* states that the work done by the ventricle increases with increasing filling volume of the ventricle. This is related to the mechanical properties of the cardiac muscle and permits the heart to continuously adapt to different positions of the body, efforts and frequencies of breathing.

The mechanical contraction of the cardiac muscle is controlled by periodic electrical impulses, which begin with excitation of the sinoatrial node. In its function as primary pace maker, the sinoatrial node sends cyclical electrical depolarization and polarization. During the depolarization phase, the discharge extends across the conduction paths with a velocity of 1 m/s into the surrounding muscles of the atria, which then contract. The electrical impulse of the sinoatrial node is delayed in the atrior ventricular node. This delay permits optimal filling of the ventricles during contraction of the atria. The impulse passes along the His nerve fibers and the sides of the chamber with a velocity of 1–4 m/s and reaches the ventricle muscles after about 110 ms. In the direction of the ventricle, the bundle of His divides along the left and right sides of the chamber.

As the ventricles begin to contract, the contraction in the atria ends, thanks to the delay of the conduction in the ventricular node. At this point all nerve cells in the impulse conduction system, apart from the impulse-forming cells in the sinoatrial nodes and the ventricular nodes, can be spontaneously depolarized. The depolarization of the ventricle shown in the electrocardiogram in Figure 2.3 takes less than 0.1 s.

The cycle of depolarization and polarization generates a small electrical potential which can be measured on the surface of the body. The depolarization of the atria causes a small deflection, called the P-wave.

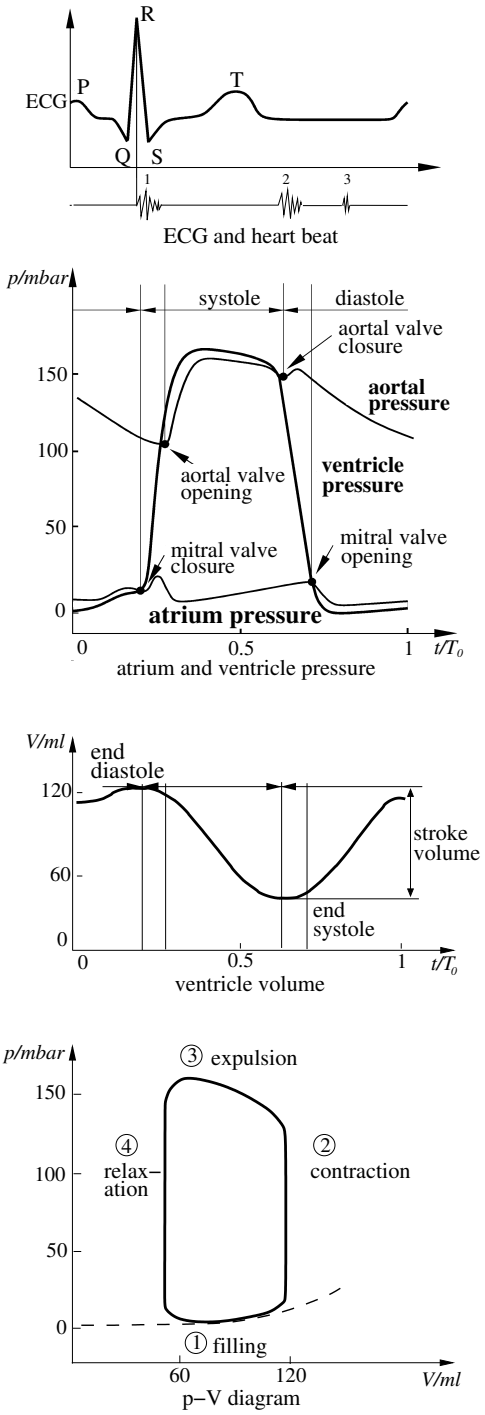

Fig. 2.3. Sketch of electrocardiogram (ECG), pressure and volume in the left ventricle, cardiac cycle $T_0 = 0.8$ s

After a pause of less than 0.2 s, this is followed by a strong deflection due to the depolarization of both ventricles (QRS). The T-wave then follows, caused by renewed polarization of the ventricles. The association of the electrical potentials with the mechanical processes and pressure changes in the left ventricle of the heart is also shown in Figure 2.3.

As the mitral valve closes, the pressure in the left ventricle rises. This is associated with a sound wave which is detected as the first heart beat. This induces the systole, the phase of ventricle contraction. At the second heart beat the aortic valve closes and the phase of ventricle relaxation begins. The third heart beat emanates from the sound wave of the filling process.

Figure 2.2 shows the three-dimensional flow in the ventricles and projections of the streamlines in the long-axis plane as well. As the mitral and tricuspid valves open, intake jets initially form during the filling process. These jets are accompanied by a ring vortex after one quarter of a cardiac cycle. These occur to balance out the deceleration of the intake jet in the fluid at rest. As the

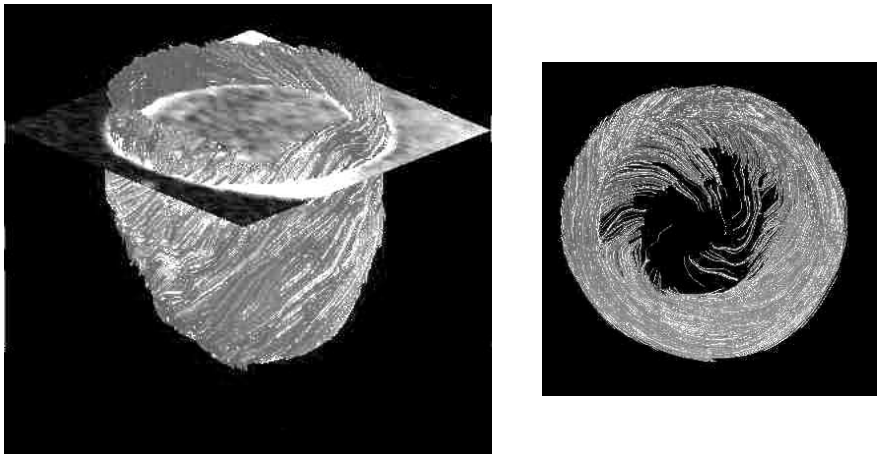

MRT – phase mapping – visualization, Jung et. al (2006)

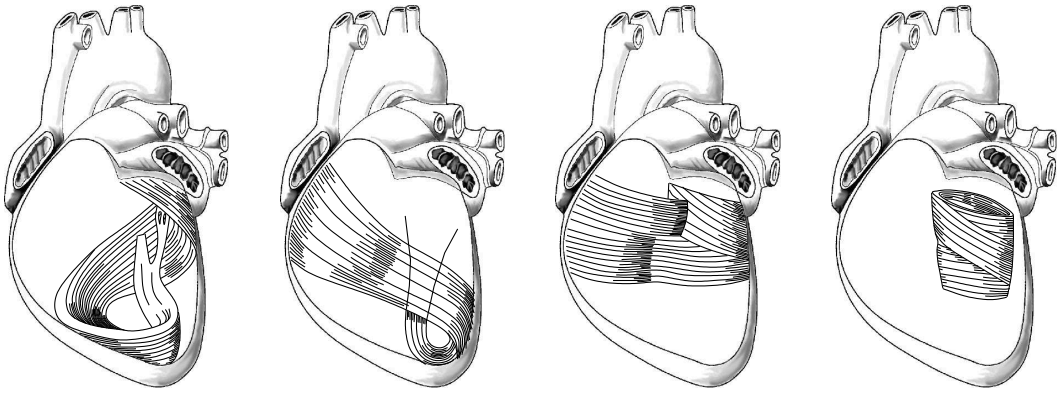

Fig. 2.4. Orientation of the muscle fibers of the heart

diastole continues, because of the motion of the cardiac myocardium, the ring vortex increases in size. The expansion of the vortex is uniform in the axial direction, but in the radial direction the left side of the vortex is strengthened. As the vortex moves into the ventricle, its velocity decreases. There is no flow through the apex of the ventricle at this time. As the intake process continues further, because of its strong deformation in the left ventricle, the ring vortex inclines towards the apex of the ventricle. As this happens the velocity of the three-dimensional flow decreases until eventually the intake process is completed and the mitral valve shuts. Further deformation of the vortex structure is determined by the inertia of the flow. In parallel, the upper part of the ring vortex induces a secondary vortex in the aortic channel.

As the aortic valve opens, the exit process into the aorta begins. The direction of motion of the vortex is sustained. First the vortex in the aortic channel is rinsed out and after that the ring vortex. The velocity maximum of the exit process is attained in the central region of the aortic valve and after 2/3 of the cardiac cycle the flow pulse in the aorta is fully developed. At the end of the systole the vortex structure in the left and right ventricles has completely dissipated. In a healthy human heart, about 62 % of the volume of the left ventricle is expelled during this process.

To calculate the interaction of the flow and the structure in the ventricle and atrium, a material law for the myocardium of the heart is necessary. The arrangement of muscle fibers and the lines of acceleration are shown in Figure 2.4. The muscle fibers are oriented in a spiral manner around the ventricle and cause radial and longitudinal contraction of the ventricle.

The qualitative shapes of the stress-strain curves of the human myocardium and epicardium are shown in Figure 2.5. The inner layer of the myocardium leads to different stress-strain behavior from that of the outer epicardial layer. In the myocardium there are different limiting values for the stress, depending

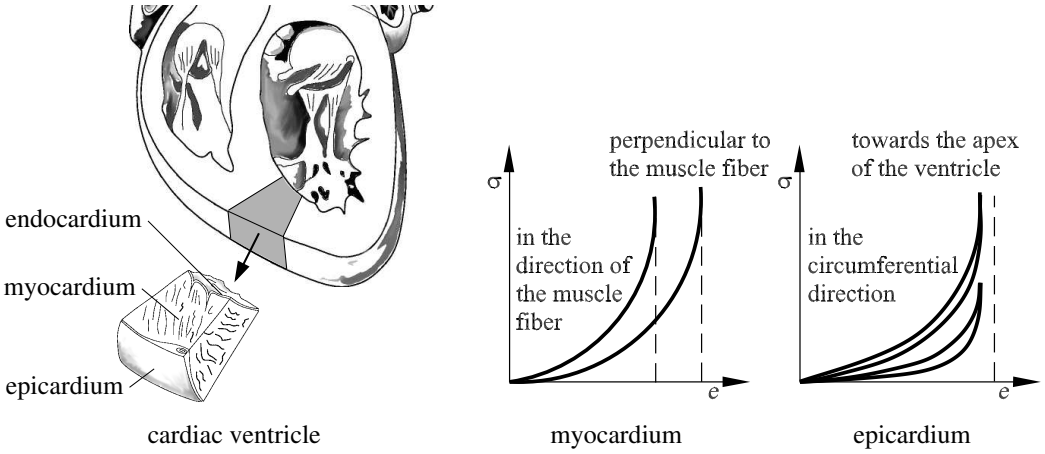

Fig. 2.5. Stress-strain curves for the human myocardium and epicardium

on whether the load is along the muscle fibers or perpendicular to them. The nonlinear stress-strain relationship exhibited by the epicardial layer is more pronounced than that exhibited by the myocardial layer. In addition, there is hysteresis in the load curve of the external muscle layer of the cardiac ventricle.

Nevertheless, in a limited region of the stress-strain curve, Hooke's law may be applied approximately, under the assumption of *orthotropy*. In addition to isotropy or transversal isotropy in a layer, orthotropy is a concept frequently used to characterize the symmetry of the material. As the name already implies, orthotropic behavior means different stress-strain behavior in three orthogonal directions. Thus, because of the radial orientation of the fibers, the axial stress-strain behavior is different from that in the circumferential and radial directions. In correspondence with Figure 2.4, three groups of muscle layers wind around both cardiac ventricles, while a further muscle layer winds only around the left cardiac ventricle. The cardiac muscle cells are oriented tangentially around the heart rather than radially. Orthotropic behavior may be approximately assigned to the various muscle layers.

2.2 Blood Circulation

The blood circulation of the human body is driven by the heart. With a power of only 1 W, the heart pumps about 4 – 5 l blood into the circulatory system every minute. If the body is undergoing strain, the pump power can increase to 20 to 30 l per minute. The blood circulation consists of two separate partial circulatory systems that are connected via the heart. One of the systems is called the systemic circulation, while the other is called the pulmonary circulation. The entire circulatory system assures gaseous exchange between the metabolism in the human tissue and the air in the atmosphere.

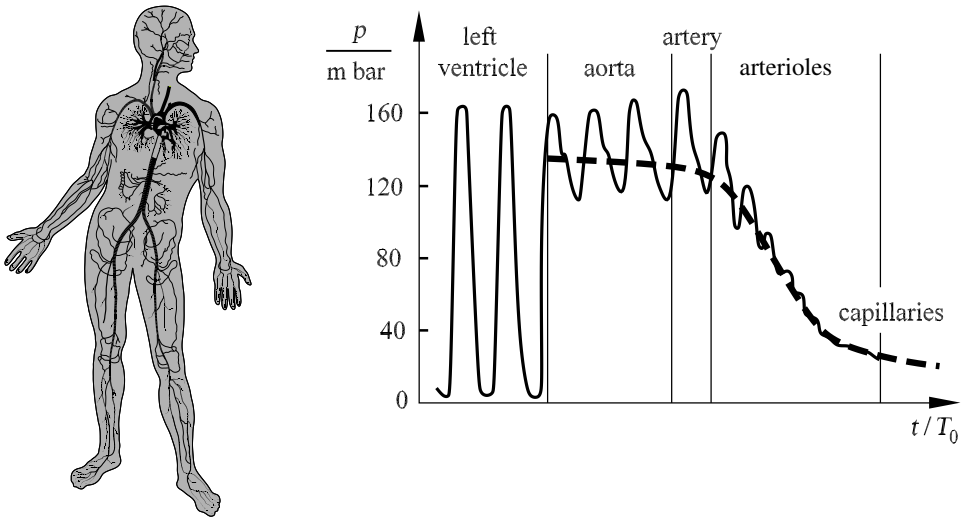

Fig. 2.6. Human arteries and pressure in the arterial circulation

The systemic circulation consists of the aorta, 159 arteries, 14 million arterioles, 4 million capillaries, 320 million venoles, 200 veins and the vena cava. The Reynolds number ranges from 3600 to 5800 in the ascending aorta, 1200 to 1500 in the descending aorta, 100 to 800 in the arteries, 0.1 to 0.5 in the arterioles, $7 \cdot 10^{-4}$ to $3 \cdot 10^{-3}$ in the muscle capillaries, 0.1 to 0.3 in the venoles, 200 to 600 in the veins, 600 to 1000 in the vena cava and 3000 in the pulmonary artery of the pulmonary circulation.

The volume fluxes of blood in the arteries are divided into 4% in the coronary arteries to supply the cardiac muscle, 14 % to supply the brain, 6 % in the arms and 4 % in the head region, 56 % in the stomach region and 16 % in the leg arteries. The circulation in the veins by volume is about 20 times larger than in that in the arteries and comprises 85 % of the volume of the blood.

The mean blood pressure on leaving the left ventricle is about 133 mbar. This drops to 13 mbar when the blood returns to the right ventricle. Figure 2.6 shows a sketch of the circulation in the arteries and the mean pressure and pressure variations in the different parts of the arterial circulation. Because of the elastic properties of the aorta, the pressure pulses between 120 mbar and 160 mbar around the mean value. In the large arteries, the amplitude of the pulsation initially increases, because of the wave reflection. It then sinks drastically to a mean value of 40 mbar in the arteriole region over a distance of a few millimeters. In the capillaries and venules, the pressure drop continues less sharply. Eventually there is a pressure of 13 mbar to push the blood back to the right ventricle. In the large veins and the vena cava, there is no pulse and no considerable pressure drop. Simultaneously pressure waves occur that are due to the pulsation of the right ventricle and move in the opposite direction to the flow of blood. The systolic pressure in the pulmonary arteries is quite small, about 20 mbar. A pressure drop of only 13 to 7 mbar is needed in order to overcome the flow drag in the lung, and so 13 to 7 mbar filling pressure remain for the left ventricle.

Because of their elasticity, the aorta and the large arteries act as a *volume reservoir*. The acceleration part of the blood pulse is reduced and a higher pressure level is retained during the diastole and systole. This means that the flow in the arterial branches is smoother.

Between each pressure pulse, the arteries contract by about 5% and so maintain the blood transport. The pressure pulse in the arteries is positive, even during the systole of the heart. In contrast, a backflow occurs in the large arteries for a short time. The flow velocity is zero as the aortic valve is closed. The amplitude of the flow pulse decreases with increasing arterial branches and the pulse width increases while a smaller backflow occurs. The forward motion of the pressure pulse through the arterial branches is initially associated with an increase in the pressure amplitude, which is caused by the

arterial branches and also by the decrease in elasticity of the artery wall. The flow profile in the branched arteries becomes more uniform.

The beating of the heart causes a periodic laminar flow in the smaller arteries and a transitional flow in the larger arteries and the aorta. The transition to turbulent flow takes place over a short time in the turning points of the velocity profile, close to the walls of the arteries. However, because of the shortness of the flow pulse the local transition to turbulence in the wall boundary layer cannot take place completely.

In the curved arteries and in particular in the aorta, the centrifugal force causes *secondary flows*. These have a velocity component perpendicular to the streamlines and cause a circulation flow in the direction of the outer wall. Figure 2.7 shows two snapshots of the velocity distribution of flow simulation in the bend of the aorta taking into account the centrifugal force, the streamline branching in the head, leg and collarbone arteries, and the flow structure of the secondary flow in the descending aorta. At the beginning of the systole, the flow first reaches a maximum at the inner side of the ascending aorta. After passing through the curved and branching region, the velocity maximum moves to the outer side of the aorta curve. Because of the centrifugal force, two secondary vortices arise that remain well into the diastole. Half-way through the cardiac cycle a radial evasive motion of the aorta can be observed. The point of maximum deceleration of the flow is passed through. The velocity profile then flattens and a first backflow is seen in the ascending aorta. Towards the end of the cardiac cycle the aorta has almost fully returned to its original state.

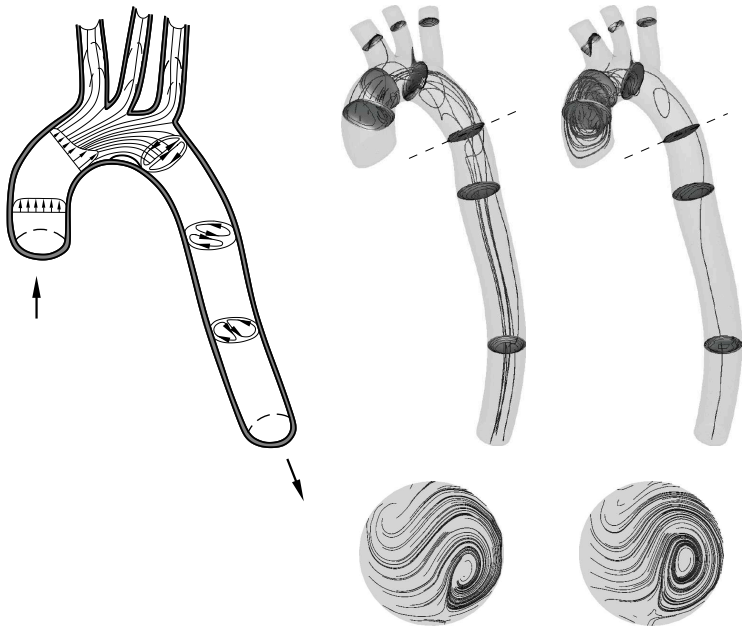

Fig. 2.7. Secondary flow in the aorta

2.2.1 Circulation Model

A model of the circulation flow is necessary for simulation of the flow in the heart. This should formulate the boundary conditions at the artery exits and the vein entrances of the heart model. The circulation model of Naujokat et al. (2000) takes into account the flow from the left cardiac ventricle into the aorta and into the attached arterial system of the body circulation, to the venous system, the right cardiac ventricle, the lung and back to the left ventricle. The circulatory system is divided into i elastic pipe segments. Within the framework of the electrodynamic analogy, whose basis was described by Guyton et al. (1972), the solution of the Navier-Stokes equation for the elastic pipe flow in each segment of the circulation model is found by associating the electric resistance, inductance and capacity with the physical properties of the arterial and venous branching and the rheological properties of the blood.

The circulation model computes the flow drag in the vessels as well as various parameters that influence the flow drag. The circulatory subsystem in the arteries is shown in Figure 2.8 and is represented as 128 segments. Each segment consists of a thin-walled elastic and cylindrical section of pipe, whereby each section of pipe, corresponding to human anatomy, is assigned a specific length, a wall strength, a specific diameter and a modulus of elasticity. Peripheral branchings of the arterioles and capillaries with a diameter of smaller than 2 mm are taken into account by means of a total peripheral resistance term.

The flow velocity u and the pressure p are represented by the electric quantities current and voltage, in analogy to the Navier-Stokes equations. Associated

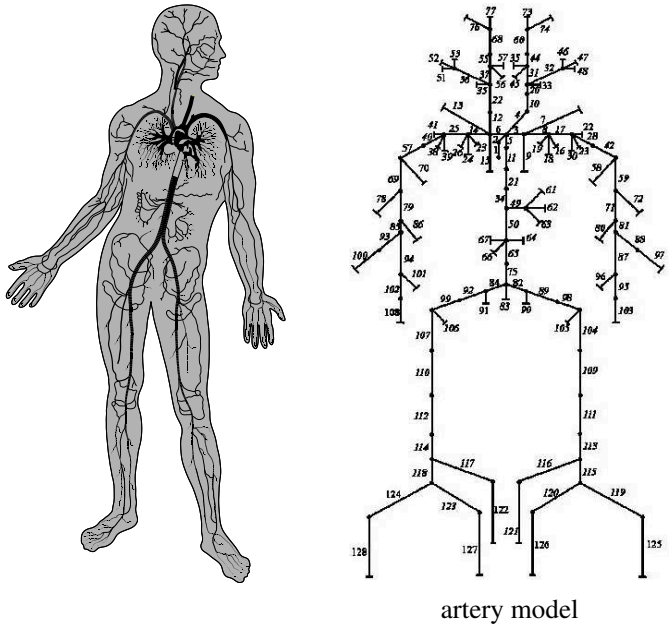

Fig. 2.8. Circulation model of Naujokat and Kienke (2000)

with the solution of the Navier-Stokes equations for the elastic pipe flow for each segment of the circulation model are the electric resistance, the inductance and the capacitance, corresponding to the physical properties of the arterial branchings and the rheological properties (e.g. the viscosity) of the blood. In analogy to the solution of the Navier-Stokes equation, for each section of pipe i the following ordinary differential equations hold for the blood pressure and the flow velocity:

$$p_{i-1} - p_i = \frac{9 \cdot \rho \cdot L}{4 \cdot \pi^2} \cdot \frac{\mathrm{d}u_i}{\mathrm{d}t} + \frac{4 \cdot \mu_{\text{eff}} \cdot L}{\pi \cdot R^4} \cdot u_i = I \cdot \frac{\mathrm{d}u_i}{\mathrm{d}t} + R_\Omega \cdot u_i \quad , \tag{2.1}$$

$$u_i - u_{i+1} = \frac{3 \cdot \pi \cdot R^3 \cdot L}{2 \cdot E \cdot d} \cdot \frac{\mathrm{d}p_i}{\mathrm{d}A} = C \cdot \frac{\mathrm{d}p_i}{\mathrm{d}A} \quad , \tag{2.2}$$

with the electric resistance R_Ω, the inductance I and the capacitance C. l is the pipe length, R the pipe radius, d the wall strength, ρ is the density of the blood and μ_{eff} is the blood viscosity. E is modulus of elasticity of the elastic pipe segment.

The circulation model assumes a pulsing flow through the circulation, whereby the intake flows after each segment branching are not taken into account. The flow pulse of the heart is replaced by a mean velocity in each segment. Figure 2.9 shows the calculated pressure curves in the aorta and the pulmonary artery for two cardiac cycles, which are used as pressure boundary conditions for the flow calculation.

The modelling of the vein and pulmonary circulations is carried out analogously, however with a lesser degree of detail. For the flow simulations the simplified circulation model of Reik et al. (2005) has been used, which is shown in Figure 2.10 as well 7 arterial and 4 venous elastic pipe segments which have been used for the flow simulation of the ventricles The intake and outlet pressures have been adapted with the patient specific blood pressure.

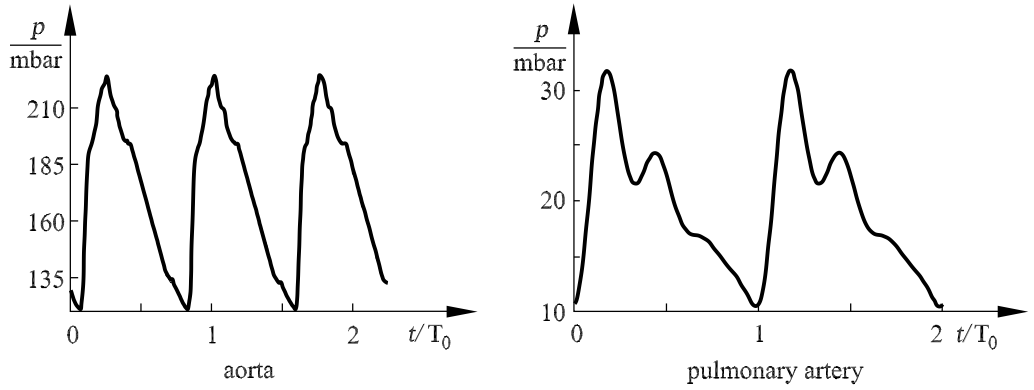

Fig. 2.9. Pressure curves in the aorta and the pulmonary artery, $T_0 = 0.76$ s

The circulation model of the previous section takes into account the blood flow in the large veins and arteries in which there is equilibrium between the pressure force, the inertial force and the forces of the elastic walls. At large Reynolds numbers the effect of friction is restricted to the wall boundary layers, which demonstrate an intake flow downstream following every branching of an artery or vein. With increasing branching of the circulatory system, the diameters become ever smaller, so that even for relatively short sections of vessels, a fully developed flow occurs. The inertial forces and centrifugal forces become negligibly small and the flow is determined by the equilibrium between pressure gradient and friction. These flow regime is called *micro-circulation*, and it makes up 80 % of the pressure losses between the aorta and the vena cava and is taken into account in the circulation model by means of a total peripheral resistance term.

Figure 2.11 shows the branching of the arterioles, venoles and capillaries in muscle tissue with a diameter less than $50\mu m$. The diameter of the subsequent capillaries lies between $10\mu m$ and $4\mu m$. In this region of the micro-flow the deformability in particular of the red blood corpuscles (erythrocytes) and the exchange of blood with the surrounding tissue has to be taken into account. The muscle cells regulate the flow in the capillaries locally.

The erythrocytes (Figure 2.12) have a biconcave shape with a diameter of

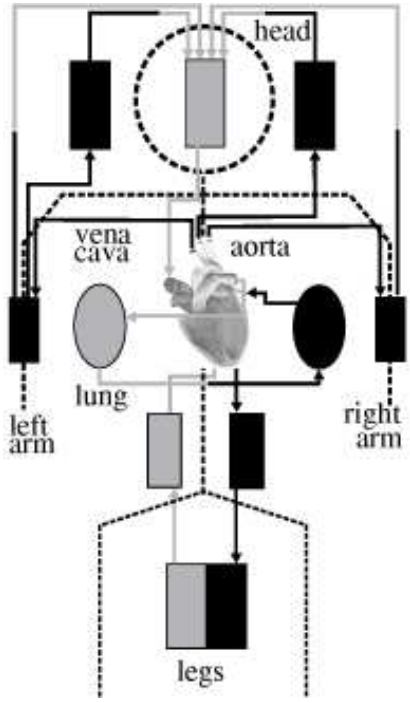

Fig. 2.10. Circulation model, Reik at al. (2005)

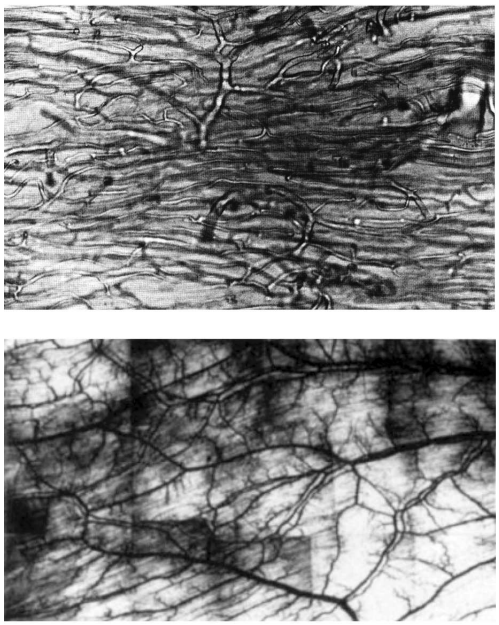

Fig. 2.11. Arterioles, venoles and capillaries in the muscle tissue

$8\mu m$. In the circulation they have a total surface area of 3750m^2. The capillary shown is filled with red blood corpuscles. Some capillaries are so small that their cross-section is smaller than a blood corpuscle. In order still to be able to pass, the red blood corpuscles deform. The oxygen transported by the blood corpuscles is delivered to the surrounding tissue via the finest capillaries. The deformation of the visco-elastic cell membrane in the fully developed shear flow of the capillaries depends on the pressure gradient and the geometry of the capillaries. Figure 2.13 shows the deformation of the erythrocytes and leucocytes in a capillary narrowing from 12 μm to 6 μm. The red blood corpuscles move faster than the blood plasma in the capillaries. A capillary branching leads to a further deformation of the red blood corpuscles.

To calculate the two-phase flow of the solid particles and the blood plasma flow in the capillaries, their interaction must be modelled. The homogeneous flow model assumes that mechanical equilibrium exists between the particle phase and the blood plasma phase. This means that the particles have the same velocity as the homogeneous phase. A transport equation that takes account of effect of the shearing in the Stokes flow is formulated for the change of particle concentration in the flow.

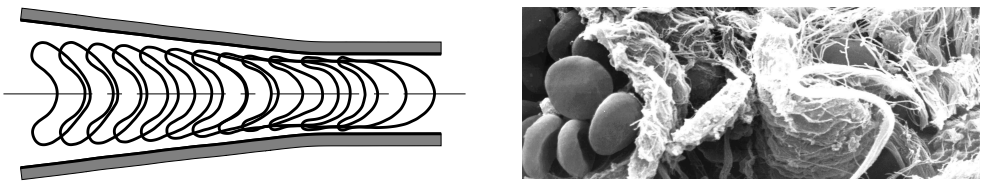

Fig. 2.12. Deformation of the red blood corpuscles in a capillary narrowing

The blood consists of blood plasma and the red blood corpuscles (erythrocytes), white blood corpuscles (leucocytes) and blood platelets (thrombocytes) suspended therein, which make up about 40 to 50 percent of volume. The blood plasma is the carrier fluid, which consists to 90 % of water, proteins, antibodies and fibrinogenes. Blood has the task of ensuring the supply to and the removal from the cells of nutrients, breathing gases, minerals, enzymes, hormones, metabolic products, waste products, water and heat. It serves as a transport system for the blood corpuscles, which guarantee the immune reactions of the body and the protection of the circulatory system from injuries.

For the flow in the heart and in the circulatory system, the flow behavior of the blood is important. In particular, it needs to be determined in which flow regimes and at which shear rates the Newtonian properties of the blood plasma, and the non-Newtonian properties of the suspension, need to be taken into account. These determine the resistance of the blood circulation that has to be compensated by the pump energy of the heart.

The blood may only be thought of as having a viscosity if the suspension occurs as a homogeneous liquid. This is true for blood in the large vessels. In the small vessels and in particular in the capillaries the elastic erythrocytes with their diameter of $8\mu m$ need to be considered as an inhomogeneity.

Although blood plasma consists to 90 % of water and can be treated to good approximation as a Newtonian fluid, the blood as a whole is a pseudo-elastic thixotropic suspension. The viscosity of the suspension depends on the relative volumes of all suspended particles. The largest part is made up of the

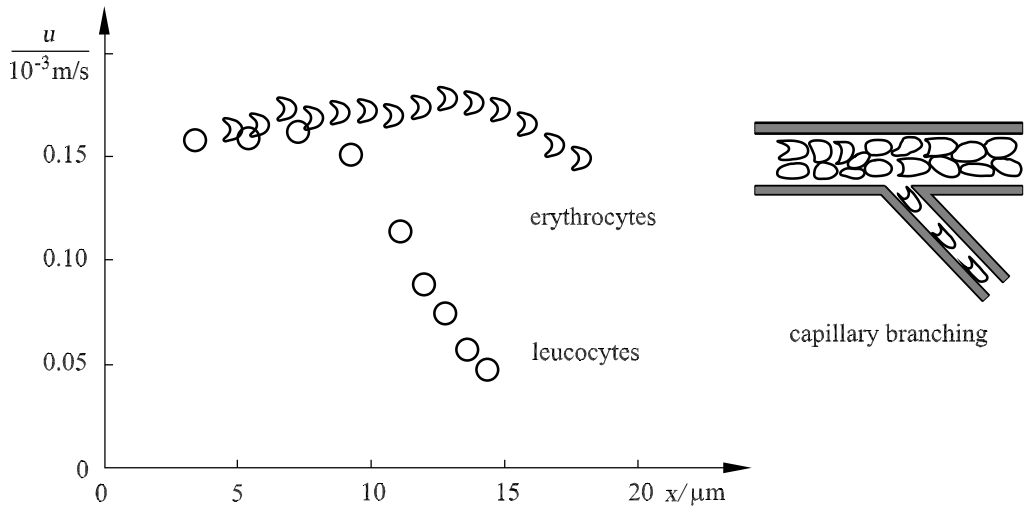

Fig. 2.13. Axial velocities of the red and white blood corpuscles in a capillary narrowing and a capillary branching

erythrocytes with 99 % volume of all particles, and 40 – 45 % volume part of the blood (hematocrit value). The thrombocytes and leucocytes make up less than 1 % volume part and have no influence on the rheology of the blood.

Figure 2.14 shows the dependence of the viscosity μ_{eff} of the blood on the shear rate $\dot{\gamma} = \nabla \mathbf{v}$. In the ventricle, the dominant component of the shear rate tensor has to be chosen for $\dot{\gamma}$. Over a wide range of varying velocity gradients, a drop in the viscosity of up to two orders of magnitude is noted. The region of velocity gradient in a healthy ventricle is in the asymptotic region where the viscosity is almost constant. For ventricle defects at very high velocity gradients and therefore very large shear stresses, there is a deformation of the erythrocytes, which itself affects the viscosity of the blood suspension. At shear stresses over 50 N/m^2, the erythrocytes begin to pull apart in a spindle-like manner. At shear rates of less than $1s^{-1}$, such as those which occur in the backflow regions of an unhealthy ventricle, aggregation of the erythrocytes occurs. The cells pile up onto one another and form connected cell stacks which are linked together. However, in a healthy ventricle no aggregation takes place. This is because the aggregation time is about 10 s while the pulse is a factor 10 shorter.

The dependence of the shear stress of the blood τ on the shear rate $\dot{\gamma}$ can be described to good approximation with the Casson equation

$$\sqrt{\tau} = \sqrt{\mu_{\text{eff}} \cdot \dot{\gamma}} = K \cdot \sqrt{\dot{\gamma}} + \sqrt{C} \quad . \tag{2.3}$$

Here K is the Casson viscosity and C the deformation stress of the blood. Fitting this equation to experimental results leads to the equation

$$\sqrt{\frac{\tau}{\mu_{\text{p}}}} = 1.53 \cdot \sqrt{\dot{\gamma}} + 2 \quad , \tag{2.4}$$

with the plasma viscosity $\mu_{\text{p}} = 0.012$ p. For shear rates larger than $100s^{-1}$ the blood behaves as a Newtonian medium.

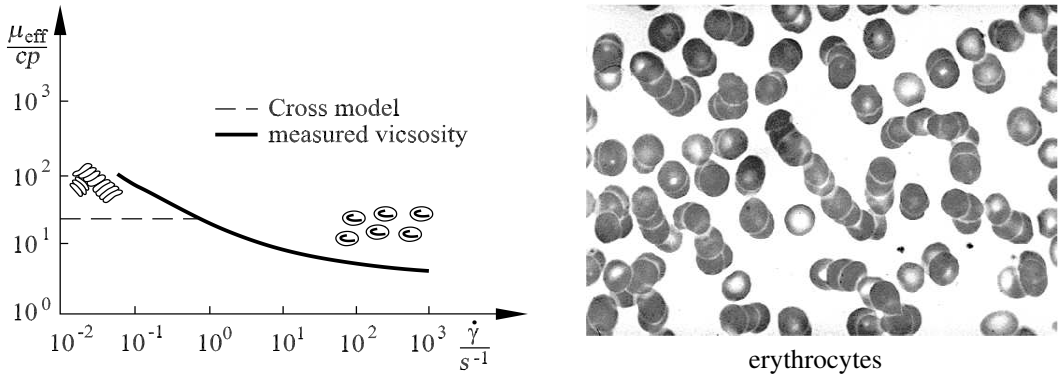

Fig. 2.14. Blood viscosity

In the flow through the vessels, the non-Newtonian properties of the blood lead to a decline in the erythrocytes close to the walls of the vessels and thus to a reduction in viscosity, which changes the velocity profile close to the wall and thus the resistance of the blood. The demixing close to the wall causes an almost cell-free plasma zone, which can be calculated with the plasma viscosity μ_{p}.

For the numerical calculation of the pulsing blood flow, the modified *Cross model* of Perktold et al. (1991) is used:

$$\mu_{\mathrm{eff}} = \mu_\infty + \frac{\mu_0 - \mu_\infty}{(1 + (t_0 \cdot \dot{\gamma})^b)^a} \quad . \tag{2.5}$$

The constants $\mu_\infty = 0.03$ p, $\mu_0 = 0.1315$ p, $t_0 = 0.55$ s, $a = 0.3$ and $b = 1.7$ are adapted to the experiments of Liepsch et al. (1992). Here μ_∞ is the limiting viscosity for large shear rates $\dot{\gamma}$ and μ_0 is the limiting viscosity for small shear rates.

The software for the calculation of the flow-structure coupling in the heart, KaHMo FSI, uses the so-called *Carreau approach* for the effective blood viscosity, which in the relevant shear rate region leads to the same result:

$$\mu_{\mathrm{eff}} = \mu_\infty + (\mu_0 - \mu_\infty) \left(1 + (t_0 \cdot \dot{\gamma})^2\right)^{\frac{n-1}{2}} \quad , \tag{2.6}$$

with $t_0 = 0.4$ and $n = 0.4$.

The viscosity of the blood μ_{eff} changes with the *hematocrit value* H of human blood. The hematocrit value is defined as the ratio of the volume fraction of red blood corpuscles to the total volume of the blood. For $H = 0$ the constant viscosity of the Newtonian blood plasma is found (Figure 2.15). For a hematocrit value $H = 45\%$ we obtain the curve of viscosity shown in Figure 2.14. For large values of the hematocrit value, the viscosity of the blood increases further.

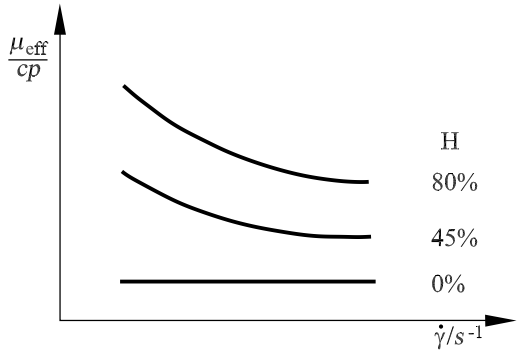

Fig. 2.15. Effect of the hematocrit value H on the viscosity of the blood μ_{eff}

Nature optimizes the transport of oxygen in the circulation and into doing so needs to harmonize two opposing demands. On the one hand a large hematocrit value is necessary to transport as much oxygen as possible, and on the other hand a small value is necessary so that the blood viscosity sinks and the volume flux in the vessels increases. Thus oxygen binding via as large a number of red blood corpuscles as possible is not the main aim. Of more importance is the optimization of the flow behavior of the blood, whereby it is necessary to transport a sufficiently large amount of oxygen without influencing the other blood functions too greatly. Corresponding to Figure 2.16, in the human body the maximum particle flux occurs for a hematocrit value of $H = 42\%$.

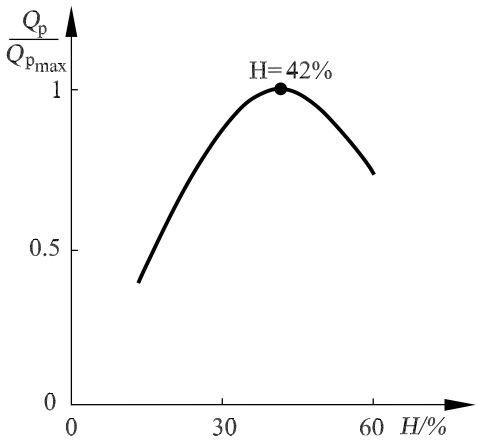

Fig. 2.16. Dependence of the particle flux $Q_p/Q_{p\max}$ on the hematocrit value H of the blood

3 Cardiovascular Flow Simulation

3.1 Continuum Mechanics

The calculation of the incompressible flow in the heart is carried out using the continuity equation:

$$\nabla \cdot \boldsymbol{v} = 0 \tag{3.1}$$

and the Navier-Stokes equation for laminar and transitional flow:

$$\rho \cdot \left(\frac{\partial \boldsymbol{v}}{\partial t} + (\boldsymbol{v} \cdot \nabla)\boldsymbol{v} \right) = -\nabla p + \mu_{\text{eff}} \cdot \Delta \boldsymbol{v} + \boldsymbol{f} \quad . \tag{3.2}$$

$\boldsymbol{f}$ is the volume force acting on the flow from the internal walls of the heart, $\boldsymbol{v}$ is the velocity vector and p is the pressure.

The non-Newtonian properties of blood are taken into account approximately with the Cross model (2.5) or the Carreau model (2.6).

The continuity and Navier-Stokes equations are made dimensionless with the characteristic diameter of the aorta D and the mean velocity U:

$$x^* = \frac{x}{D} \quad , \quad v^* = \frac{\boldsymbol{v}}{U} \quad , \quad t^* = t \cdot \omega \quad , \quad p^* = \frac{p}{\rho \cdot U^2} \quad .$$

Using the dimensionless characteristic Reynolds number $Re_D = U \cdot D / \nu_{\text{eff}}$, with $\nu_{\text{eff}} = \mu_{\text{eff}} / \rho$ from equation (2.5) and the Womersley number $Wo = D \cdot \sqrt{\omega / \nu_{\text{eff}}}$ ($\omega = 2 \cdot \pi / f$), we obtain the dimensionless equations:

$$\nabla \cdot \boldsymbol{v} = 0 \quad , \tag{3.3}$$

$$\frac{Wo^2}{Re_D} \cdot \left(\frac{\partial v}{\partial t} + (\boldsymbol{v} \cdot \nabla)\boldsymbol{v} \right) = -\nabla p + \frac{1}{Re_D} \cdot \Delta \boldsymbol{v} \quad . \tag{3.4}$$

The force tensor, which acts on the flow from the inner walls of the heart, is replaced in KaHMo MRT by the movement of the geometrical model and is calculated in KaHMo FSI with a flow-structure coupling model (see Chapter 4).

The equation of motion of the structure mechanics for the velocity of deformation v_{i} and the stress tensor σ_{ij} may be written:

$$\rho \cdot \frac{\mathrm{d}v_{\text{i}}}{\mathrm{d}t} = \rho \cdot \left(\frac{\partial v_{\text{i}}}{\partial t} + v_{\text{j}} \cdot \frac{\partial v_{\text{i}}}{\partial x_{\text{j}}} \right) = \frac{\partial \sigma_{\text{ij}}}{\partial x_{\text{j}}} + f_{\text{i}} \quad , \tag{3.5}$$

with the volume specific forces f_i and the density of the material ρ. The usual tensor notation has been used. Repetition of an index implies the sum over $\mathrm{i} = 1, 2, 3$ or $\mathrm{j} = 1, 2, 3$:

$$\frac{\partial \sigma_{\mathrm{ij}}}{\partial x_\mathrm{j}} = \frac{\partial \sigma_{\mathrm{i1}}}{\partial x_1} + \frac{\partial \sigma_{\mathrm{i2}}}{\partial x_2} + \frac{\partial \sigma_{\mathrm{i3}}}{\partial x_3} \quad ,$$
$$\frac{\mathrm{d}v_\mathrm{i}}{\mathrm{d}t} = \frac{\partial v_\mathrm{i}}{\partial t} + v_\mathrm{j} \cdot \frac{\partial v_\mathrm{i}}{\partial x_\mathrm{j}} = \frac{\partial v_\mathrm{i}}{\partial t} + v_1 \cdot \frac{\partial v_\mathrm{i}}{\partial x_1} + v_2 \cdot \frac{\partial v_\mathrm{i}}{\partial x_2} + v_3 \cdot \frac{\partial v_\mathrm{i}}{\partial x_3} \quad .$$

The total time derivative of the rate of deformation describes the change in a volume element $\mathrm{d}V = \mathrm{d}x_1 \cdot \mathrm{d}x_2 \cdot \mathrm{d}x_3$ that is moving with the flow. This representation is called the *Lagrange description*. The partial time derivative of the rate of deformation with respect to time and the convective terms differentiated with respect to the space coordinates is called the *Euler representation*.

For the flow-structure coupled calculation, the boundary conditions at the edges of the fluid space of the ventricle are formulated using the Lagrange representation, while the flow is calculated using the Euler representation. This leads to the *Lagrange-Euler formulation* of the fundamental equations for the structure and the flow.

The rate of deformation v_i:

$$v_\mathrm{i} = \begin{pmatrix} v_1 \\ v_2 \\ v_3 \end{pmatrix} \Longleftrightarrow \boldsymbol{v} = \begin{pmatrix} u \\ v \\ w \end{pmatrix} \tag{3.6}$$

corresponds to the flow vector $\boldsymbol{v}$. The stress tensor of structure σ_{ij} :

$$\sigma_{\mathrm{ij}} \Longleftrightarrow \tau_{\mathrm{ij}} \tag{3.7}$$

corresponds to the shear stress tensor of the flow τ_{ij}. Therefore the equation of motion of the structure mechanics (3.5) can be written as:

$$\rho \cdot \frac{\mathrm{d}v_\mathrm{i}}{\mathrm{d}t} = \rho \cdot \left(\frac{\partial v_\mathrm{i}}{\partial t} + v_\mathrm{j} \cdot \frac{\partial v_\mathrm{i}}{\partial x_\mathrm{j}} \right) = \frac{\partial \sigma_{\mathrm{ij}}}{\partial x_\mathrm{j}} + f_\mathrm{i} \quad , \tag{3.8}$$

and the Navier-Stokes equation of the fluid mechanics (3.2) can be written as:

$$\rho \cdot \frac{\mathrm{d}v_\mathrm{i}}{\mathrm{d}t} = \rho \cdot \left(\frac{\partial v_\mathrm{i}}{\partial t} + v_\mathrm{j} \cdot \frac{\partial v_\mathrm{i}}{\partial x_\mathrm{j}} \right) = \frac{\partial \tau_{\mathrm{ij}}}{\partial x_\mathrm{j}} + f_\mathrm{i} \quad . \tag{3.9}$$

For incompressible media, conservation of mass is identical for the structure

mechanics and for the fluid mechanics:

$$\frac{\partial v_{\mathrm{i}}}{\partial x_{\mathrm{i}}} = 0 \quad . \tag{3.10}$$

If we bring equations (3.8) and (3.9) together to a single equation, we obtain the *Euler-Lagrange formulation* of conservation of momentum for both the structure mechanics and the fluid mechanics in vector notation:

$$\rho \cdot \left(\left. \frac{\partial \boldsymbol{v}}{\partial t} \right|_G + ((\boldsymbol{v} - \boldsymbol{v_G}) \cdot \nabla)\boldsymbol{v} \right) = \nabla \boldsymbol{\sigma} + \boldsymbol{f} \quad . \tag{3.11}$$

$\boldsymbol{v}_G$ is the reference velocity of the moving surface and G denotes the associated reference surface that is moving in the Lagrange formulation. The fundamental equations of structure mechanics and fluid mechanics are given in the Euler formulation relative to this surface. This so-called ALE (**A**rbitrary **L**agrange-**E**uler) mixed Lagrange-Euler formulation has the advantage concerning the coupling of the structure mechanical and fluid mechanical fundamental equations via the Lagrange representation of the moving surface, that the various computational grids of each region on the surface G can be coupled. For the relative velocity $\boldsymbol{v} - \boldsymbol{v}_G$, the continuity equation $\nabla \cdot (\boldsymbol{v} - \boldsymbol{v}_G) = 0$ also holds.

In the ALE fundamental equation (3.11), ρ denotes the density of the structure and of the flowing medium. The tensor $\boldsymbol{\sigma}$ stands for

$$\boldsymbol{\sigma} = \sigma_{\mathrm{ij}} \quad \text{for the structure} \quad ,$$

with the associated ansatz for the stress-extension law, and

$$\boldsymbol{\sigma} = \tau_{\mathrm{ij}} \quad \text{for the flow} \quad ,$$

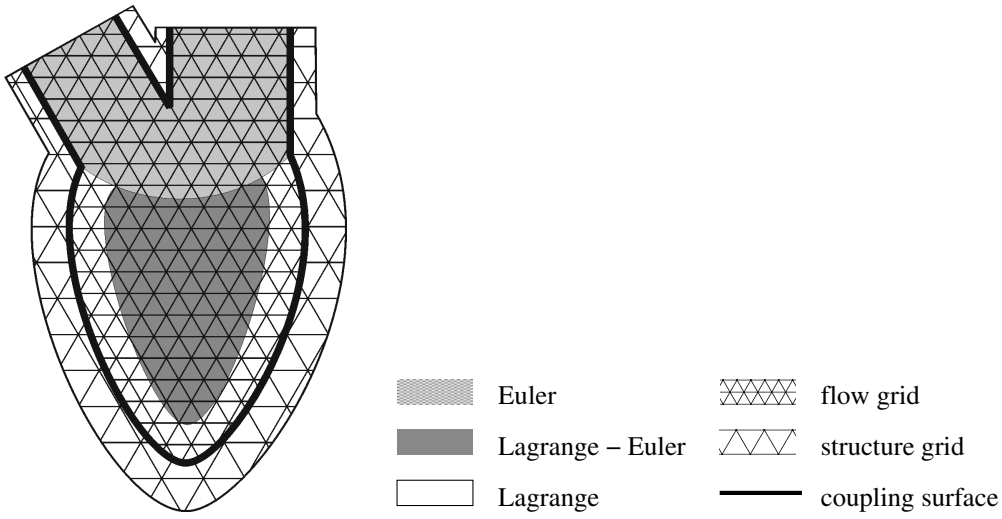

Fig. 3.1. Division of regions for the ALE Lagrange-Euler formulation of the flow-structure coupling for the human ventricle

with the Stokes friction law for incompressible flow

$$\tau_{\mathrm{ij}} = -p \cdot \delta_{\mathrm{ij}} + \mu \cdot \left(\frac{\partial v_{\mathrm{i}}}{\partial x_{\mathrm{j}}} + \frac{\partial v_{\mathrm{j}}}{\partial x_{\mathrm{i}}} \right) \quad . \tag{3.12}$$

The coupling takes place via the boundary conditions at the interface G. The kinematic coupling condition states that the rate of deformation v_{i} must be equal to the flow velocity $\boldsymbol{v}$ at the interface:

$$v_{\mathrm{i}}|_G = \boldsymbol{v}|_G \quad . \tag{3.13}$$

The dynamic coupling condition relates the stress tensor $\boldsymbol{\sigma}$ with the shear stress vector $\boldsymbol{\tau}$ at the interface with the normal vector $\boldsymbol{n}$:

$$\boldsymbol{\sigma} \cdot \boldsymbol{n} = \boldsymbol{\tau} \cdot \boldsymbol{n} \quad . \tag{3.14}$$

The exchange of stresses with the hydrostatic pressure and with the shear stress components of the friction is a matter for the coupling models.

For the flow calculation, as shown in Figure 3.1, three regions are to be distinguished. In the first region the motion of the coupling interface leads to a substantial Lagrange description of the flow quantities. The second transition

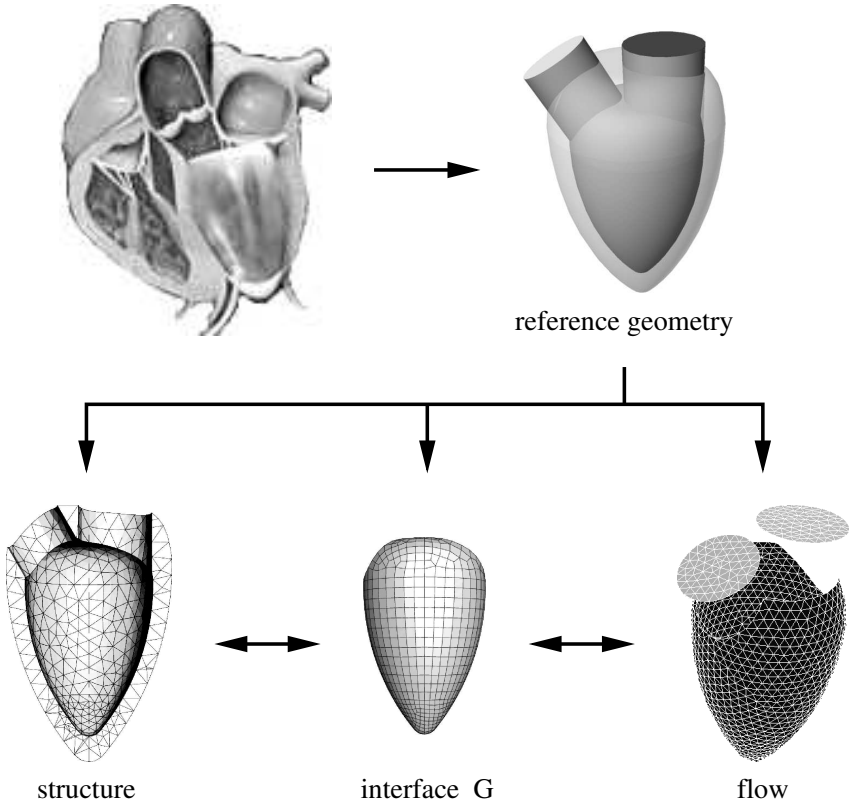

Fig. 3.2. Partitioned ALE coupling for a model ventricle

region requires a mixed Lagrange-Euler approach and at a sufficiently large distance from the interface in the third region the Euler formulation is used. Figure 3.1 shows the division of regions with a characteristic computational grid for the flow calculation of the human heart.

3.2 Code Coupling Interfaces

There are basically two different partitioned coupling strategies: explicit weak coupling and implicit strong coupling.

In *explicit coupling* at each time step of the numerical calculation the structure equation and the flow equation (3.11) are solved successively, and the kinematic coupling quantities (3.13) and the dynamic coupling quantities (3.14) are then exchanged at the interface G. In parallel coupling method neither the kinematic coupling condition nor the dynamic coupling condition are satisfied. In a serial coupling method at least one of the two boundary conditions (3.13) or (3.14) is satisfied. The numerical stability behavior of this explicit coupling method is certainly adequate for media of low density, however it reaches its limits for flows in liquids.

In *implicit coupling*, on the other hand, there is strong coupling of the structure calculation with the flow calculation. The coupling takes place iteratively at the interface G at each time step in the calculation, and satisfies the kinematic boundary condition (3.13) and the dynamic boundary condition (3.14). The disadvantage of the implicit coupling method is the considerable computational effort involved. For this reason, semi-implicit coupling methods are also used, in which the actualization of the coupling surface at each time step is restricted. In absolutely implicit coupling methods only one of the two coupling conditions is satisfied at the start, while the second coupling condition is

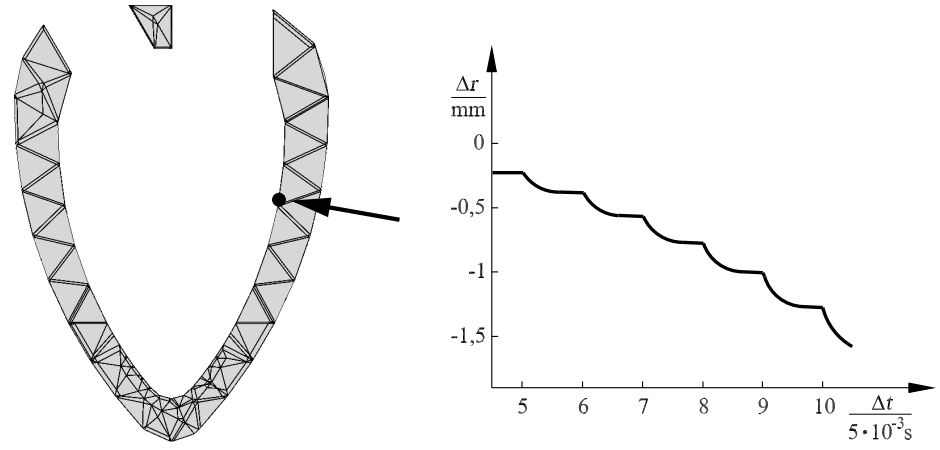

Fig. 3.3. Dependence of the motion of the interface on the time steps for implicit coupling

determined iteratively. The partitioned ALE coupling of Figure 3.2 is realized in KaHMo FSI.

Figure 3.3 shows the result of the iteration of the dynamic boundary condition (3.14). The plot shows how the radial change in position Δr of the interface depends on the time steps Δt of the numerical calculation. At each time step the correction in the position of the interface induced by the iteration can be seen.

Figure 3.4 shows the results of the structure and flow calculation of the filling and expulsion phases of a model ventricle for periodic relaxation and contraction. The upper picture shows the fiber distribution in the ventricle wall and the lower picture shows a cross-section of the resulting flow through the ventricle. All characteristics of the ventricle flow in the human heart as described in Figure 2.2 can be seen. The intake jet through the mitral valve causes the characteristic ring vortex, which moves into the apex of the ventricle as the ventricle continues to deform. When the aortic valve opens, the time ordered expulsion of the three-dimensional ring vortex takes place.

The numerical solution of equations (3.3) and (3.4) in KaHMo MRT is carried out using the finite volume method and the numerical model of Section 2.4. The flow calculation is performed using the Star CD software package (Com-

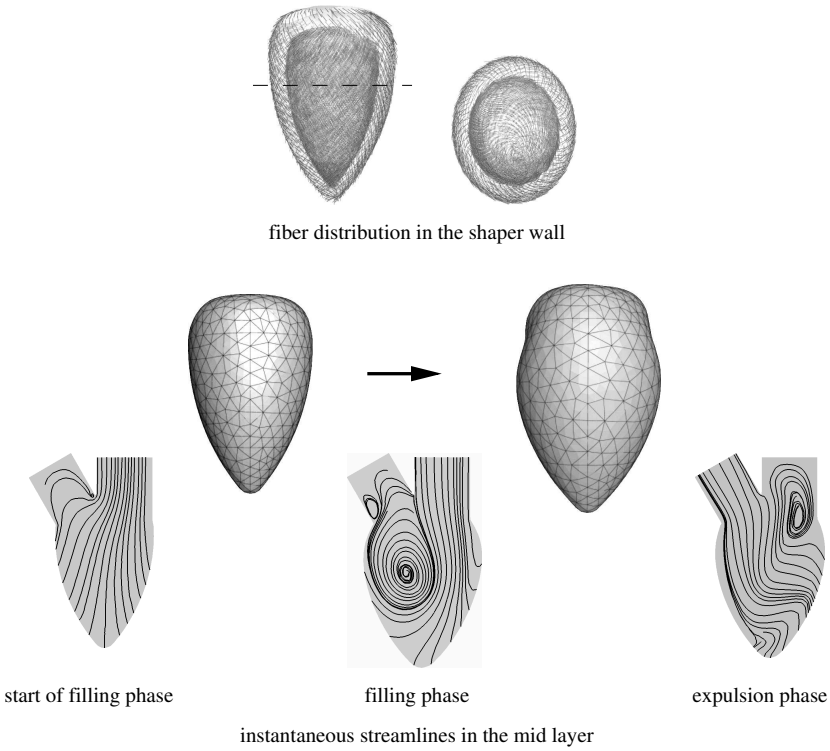

Fig. 3.4. Fiber distribution in the ventricle wall and flow images during the filling and expulsion phases

putational Dynamics Limited). It has been verified for numerous applications in fluid mechanics, especially for rigid and elastic pulsatile pipe flows, Oertel et al. (2011). The time discretization is performed with an implicit Euler method and a monotonic advection and reconstruction scheme. This second-order method is carried out in two steps. First, a field of monotonic gradients is defined, which together with the finite volume discretization guarantees a spatial second-order discretization. In the second step the fluxes through the volume cell surface for all advectively transported quantities are reconstructed from the quantities calculated in the first step by means of a monotonic and bounded advection scheme. In order to calculate the incompressible blood flow, the PISO algorithm is applied. This introduces a further equation to calculate the pressure field. The PISO algorithm is a predictor-corrector method that calculates the temporally implicitly discretized unsteady flow. The details of the temporal and spatial discretization may be found in Laurien and Oertel (2011).

In order to permit a flexible choice of software partners for the flow and structure calculation with KaHMo FSI, the coupling library *MpCCI 3.0* (**M**esh-based **p**arallel **C**ode **C**oupling **I**nterface) is used. This permits surface-based exchange of the coupling quantities on the common interface.

Using the finite-volume software *Fluent 6.3.26* for the flow and the finite-element software *Abaqus 6.7-1*, the explicit coupling is achieved in a standard manner. In line with the previous explanations, this approach is particularly suitable for incompressible flows through the *added-mass effect*. In order to avoid the associated instabilities, for KaHMo FSI an implicit coupling algo-

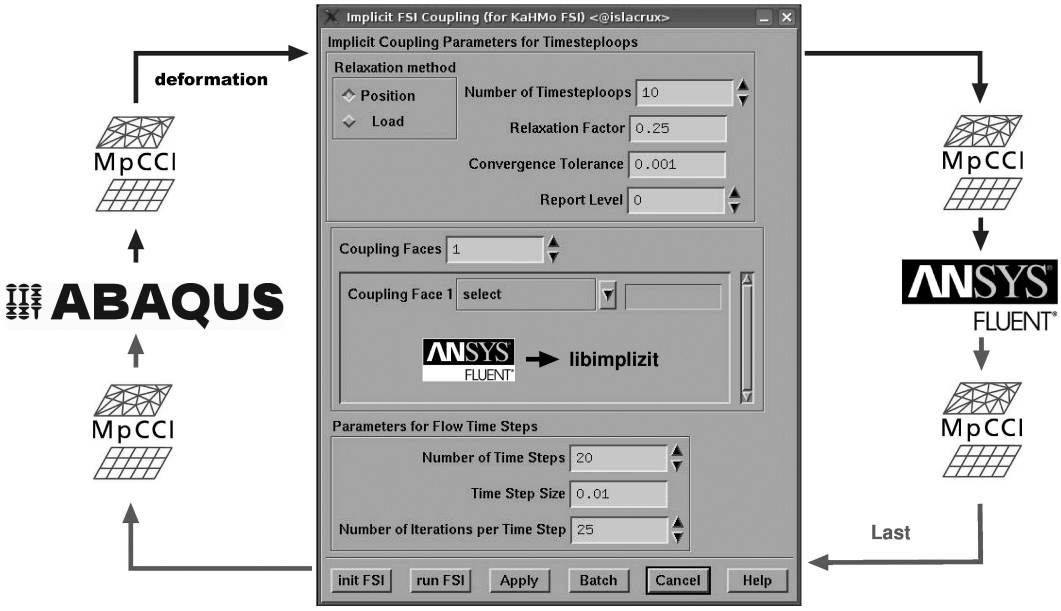

Fig. 3.5. Implicit KaHMo FSI coupling

rithm is realized that is particularly adapted for the demands of blood flow in the heart.

The coupling algorithm is implemented using the software package *Fluent*, in which, as shown in Figure 3.5, several loops are used within the partitioned coupling. *Fluent* calculates the flow and thus the loads acting on the interface, and *Fluent* also controls the relaxation process as well as the communication with *Abaqus* via the interface *MpCCI*.

The interaction of the *Fluent-MpCCI-Abaqus* software combination is synchronized by means of the coupling module shown in Figure 3.5. The input windows of this panel permit fast selection of a position or load relaxation method. At the start of the implicit coupling method, the maximum number of time step loops as well as the initial values of the relaxation factor and the convergence limit must be specified. In addition, the iteration specifications of the flow solver with the number of time steps, the size of time steps and the number of internal iterations can be given.

After selection of the corresponding coupling surfaces, the coupling is first initialized with *init FSI*. This assigns the exchange partners to the computational grids, which are generally discretized differently. The start of the actual coupling then takes place by executing *run FSI*. A *scheme file* provides overall control; this in turn accesses the C-programmed *relaxation unit (libimplizit)*. Exchange of the coupling quantities within the time step loops takes place via the MpCCI coupling library *libmpcci*.

Depending on the relaxation method, either the load quantity passed from *Fluent* to *Abaqus* is relaxed, or the returning information on the deformation is relaxed. As soon as the equilibrium state or the maximum number of time step loops is reached, the current time step is considered to be completed and the scheme moves to the next time step.

3.3 Integrative Multi-Physics

KaHMo represents a software-independent modelling tool for cardiovascular flow analysis. To date the underlying simulation work has been performed by commercial software packages due to their proven accuracy, speed and robustness. In terms of bio-physical model development, however, these software packages often show a lack of flexibility when integrating more aspects of cardiovascular function. Looking to the future of whole heart fluid mechanics, we understand that bio-medical-oriented software projects represent a valid platform to fill this gap. Increase in model complexity has driven a corresponding increase in the complexity of the computer codes which solve the models. As modern scientific modelling codes take a great deal of effort to develop, test

and maintain there has been an emerging trend towards collaborative efforts to develop software libraries which can be used by many groups. Although there is still some way to go, we want to express our optimism towards the idea of multi-disciplinary support of an open-source heart model. This would also allow a fluid-solid coupling inside the same computational environment. Depending on the specific case under consideration either partitioned or monolithic approaches may be preferred.

One promising software project for a wide range of bio-physical application is the open-source software platform OpenCMISS. Apart from full multi-physics coupled heart simulation, individual OpenCMISS modules can provide important input to other models like KaHMo (see e.g. Krittian et al. (2011)). The main goal of OpenCMISS, however, is to provide both the scientific and technological underpinnings of a modern software development approach to cardiovascular disease management through improving diagnosis, patient selection, and interventional planning. The description of the core computational engine of OpenCMISS as well as the integration of XML mark-up languages (CellML and FieldML) is presented by *Bradley et al.* (2011). The OpenCMISS code (www.opencmiss.org) has been developed by the authors over the last six years as a distributed-memory code to replace the shared-memory CMISS code that has supported a number of organ system physiome projects, including the cardiac physiome project and a number of similar projects on the lungs, digestive system and musculo-skeletal system. The design requirements for the OpenCMISS code are that it encompasses multiple sets of physical equations (such as finite elasticity coupled with fluid mechanics and reaction-diffusion) and that it links sub-cellular and tissue level biophysical processes into organ level processes. For example, the large deformation mechanics of the myocardial wall can be coupled to both ventricular flow and embedded coronary flow, and the reaction-diffusion equations that govern the propagation of electrical waves through myocardial tissue need to be coupled with equations that describe the ion channel currents that flow through the cardiac cell membranes.

4 The Karlsruhe Heart Model

The flow simulation in the left human ventricle, atrium and aorta are carried out using the KaHMo heart model (**Ka**rlsruhe **H**eart **Mo**del). The heart model is divided into the active part consisting of the ventricles and the atria; and the passive part with the aorta, vena cava and cardiac valves. The human circulation is taken into account with a circulation resistance and pressure boundary conditions of Section 2.2 at the atria, aorta and vena cava which have been adapted to MRT-flux measurements.

4.1 Multi-physics Modelling Approach

As there are only limited in vivo structure data of the human ventricle myocardium available, the KaHMo MRT model does not employ an active fluid-structure calculation in the ventricle, but rather uses instead in vivo measurements of the motion of the human ventricle with image data from nuclear spin MRT tomography. Figure 4.1 shows horizontal MR sections of a healthy human heart at a given point in time and the geometry model derived from it. The periodical geometrical model of the human heart is represented at each point in time by 23 horizontal and vertical sections. A cardiac cycle consists of 17 to 25 time steps with a respective time resolution of 32 ms to 45 ms of the MRT scanner. The geometry data of the periodic ventricle motion is recorded over several cardiac cycles and converted into a CAD geometry model. The trigger for recording the image takes place via the ECG shown in Figure 2.3.

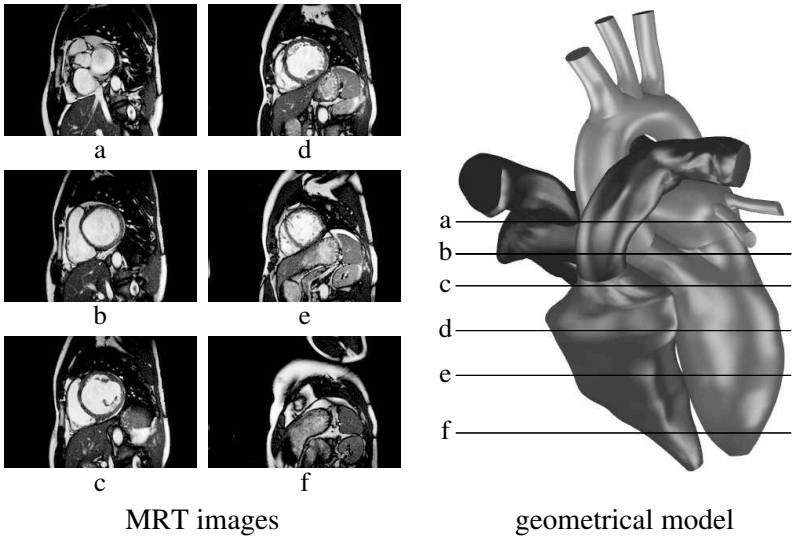

Fig. 4.1. KaHMo heart model

The passive part of the KaHMo heart model consists of a model aorta and vena cava, as well as modelling of the cardiac valves. In the inactive part of the heart, in contrast to the ventricles, the movement is caused by the flow. To calculate the pulsing deviation of the aorta and the cardiac valve motion, a flow-structure coupling is therefore necessary. Since no in vivo stress-strain data of the moving walls are available, the moving geometry has been also specified by the MRT data, or, if human data are not available, added by generic models. Supplementary image data and velocity measurements with ultrasonic Doppler echocardiography have been used, which form the basis for developing a simplified model of the cardiac valves. Instead of all three-dimensional details of the valve motion, only their projection onto the valve plane is modelled, in such a way that the volume fluxes of the human valves are correctly represented.

Figure 4.2 shows a typical example of the results of flow simulations from Section 4.3 with the KaHMo MRT heart model. The results are for the left ventricle, a generic atrium, and an aorta of a healthy human heart at four points in the cardiac cycle. In each case, a snapshot is shown of streamlines in the left ventricle projected into a longitudinal section, as well as the three-dimensional streamlines in the aorta. The intake flow into the left ventricle and the outflow from the atrium as the mitral valve is opened can be seen, along with the intake vortex in the ventricle that accompanies it. This branches in the long-axis view according to the three-dimensional asymmetrical vortex ring of Figure 2.2 into two parts, so that the flow also washes through the apex of the ventricle. A clockwise rotating vortex can be observed in the projection plane; as the aortic valve is opened, the first part is initially expelled into the aorta. The streamlines branch in the aorta into each artery and, because of the centrifugal force in the aorta curve, the secondary flow of Section 2.2 forms.

The KaHMo FSI heart model uses the patient-specific geometry model of the MRT image data at a given point in time of the cardiac cycle, and then calculates the flow-structure coupled motion of the ventricle. In addition, the derivation of an anisotropic material law is necessary for the stress-strain be-

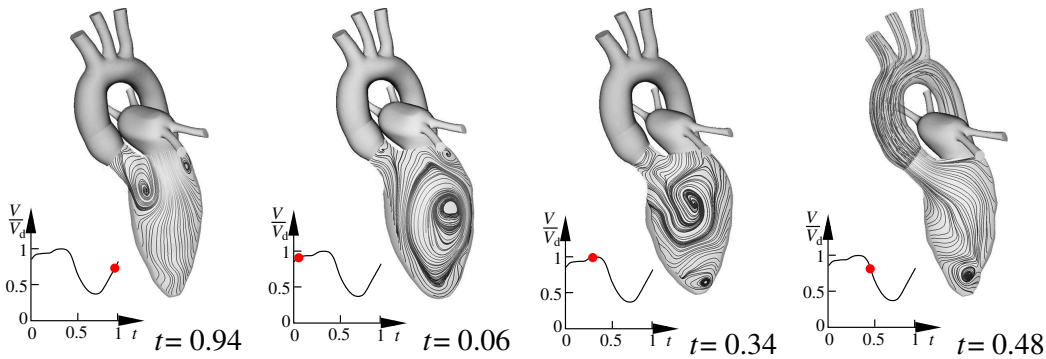

Fig. 4.2. Flow simulation with the KaHMo MRT heart model, $Re_{D\text{systolic}} = 3470$, $Wo = 25$, $T_0 = 1$ s

havior of the myocardium of Figure 2.5, as well as a coupling software that iteratively connects the flow with the structure calculation, in accordance with the sketch of Figure 4.3. The flow simulation of a healthy human ventricle serves as a reference for the flow simulations of unhealthy human ventricles with an aneurysm, both before and after surgery.

The opening and closing of mitral and aortic flaps of the left ventricle and tricuspidal and pulmonary flaps of the right ventricle are pressure controlled. Figure 4.4 shows the opening process of the mitral and aortic valve with an image frequency of 50 Hz. The individual images are taken with a three-dimensional echo-cardiograph by Handke et al. (2003) and reconstructed three-dimensionally, whereby the systole of aortic valve is covered with 50 images. The flap opening already reaches its maximum early in the systole. After this, closure begins, first taking place slowly and finally quickly.

The mitral valve consists of two bicuspid flaps. It permits the filling process of the left atrium between the heart beats and prohibits back-flow of the blood during ventricle contraction. The sinews leading to the papillary muscle prohibit the folding down of the mitral valve flaps during the high pressure of the contraction phase of the heart. The aortic valve consists of three semilunar shaped tissue flaps. During the relaxation phase of the heart, it prohibits back-flow of the blood from the aorta. Because of the high pressure acting on the aortic valve during the contraction phase, the semilunar flaps of the aortic valve are considerably more stable than the bicuspid flaps of the mitral valve. In the opened state, the semilunar flaps of the aortic valve, in spite of the high aortic pressure, do not lie along the aortic bulb. The flow is past the peaks of the flaps and a back-flow region forms between the flaps and the aortic bulb; the opposing pressure of this back-flow region prevents the semilunar flaps

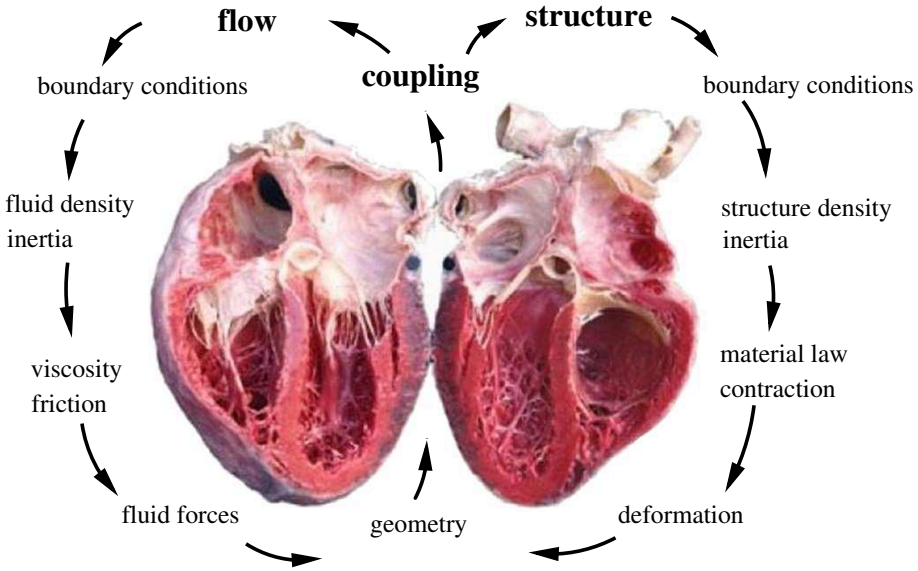

Fig. 4.3. Sketch of the flow-structure coupling

from bulging out and attaching to the bulb. Because of the high shear rates of the intake jet into the aorta, the peaks of the aortic valve flaps are unstable and begin to flap in the opened state. To calculate the flow in the ventricles, it is not necessary to know all the details of the flap motion caused by the flow. It is sufficient to model the volume fluxes through the cardiac valves correctly on the basis of ultrasound Doppler velocity measurements and MRT flow data of the human heart. In the cardiac valve models, only the projection of the natural flapping onto the valve plane is considered. The open shapes of the two-flapped mitral valve and the three-flapped aortic valve are shown in Figure 4.5. The model valves are realized by boundary conditions, to which a variable resistance is assigned. This resistance can be varied between 0 and ∞. By altering the resistance, the valves are opened, corresponding to their projection onto the valve plane. In the closed state, the resistance ∞ is assigned to the valves over the entire surface of the valve plane. In the open state the resistance is 0. The modelling of the tricuspid valve and the pulmonary valve of the right cardiac ventricle is carried out in the same manner.

4.1.1 KaHMo MRT

The starting point of the KaHMo MRT dynamic geometrical model of the moving left ventricle inner wall (Figure 4.6) is one set of MRT image data of a

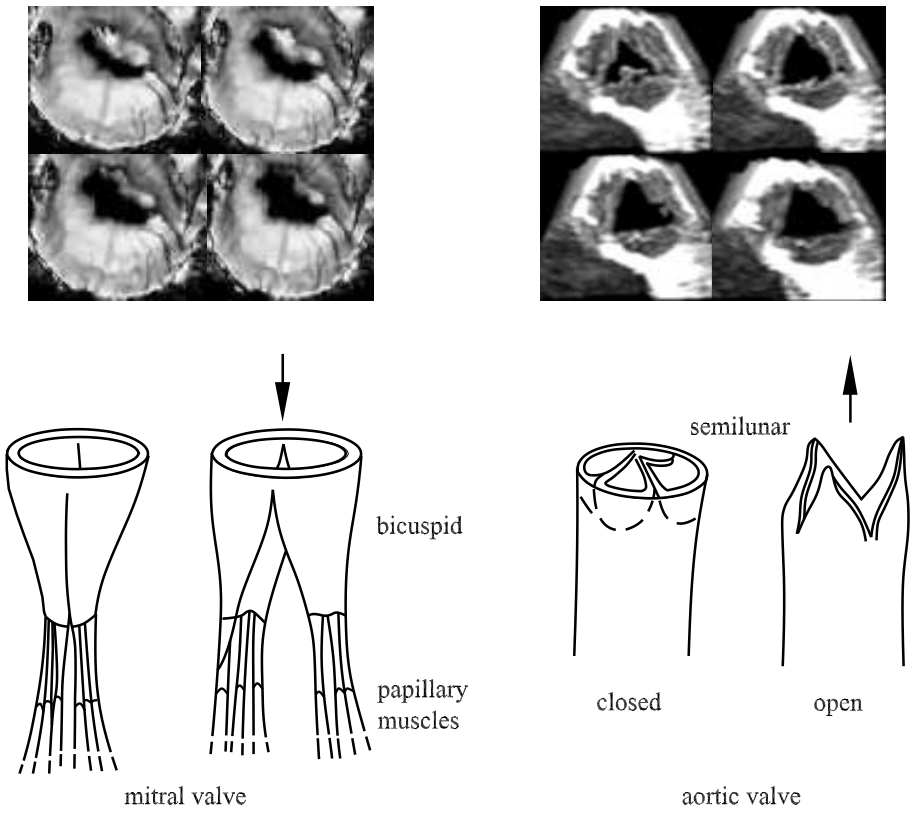

Fig. 4.4. Opening of the mitral and aortic valves

healthy human heart, and data of a pathological ventricle with an aneurysm, both before and after surgery, taken at the University Hospital of Freiburg (Jung (2006)). The methods of MRT imaging, the segmentation of images and the reconstruction of the geometrical models are described in detail by Schenkel et al. (2009).

Eighteen short-axis slices are taken from the top of the heart, through the mitral valve, as well as five vertical sections through the middle of the left ventricle. The sections are rotated about different angles so that the ventricles are seen as fully as possible. In addition, three sections are taken perpendicular to the aortic valve plane. In fitting the boundary conditions of the calculations and the validations of the results, the blood flow in the heart is determined by means of the MRT phase contrast flow measurements. This must be carried out at the same number of cardiac cycles as the earlier image data. The blood flow is measured perpendicular to the aortic valve and the mitral valve plane, as well as in the so-called three-chamber view of the left ventricle outflow tract. The problem in producing pictures of the heart is that the movement

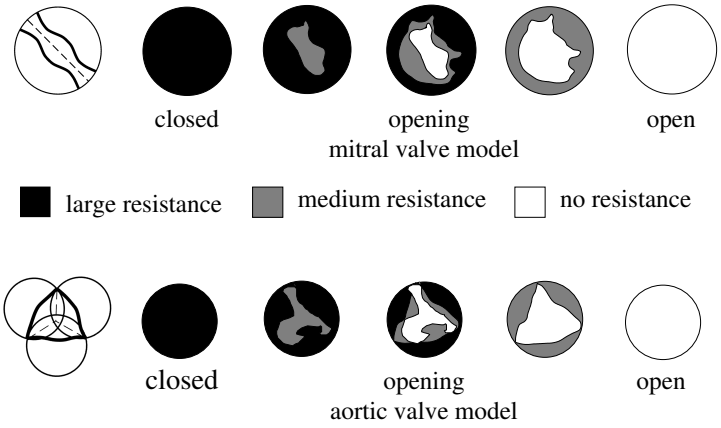

Fig. 4.5. Mitral and aortic valve model

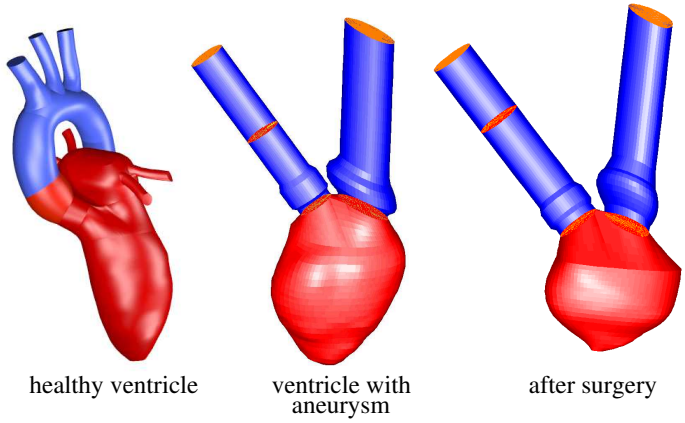

Fig. 4.6. Geometrical models of a healthy human left ventricle and a human ventricle with aneurysm before and after surgery

of the heart and the fast flow of blood make obtaining meaningful images difficult. The breathing of the patient is a further problem, as the motion of the diaphragm causes displacement of the heart in the chest. Therefore, short exposure times and high resolution are necessary for taking images of the heart. Through employing an electrocardiogram (ECG) and corresponding triggering of the image capture, new MRT data acquisition protocols make it possible to obtain time-resolved cine-records of the heart in a phase of only 15–20 seconds where the breath is held. The time resolution of the image acquisition is 50 ms and is chosen depending on the frequency of the heart in order to record 17 – 25 time steps of the cardiac cycle. The spatial resolution and thus the thickness of the individual layers is 6 mm. The demands on the image acquisition and the MRT phase contrast flow measurements, as well as the optimization of the segmentation of the images, are documented in the report by Schwarz (2003) and Oertel et al. (2009).

In order to determine the dynamic geometrical model of the left ventricle, the contours of the left myocardial wall in a cine-heart-MRT image of the human hearts are segmented, in all sections and for all cardiac cycles. The semi-automatic segmentation is carried out using the live-wire method of Mortensen and Barrett (1998). The segmentation method is based on the algorithm of Dijkstra (1959) to optimize the path search in a weighted graph.

The result of segmentation is a scatter plot of the contour data for each time step. As shown in Figure 4.7, a smoothing and triangulation tool is used to create a surface that is coincident in geometry and volume with the segmentation data. The dynamic geometry model of the fluid space of the ventricles and atria, derived from human MRT image data, together with the numerical

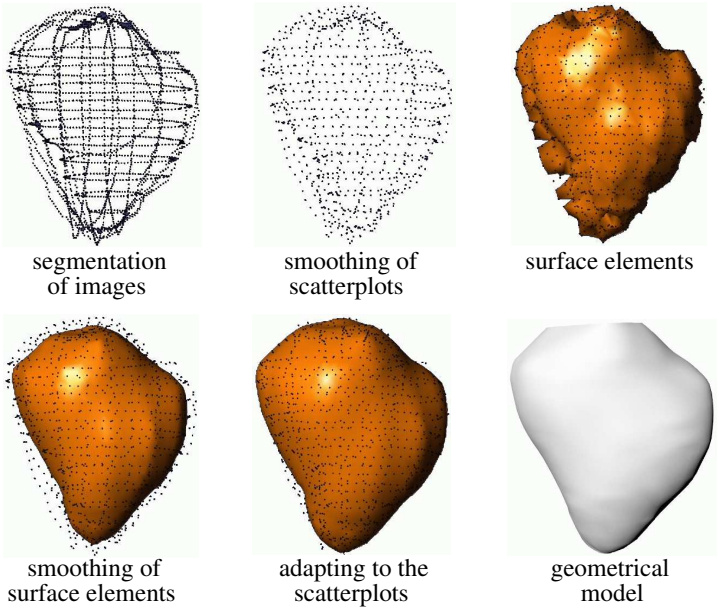

Fig. 4.7. Reconstruction of the geometrical model

model of Section 4.1.4 and the software for the pulsing flow calculation of Section 3.2, forms the basis for the patient-specific *KaHMo MRT* model.

4.1.2 KaHMo FSI

The KaHMo global concept is based on software-independent modelling of the blood flow of the human heart. The motion of the fluid space of the ventricles and atria may be determined either by specifying the *KaHMo MRT* geometry model or via the flow-structure coupled calculation with *KaHMo FSI*. This demands partitioned implicit coupling of the flow software with the structure software in Section 3.2. A requirement for the KaHMo FSI is the development of a *fiber-composite model* for the myocardium. This has the task of including characteristic kinematic properties in the flow-structure interaction. The model is based on the separation of the material properties into *isotropic* and *anisotropic* components.

The continuous change in fiber orientation from endocardium to epicardium, as shown in Figure 4.8, is assumed to be concentrated on the inner and outer layers, which are separated from one another by an isotropic matrix. The angle of the epicardial layer is assumed to be $\alpha_A = -45°$, and that of the endocardial layer $\alpha_I = 35°$. Using this method, the passive material properties of the myocardial tissue are projected onto a simplified model, which turns out to be robust and efficient within the coupling model of Section 3.1. The local stress state in the heart resulting from the fiber and layer system described is initially neglected. However, in comparison to existing *isotropic structure models*, in this way initial anisotopic components are mapped, which can be correlated with the quasi fiber orientation of the tissue-phase mapping of Figure 2.4. In addition, the orientation in the deformed state corresponds indeed to the instantaneous fiber orientation and is not tied to the deformation of the finite elements. With this result, the demands on a macroscopic muscle model for

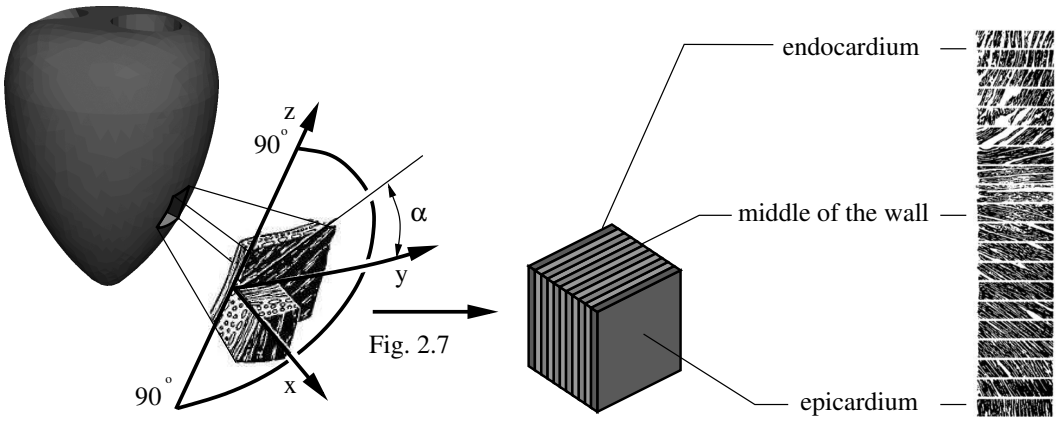

Fig. 4.8. Orientation of the fibers of the endocardium and epicardium

the fluid space motion are satisfied.

If we compare the real change in fiber orientation and the assumed concentration at the inner and outer layers, we may fall back directly on the fundamentals of fiber composite materials. To this end, Figure 4.9 shows a comparison of the *model assumptions* with a *cube* consisting of *n layers*, following the fiber orientation in Figure 4.8. Assuming identical force development in an *equibiaxial tensile experiment* of homogeneous stretching in the $y - z$ *direction*, both models follow from an energy function. Seen globally, the load on the cuboid follows from the relation

$$A_{\text{total}} \cdot \sigma_{\text{total}} = A_{\text{F}} \cdot \sigma_{\text{fiber}} + A_{\text{matrix}} \cdot \sigma_{\text{matrix}} \tag{4.1}$$

Whereas the cube model consists of n layers of different orientation but the same thickness $h_0 = \frac{b_0}{n}$, in the bound model the matrix is assumed to be a cuboid of base area $\Delta x_{10} \times \Delta x_{20}$ and height b_0. In addition, on the upper and lower sides the fiber layers with thickness r_0 are applied. This leads to an adaption of the fiber parameter in the ratio $\frac{b_0}{2r_0}$.

4.1.3 Model comparison and justification

The totality of the passive and active material properties of the myocardium during the relaxation and contraction phases can be described with two separate parts of an energy function (see Krittian (2009)). In this the muscle contractions are formulated by specifying the Strain extension. This still remains to be further developed for the KaHMo FSI model. Such an approach requires an additional coupling of the circulation model with the contraction model. For this reason, as is done for the KaHMo MRT model, simplifying we assume that the muscle contraction dominates the fluid pressure. From this consideration, it is justified to introduce a *hybrid contraction model*, which provides the volume of the matrix and the extension of the fibers. The hybrid characters of this approach consists of correcting the specified motion by

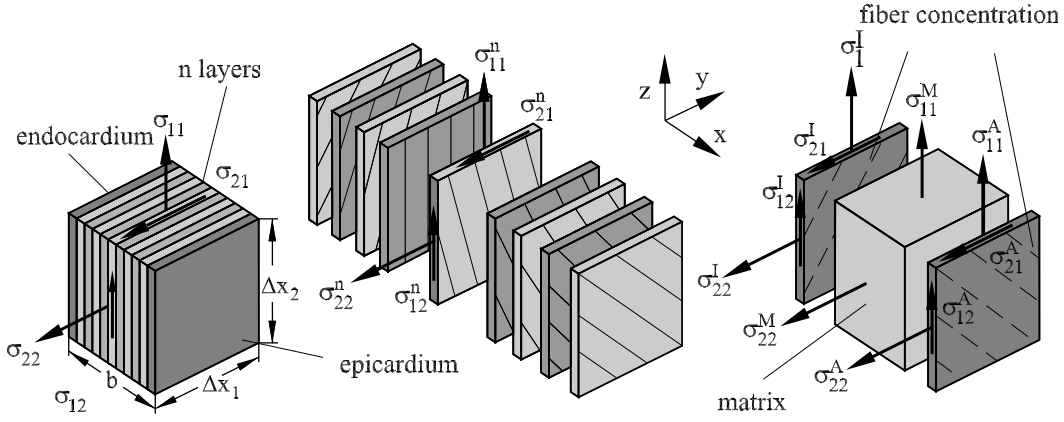

Fig. 4.9. Cube model and abstraction model

means of the coupled fluid pressure in retrospect, and thereby determining the correct equilibrium position. Violation of the requirement to keep the muscle volume constant is initially accepted. The main part of the contraction occurs in the implemented composite fibers, which give rise to a directed motion of the cardiac muscle.

Corresponding to Figure 2.3, the flow-structure coupled KaHMo FSI model can be set out in four phases:

Phase	Name	Structure	↔	Fluid
1	atrium contraction	passive extension	↔	active filling
	myocardial relaxation	active relaxation	↔	passive filling
2	isovolumetric contraction	shape change	↔	constant volume
3	myocardial contraction	active contraction	↔	expulsion
4	isovolumetric relaxation	shape change	↔	constant volume

Phase 1 is determined by the interaction of the increasing circulation pressure with the material properties of the myocardium. The pressure change acting is fixed at $1000Pa$. In the subsequent phase 2, the inner ventricular pressure increases to about $15000Pa$. However, this affects only the shape, and not the inner volume of the structure model. Contraction forces and pressure forces are balanced for the purposes of the hybrid contraction model, and are filtered for the structure side.

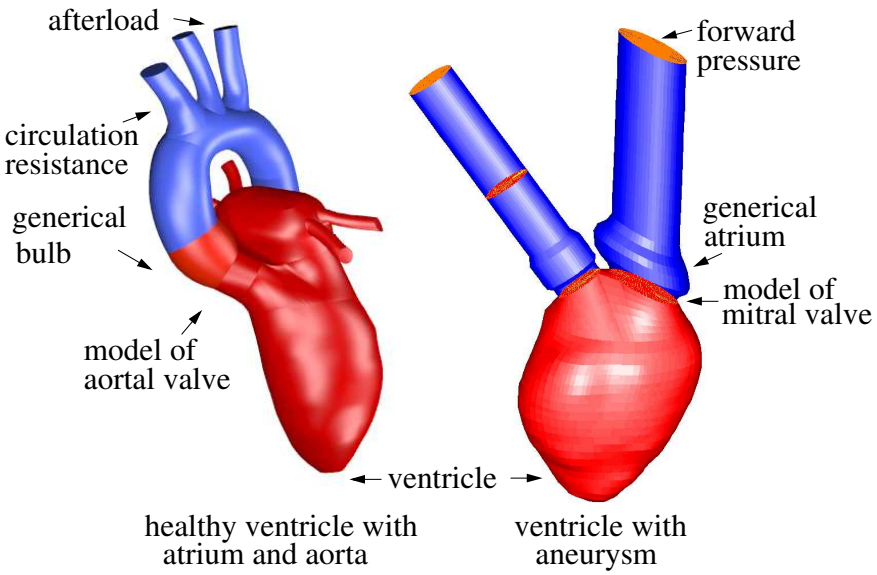

Fig. 4.10. Numerical models

The isovolumetric relaxation of phase 4 behaves analogously to phase 2, and introduces the actual filling process of phase 1. The weakening contraction initially leads to a rapid increase in the ventricle volume, which stagnates before the atrium contraction and, through this, increases once again. The entire process is strongly influenced by the inertial forces of the fluid.

4.1.4 Computational Setup

The basis of the numerical model is the geometrical model of Figure 4.6. The flow in the left ventricle is determined by the periodic motion of the geometrical model. The after-load p_{a}, forward pressure p_{f} and the circulation resistance R are taken from the simplified circulation model of Section 2.2. The pressure boundary conditions are formulated at sufficient distance from the cardiac valve model of Figure 4.5 to minimize the influence of the boundary conditions on the flow simulation in the ventricle. The numerical model of Figure 4.10 is expanded by the atrium and aortic root. For the ventricle with aneurysm and the ventricle after surgery, no in vivo data for the atrium and aorta were available, and so a constant after-load p_{a} and forward pressure p_{f} have been assumed.

The surface of the geometrical model of Figure 4.7 forms the basis of grid generation. The surface and the fluid space of the ventricle are covered with unstructured triangular and tetrahedron cells. The topology of the computational grid is shown in Figures 4.11 and 4.12. At every point in time at which MRT images exist, a separate grid is created. The resulting surface grid is smoothed so that the ventricle volume is kept constant. The grids at each of the 20 time steps are generated so that they are topologically equivalent. The number of nodes and thus of cells is the same in all grids. In order to achieve this, the surfaces of each time step are first covered with structured rectangular cells and then coupled to the same triangular surface mesh, which automatically readjusts to the individual geometry of each time step. For the given resolution of 20 grids over the cycle, 50 intermediate steps are needed

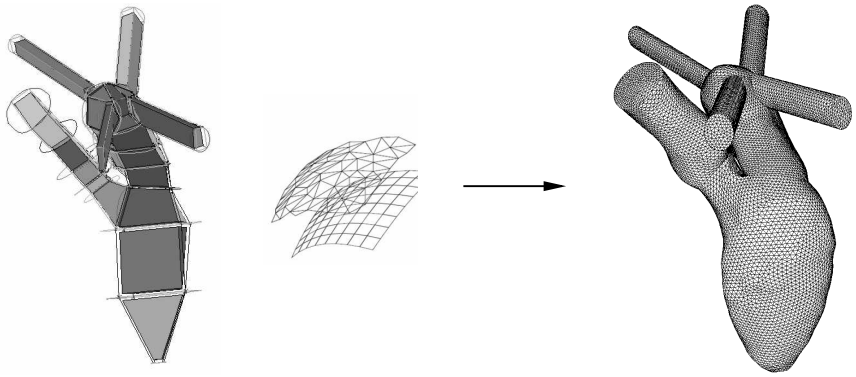

Fig. 4.11. Topology of the computational grid

for the grid used to keep the Courant number Co for the flow simulation close to unity.

The position of the nodes in the grid as well as their identification number also remains constant at each point in time. From the position of the node i at time t_n and at time t_{n+1}, intermediate grids are determined. Nonlinear interpolation is performed between the individual grids, so that it is ensured that the position vectors x_{n-1} and x_{n+1} pass continuously into each other. The motion of the ventricle is different in different regions. The motion of the cardiac valve plane is small compared to the motion in the apex of the heart. Therefore, some sections of the grid, those that can be recognized clearly in the MRT images, are fixed. The remaining grid planes are distributed linearly between these. The global motion of the ventricle is therefore divided into regions of differently sized motion. The flow structure in the ventricle to be calculated is dependent on the number of cells in the computational grid (see Oertel et al. (2005), (2011) and Laurien and Oertel (2011)). Therefore, first the grid dependence of the numerical solution in the ventricle described in the following section has to be analyzed.

The numerical solution of the partial differential equations for the flow requires spatial and temporal discretization, from which a unique approximation solution must result. For this reason, to demonstrate the grid-independence, the fluid space was discretized with a cell number ranging from 12500 to 100000. For the quantitative description of the viscous, incompressible and unsteady blood flow, in particular the mean velocities $\bar{v}_{\mathrm{sys/dia}}$ through the mitral and

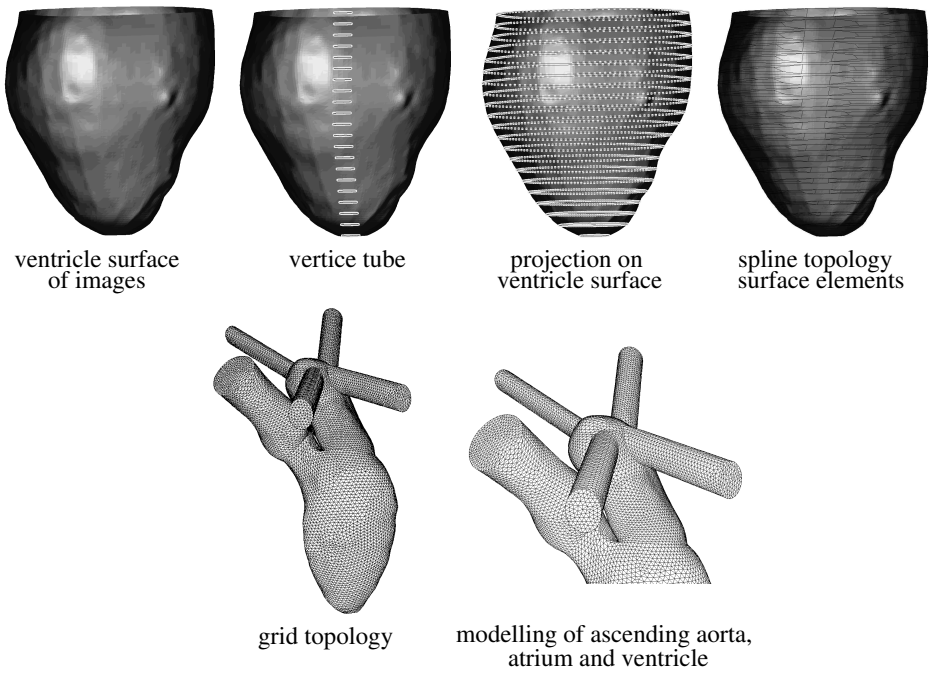

Fig. 4.12. Computational grid

aortic valves, as well as the viscosity $\bar{\mu}_{\text{eff}}$ and vortex strength $\bar{\omega}_{\text{eff}}$ in the volume, were selected. In respect of the existing coupling he sensitivity of the pressure $\bar{p}_K$ and the shearing $\bar{s}_K$ at the common coupling surface are to be examined. Finally, $t_{b,20}$ delivers the time necessary until 80% of the initial end-diastolic blood has left the ventricle. The mean velocities are found directly from the pulse volume V_S of the ventricle, referred to the time duration of the systole or the diastole $t_{\text{sys/dia}}$ as well as the surface of the valve through which the flow passes $A_{A/M}$

$$\bar{v}_{\text{sys/dia}} = \frac{V_S}{t_{\text{sys/dia}} \cdot A_{A/M}} \quad . \tag{4.2}$$

The effective quantities represent the time and volume averaged values, while the quantities denoted with K represent the surface averaged relative values. For the characteristic time and spatial discretization, it should be noted that the physical propagation velocity v_p and the velocity of the numerical transport $\Delta t/\Delta x$ always need to be of the same order of magnitude. This property is described by the Courant number Co:

$$Co = \frac{v_p \cdot \Delta t}{\Delta x} \approx 1 \quad . \tag{4.3}$$

			number of cells			
Sensitive quantities		Unit	12500	25000	50000	100000
Aortic velocity	$\bar{v}_{\text{sys}}$	m/s	0.57	0.57	0.57	0.58
Mitral velocity	$\bar{v}_{\text{dia}}$	m/s	0.24	0.24	0.24	0.24
Vortex strength	$\bar{\omega}_{\text{eff}}$	$1/s$	21.63	24.03	27.07	27.13
Viscosity	$\bar{\mu}_{\text{eff}}$	$g/(m \cdot s)$	6.23	6.18	5.85	5.84
Duration	$t_{b,20}$	s	1.35	1.36	1.37	1.36
Coupling pressure	$\bar{p}_K$	Pa	215.20	210.80	210.36	217.75
Coupling shearing	$\bar{s}_K$	Pa	0.48	0.53	0.59	0.59
Courant number	Co	$-$	1.10	0.93	1.41	1.00

The table shows that both the velocities $\bar{v}_{\text{sys/dia}}$ and the mixing time of the blood $t_{b,20}$ indicate no grid dependence. The remaining values approach asymptotic limiting values for 100000 cells, as shown in Figure 4.13 for the example of the vortex strength $\bar{\omega}_{\text{eff}}$. The ultimate constant vortex strength $\bar{\omega}_{\text{eff}}$ is accompanied with a constant shear rate $\dot{\gamma}$ and yields a viscosity $\bar{\mu}_{\text{eff}}$ that is also constant. With increasing number of cells, ever smaller vortex structures are

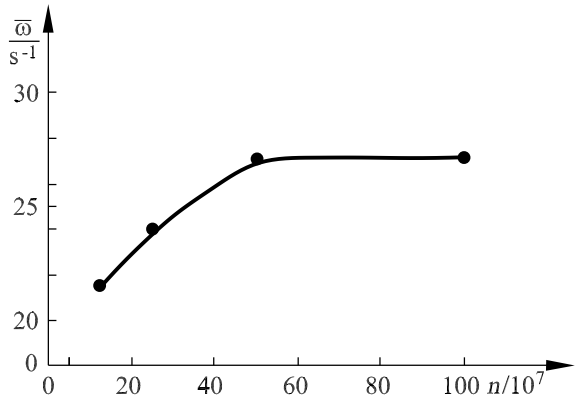

Fig. 4.13. Vortex strength $\bar{\omega}$ as a function of the number of cells n

resolved, which do not contribute to the understanding of the main flow in the ventricle. In addition, an increasing restriction of grid motion and quality is observed. In order to be able to speak of a grid-independent solution, therefore, a grid resolution of 100000 cells is required, which furthermore ensures the extension of the vortex structures of Figure 2.2.

4.2 Validation Experiment

The experiment for the KaHMo model validation was carried out at the Fachhochschule Munich (Schmid et al. (2009)). As shown in Figure 4.14, the validation experiment consists of a model ventricle with mitral and aortic valves and an atrium, whose geometry was derived from the MRT image data of a healthy patient. The model ventricle is covered with an elastic and transparent plastic layer, which has approximately the same mechanical properties as the myocardium. The ventricle liquid consists of dimethyl sulfoxide with the same non-Newtonian properties as blood. The model ventricle with atrium and biological mitral and aortic valves is placed in a pressure chamber from which an external pump periodically removes liquid. This causes the elastic ventricle to be periodically inflated from its end-systolic position to the end-diastolic volume, and thus the human cardiac cycle simulated. For simplicity, the circulatory resistance is represented by two throttles.

All liquids in the measuring chamber as well as the elastic ventricle wall have approximately the same refractive index, so that optical measuring techniques can be used to measure the velocity distributions with particle image velocimetry (PIV). The geometry of the model ventricle was derived from a set of MRT image data from a healthy patient. The data are geometrically processed and a reusable negative model is constructed and filled with resin. The positive model produced in this manner is covered with an elastic, transparent silicon layer about 1 mm thick. The resin is melted and the silicon covering is finally exposed as the model ventricle with atrium.

Using the PIV measuring method, the flow velocities are captured in defined planes over a cycle of $T_0 = 1s$. The recording phases φ_i describe the times $t_i = \frac{\varphi_i}{360} \cdot T_0 = \frac{5+20i}{360} \cdot T_0 (i = 0, 1, 2, \ldots, 17)$. These velocity measurements serve for the validation of the coupled flow simulation, while the resulting volume changes confirm the structure calculation. As by-product of the measuring method, however, 5 mm long-axis slices of the ventricle geometry result at every phase φ_i. By means of this information it is possible to assign a CAD geometry to the individual phases. The right-hand side of Figure 4.14 shows such a CAD geometry for the phase $\varphi_{17} = 345$.

Whereas KaHMo MRT uses the 18 phase geometries as nodes for the grid motion, the CAD information resulting from phase $\varphi_{17} = 345$ is used as a reference geometry for KaHMo FSI. Figure 4.15 shows the discretized regions of the flow and structure models. The *Fluent model* consists of 200000 tetrahedron cells, whereby 100000 cells alone are located on the ventricle. For the discretization of the *Abaqus model*, 10000 linear shell elements are used. Both resolutions are oriented to the characteristic size of 2 mm, which simplifies the search for a partner cell at the common interface. Furthermore, it can be seen that the fluid space covers the entire CAD geometry, while the shell model covers only the coupling surface and the clamping region.

In the framework of this coupling model, the mitral and aortic valves sketched in Figure 4.15 are reproduced using the opening surfaces, also shown. These represent a projected two-dimensional opening surface of the otherwise three-dimensional artificial valves onto the valve plane, and permit time-synchronized opening and closing of the inlet and outlet. The entire surface of the mitral valve in the closed state is $A_M = 660\ mm^2$, and of the aortic valve $A_A = 413\ mm^2$. Both consist of three flaps. The incomplete opening of the valves should be noted; this is due to the characteristic, small ejection fraction that is technically necessary because of the too-small pump power in the experiment. Compared to the results of the patient, this leads to pressures that are too low: 9500 Pa at the atrium and 8500 Pa at the aorta.

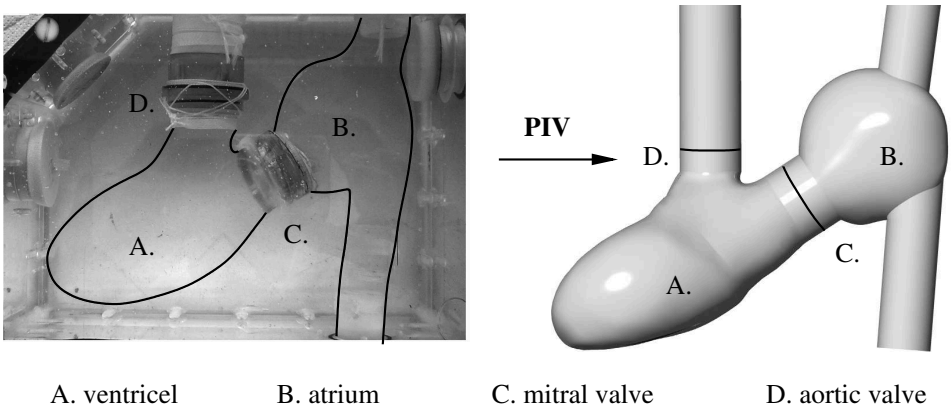

A. ventricel B. atrium C. mitral valve D. aortic valve

Fig. 4.14. Experimental set up and CAD geometry for phase $\varphi_{17} = 345$

The deformation of the simulation model is a direct response to the pressure distribution. Starting with the reference state ($\varphi_{17} = 345$), which is assumed to be stress free, first a contraction of the model ventricle takes place, followed by the actual expansion via a drop in the pressure inside the pressure chamber. If we compare the measured real geometry with the calculated ventricle shapes, very good agreement is observed. Figure 4.16 shows as an example the superposition of the smallest ($\varphi_0 = 5$), the largest ($\varphi_5 = 105$), as well as an average-sized ventricle shape ($\varphi_{10} = 205$) for the filling phase. The dashed line indicates the derived geometry, while the full line indicates the simulation results, which, as expected, overlap. The individual examples shown are representative for the entire motion, which confirms the analysis of the global change in volume in time, as shown in Figure 4.17. It can be seen that the middle filling phase of the simulation has smaller values compared to the derived data from the experiments. This situation is due to the initial over-representation of the fluid inertia. In interpreting the pressure and volume changes, we revert to the experimental data for the pressure. After transforming the relative pressures into boundary conditions of the numerical models of Figure 4.10, it can be seen that the *suction phase* takes up 60% of the cycle time, while the *pressure phase* takes up the remaining 40%. From the measurements of the change in volume, however, it is known that the ratio of intake flow to output flow is 55% to 45%. In addition, it is seen that the suction phase of the measurement is initially influenced by a rapid drop in pressure, whereas the change in volume takes place continuously.

The origin of this effect can be found in the effect of the fluid inertia. Towards the end of the expulsion phase of the experiment, the pressure load is already back in the suction phase. However, the inertia of the exiting fluid acts against this and causes the delayed reaction of the volume change. After the intake

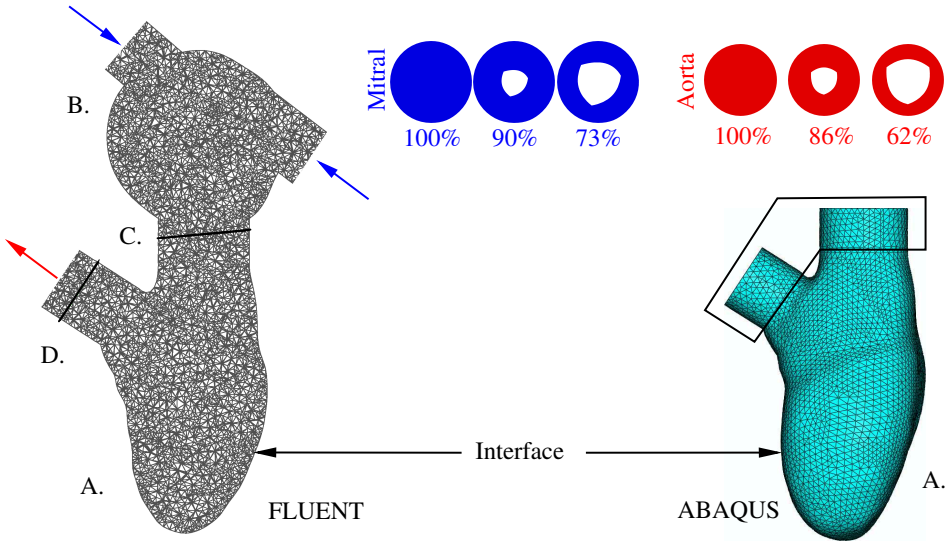

Fig. 4.15. Fluid and structure model for the validation experiment

phase begins it is again the fluid inertia that initially acts against an increase in the volume. In order to obtain the resulting change in volume, this inertia must be met by an initial increase in the suction load. This can be removed as soon as the incoming fluid has been set into motion. On the other hand the pressure of the coupling model is controlled continuously, but it takes into account the 5% phase shift in specifying the pressure. This explains the small deviation of the change in volume seen in Figure 4.17. As a reaction to the boundary conditions of the coupling model, an interaction occurs between the pressure forces acting and the structure of the model ventricle. It can be seen that a comparable result from KaHMo MRT at the beginning and end of the intake and output phases corresponds to the coupled curve. In the vicinity of the smallest ventricle volume, however, a wave-shaped pressure reaction can be seen, which is due to the buckling of the shell model; this can also be observed in the experimental images. If we initially neglect this phenomenon, the early filling phase of KaHMo FSI is characterized by a pressure drop, which can be explained by the suction and intake of the fluid. The fluid that is accelerated towards the end of the filling phase then presses additionally into the ventricle and causes a pressure increase before the transition to the expulsion phase takes place. The pressure continues to rise here, but the the inner-ventricular fluid now needs to be expelled. As soon as the fluid column has been set into motion a further pressure drop is observed. The origin of this again lies in the inertia of the exiting fluid, which towards the end causes the buckling of the structure mentioned above. Assessment of the ventricle motion as well as the resulting change in volume thus permits quantitative evaluation of the flow

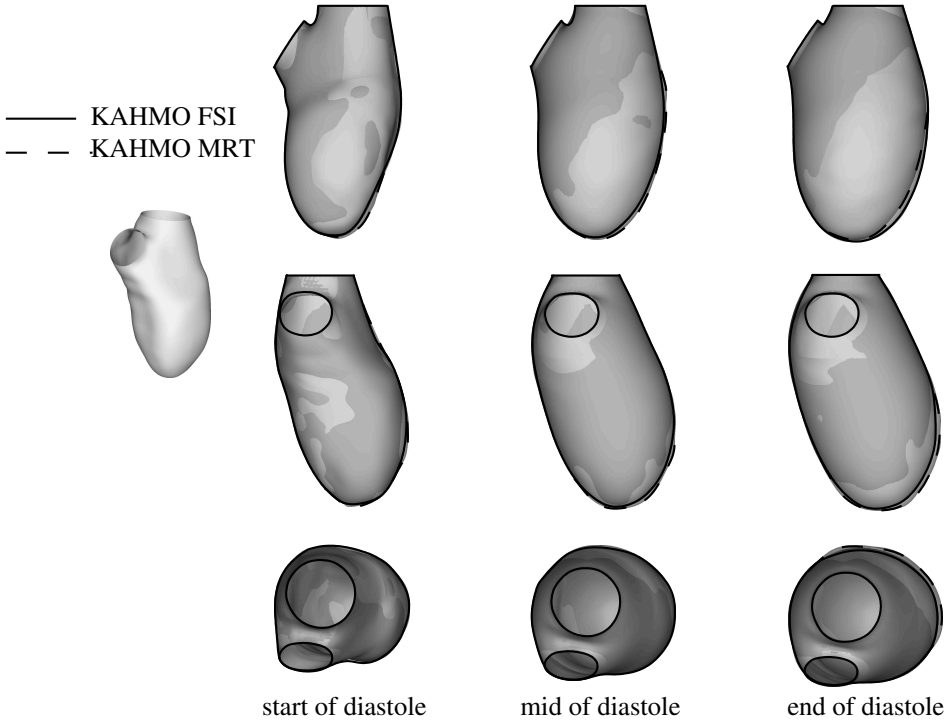

Fig. 4.16. Calculated and measured deformation of the fluid space

solution. As there exists both experimental data and simulations where the motion of the fluid space is specified, the next stage involves a validation of the coupling model.

Comparison with the quantitative results in Table 4.1 shows excellent agreement of KaHMo FSI with the measured experimental data, as well as with the results obtained with KaHMo MRT. Based on the same geometrical model, the quantitative evaluation of the change in volume also yields the expected results. Both KaHMo MRT and KaHMo FSI display small deviations in the average speeds and the viscosity, which become evident in the characteristic numbers in further analysis. If we take the experimental values as a reference, however, a deviation of only about 5% appears. Because of the larger enclosed area in the p-V diagram of Figure 4.21, as expected a slightly increased pV work and thus also a higher dimensionless pumping work are evident in the solution of KaHMo FSI.

As a consequence of the smaller ejection fraction of the validation experiment, however, the Reynolds number is in general very low, which has an effect on the interpretation of the velocity field. By evaluating the mixing parameter in Table 4.1, however, this fact can also be made quantitatively visible. Six cycles instead of the usual two cycles are necessary to determine the resting period of the blood in the ventricle $t_{b,20}$. The other characteristic numbers listed in the table will be introduced in Section 5.1.

The PIV measurements of the validation experiment permit the quantitative recording of the velocity distribution within the model ventricle, as well as the visualization of the flow field. The resulting experimental results are then discussed at the characteristic evaluation phases $\varphi_2 = 45$, $\varphi_5 = 105$, $\varphi_9 = 185$ and $\varphi_{14} = 285$ of Figure 4.17 and compared with the KaHMo MRT and KaHMo FSI results. At phase $\varphi_2 = 45$ an early stage of the intake process take place. At this phase both simulation models correspond to the flow structure of the validation experiment. The intake jet is accompanied by a torus-shaped

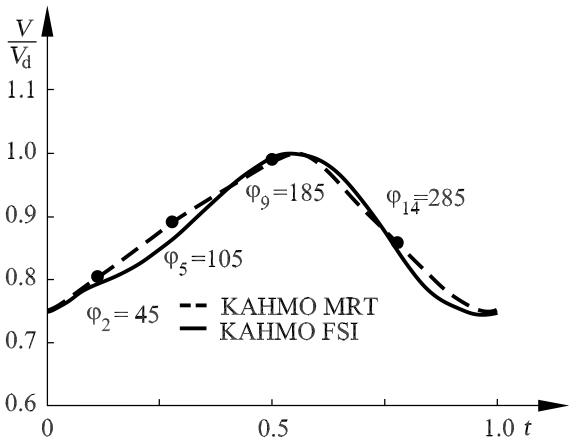

Fig. 4.17. Change in volume

validation experiment:					
model paramaters		unit	FSI	MRT	EXP
mitral valve diameter	D_M	mm	15.01	15.00	15.01
mitral valve surface	A_M	mm^2	176.85	176.81	176.88
atrial pressure	p_M	$mbar$	85		
aortic valve diameter	D_A	mm	14.07	14.09	14.08
aortic valve surface	A_A	mm^2	155.46	155.85	155.70
aortic pressure	p_A	$mbar$	95		
density	ρ_B	kg/m^3	1008		
analysis of volumes		unit	FSI	MRT	EXP
end systolic volume	V_{sys}	ml	142.53	143.64	142.73
end diastolic volume	V_{dia}	ml	192.30	191.74	193.31
stroke volume	V_S	ml	49.77	48.10	50.58
total cycle time	T_0	s	1.00	1.00	1.00
pulse	HR	$1/min$	60	60	60
systolic time	t_{sys}	s	0.43	0.43	0.44
diastolic time	t_{dia}	s	0.57	0.57	0.56
mean flow values		unit	FSI	MRT	EXP
mean velocity (systole)	$\bar{v}_{sys}$	m/s	0.74	0.72	0.74
mean velocity (diastole)	$\bar{v}_{dia}$	m/s	0.49	0.48	0.51
mean viscosity	$\bar{\mu}_{eff}$	$g/(m \cdot s)$	5.23	5.45	5.55
dimensionless parameters		unit	FSI	MRT	EXP
Reynolds number (systole)	Re_D^{sys}	–	2007	1869	1905
Reynolds number (diastole)	Re_D^{dia}	–	1427	1324	1404
Womersley number (systole)	Wo_D^{sys}	–	15	15	15
Womersley number (diastole)	Wo_D^{dia}	–	17	16	16
analysis of pumping		unit	FSI	MRT	EXP
pV work	A_{pV}	J	0.11	0.09	–
power	P_{pV}	W	0.11	0.09	–
ejection fraction	EF	%	26	25	26
mixing parameter	%	M_1	71	71	–
	%	M_4	25	26	–
$\rightarrow$ mixing time	$t_{b,20}$	s	4.35	4.47	–
dimensionless pumping	O	–	$1.83 \cdot 10^6$	$1.50 \cdot 10^6$	–

Table 4.1. Quantitative description of the flow in the validation experiment

ring vortex. The left part of the vortex is fixed in position by the aortic channel. In addition, there is a good representation of the flow structure in the atrium and apex of the heart. As the cycle progresses further, Figure 4.19 shows the deep penetration of the intake jet into the ventricle at phase $\varphi_5 = 105$. The figure shows the projected streamlines through the mitral and aortic valves. The right part of the ring vortex moves to the edge of the fluid space in

the direction of the apex of the heart, while the left part grows in the upper position. The low ejection fraction of $EF \approx 25\%$ is insufficient, as in the human heart, to allow the left vortex part to grow and dominate. The tangential orientation of the streamlines on the lower ventricle edge is due to the ongoing increase in volume of the ventricle.

Also at this point in time good agreement with the flow structure in the atrium and ventricle is apparent. As the increase in volume drops, the velocity of the intake jet also decreases considerably at phase $\varphi_9 = 185$, and a thorough mixing in the atrium in the clockwise direction can be seen. As the maximum volume is reached, this clockwise orientation in the atrium initially persists, before the vortex structure collapses because of the decreasing kinetic energy. The ventricle is now in the expulsion phase $\varphi_{14} = 285$. Here all three results indicate that the preferred expulsion region is in the upper part of the ventricle, whereas the flow through the apex of the ventricle is not optimal. Not least this confirms the very high mixing time of the blood of $t_{b,20} > 4s$.

In addition to the projected streamlines, Figure 4.19 contains further information on the PIV velocity measurements in the two sections shown, which quantitatively demonstrate the intake behavior and the ventricle flow in time. The axes are normalized according to the experimental maximum speed $v_{max} = 1.2\ \frac{m}{s}$ as well as the length of the measuring track $L^* = \frac{x_{max} - x_{min}}{D_A}$ with $0 < L_M^* = ||L^*|| < 1$. The uncertainties in the simulation results of KaHMo MRT (blue) and KaHMo FSI (red) of about 20% are due to the tolerance of the CAD geometry treatment as well as the simplified valve models, and explain the gray background tolerance region. In the documentation of the experiment, the errors in the PIV data in measurement and evaluation are given as a deviation of about 5%. The selected flow phases show very good quantitative agreement of the simulation models with the experimental data at hand. The increase and decrease of the intake velocity during the filling phase can be seen clearly in both sections and is confirmed during the expulsion.

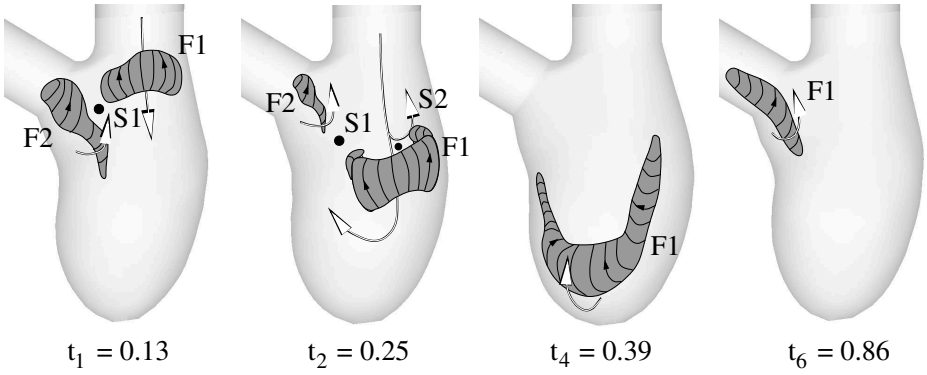

Fig. 4.18. Three-dimensional flow structure in the model ventricle

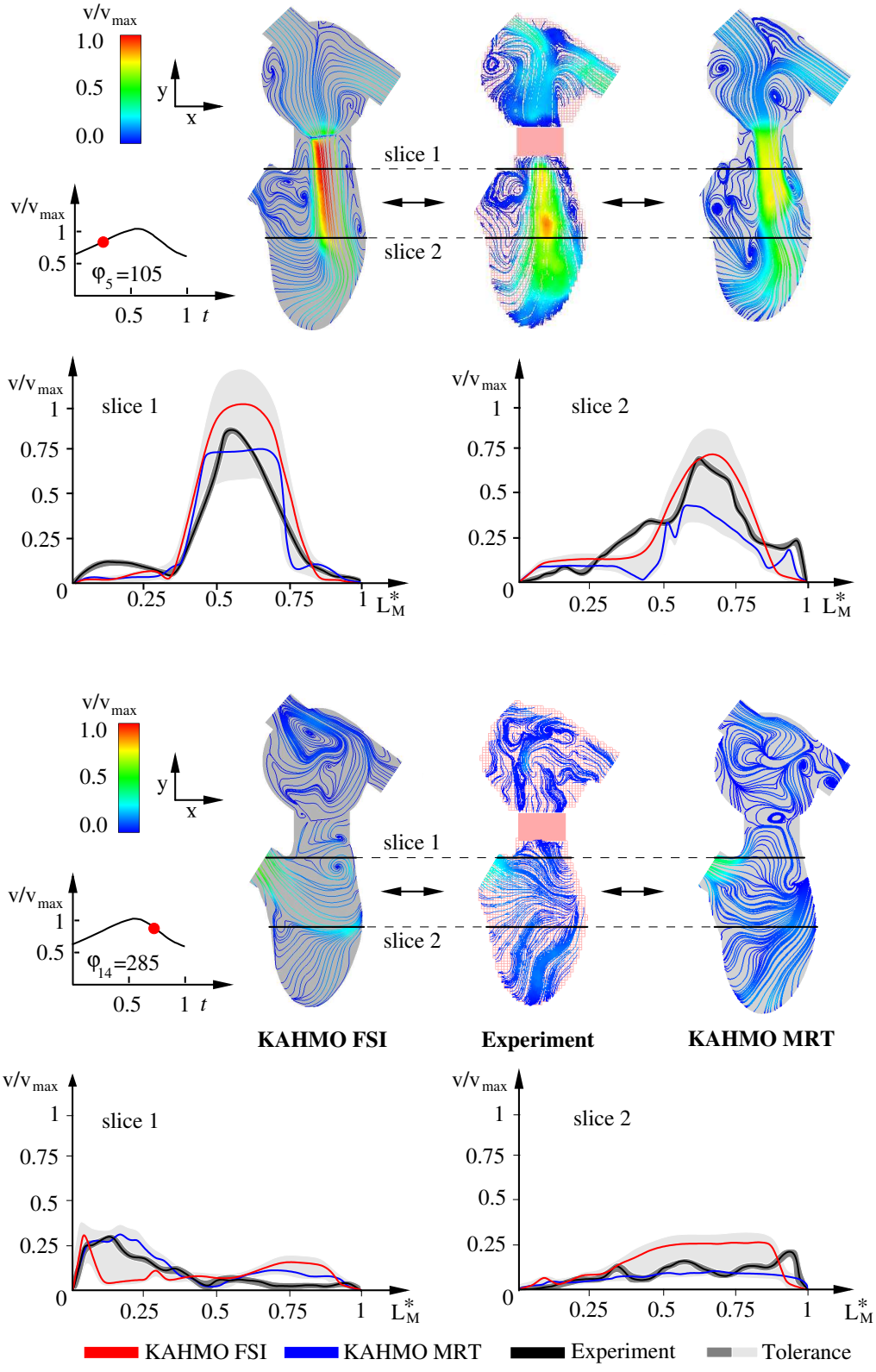

Fig. 4.19. Comparison of the simulation results with KaHMo FSI and KaHMo MRT with experimental data (phase $\varphi_5 = 105$ and $\varphi_{14} = 285$)

In conclusion, however, it should be noted that, in comparison to the flow in a real heart of Figure 2.2, the Reynolds number is too small to be sufficient for the characteristic turning of the ring vortex in the apex of the heart. Instead, a three-dimensional secondary flow arises at the end of the diastole in the mid and lower regions of the ventricle. This is due to the reduced inertia of the fluid. However, for the validation of KaHMo FSI, it is important to compare directly with *experiment* and KaHMo MRT, and so the coupled model at this point can be considered validated. Figure 4.18 shows in addition the three-dimensional flow structure in the model ventricle with quantitative evaluation of the the singular surfaces (see Oertel et al. (2008)) at the times $t = 0.13, 0.25, 0.39$ and 0.86, which correspond to the phases. At the start (t_1) the torus shaped ring vortex (F1) already described forms. Because of the vortex roll remaining in the aortic channel from the previous cycle (F2), the ring vortex is pushed in the direction of the back ventricle wall. The actual directions of rotation can be seen in the figure. Because of the two counter-rotating vortex structures, a saddle point line (S1) forms between the two foci. As the cycle continues (t_3), F1 encounters the back wall of the ventricle, breaks open and tips towards the ventricle apex with the front side downwards. Before the upper half dissipates with vanishing energy, for a short time a half-saddle (S2) arises at the ventricle wall. At the time t_6, F2 is also already completely dissipated and the broken up focus F1 now rolls in the shape of the vortex roll already described, with its ends fixed to the ventricle walls, towards the ventricle apex and rinses it out. At the beginning of the systole and the associated rinsing out, the vortex roll becomes a vortex spiral and moves straight through the ventricle towards the aortic channel, where it remains at the start of the new cycle and there, as F2, displaces the incoming vortex (F1).

4.3 Model Predictions

With the validated KaHMo FSI and KaHMo MRT heart models, flow simulations are carried out on the basis of the MRT image data of the hearts of three healthy volunteer B001, F001 and L001, the heart of an athlete B002 and two patients with aneurysms after a heart attack F002 and F003, both before and after ventricular reduction as well as after four months' recuperation. B stands for the University Hospital Bonn, F for Freiburg and L for Leipzig. The results of the healthy volunteers serve on the one hand to determine reference values for the dimensionless characteristic numbers for Section 5.1 and on the other hand as a reference for cardiac surgery, also described in Section 5.1. The anatomical, physiological and relevant dimensionless characteristic numbers are summarized in Tables 4.2 and 4.3. Comparison of the flow simulations with KaHMo FSI and KaHMo MRT uses data from the healthy volunteer L001 and B001.

4.3.1 Healthy Reference

The calculation of the real set of human data requires the adaption of model parameters that adapt the passive extension as well as the active contraction within the cardiac cycle to the real, existing pressure-volume ratio. On principle, we refrain from changing the circulatory pressure. In the model assumptions presented here, therefore, the stiffness of the muscle model determines the end-diastolic volume, whereas the size of the contraction influences the end-systolic volume. These two reference values can be seen in the MRT data of Table 4.2 and are initially used for the linear adaptation of the change in volume. The resulting coupling then causes a characteristic deformation of the structure model, as can be seen in Figure 4.20. There is a relatively small change in the structure during the contraction of the atrium, and this is followed by a rapid decrease in the inner volume during the expulsion phase. The characteristic ventricle rotation is superimposed on this motion.

Whereas the pressure-volume interaction is realized by a uniform motion in KaHMo FSI, specification from the MRT image data will lead to an exact representation of the local wall motion. However, the effect of the prevailing forces is neglected. For the geometric arrangement at the height where the aorta connects, KaHMo FSI displays an exact representation at the reference

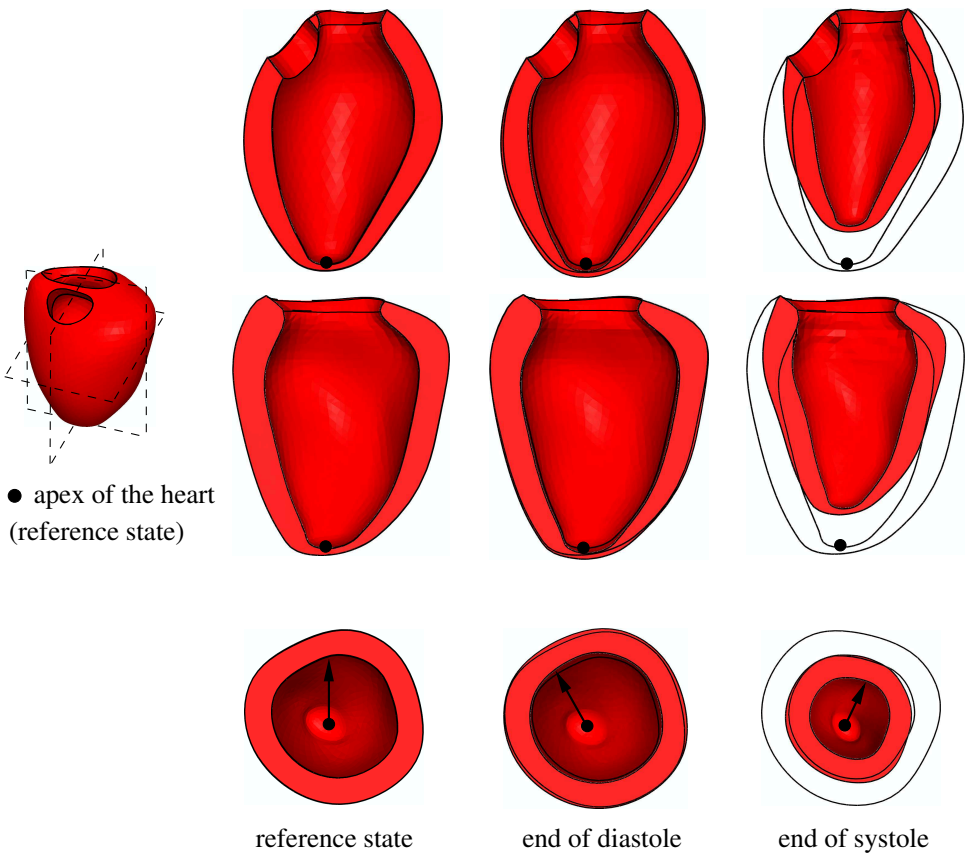

Fig. 4.20. States of deformation of the anatomical model L001

healthy volunteers:					
model paramaters		B001	B002	F001	L001
mitral valve diameter	D_M	25.76	26.79	28.54	24.04
mitral valve surface	A_M	521.01	563.88	640.00	454.00
atrial pressure	p_M	6.3	10.4	7.5	5.0
aortic valve diameter	D_A	22.76	22.08	21.76	19.58
aortic valve surface	A_A	406.84	383.00	372.00	301.3
aortic pressure	p_A	135	117	118	160
density	ρ_B	1008			
analysis of volumes		B001	B002	F001	L001
end systolic volume	V_{sys}	66.86	82.00	64.00	71.19
end diastolic volume	V_{dia}	176.33	178.00	166.00	162.17
stroke volume	V_S	109.47	96.00	102.00	90.98
total cycle time	T_0	1.03	1.22	0.76	0.8
pulse	HR	58	49	79	75
systolic time	t_{sys}	0.35	0.44	0.27	0.35
diastolic time	t_{dia}	0.68	0.78	0.49	0.45
mean flow values		B001	B002	F001	L001
mean velocity (systole)	$\bar{v}_{sys}$	0.76	0.57	1.02	0.86
mean velocity (diastole)	$\bar{v}_{dia}$	0.31	0.22	0.33	0.45
mean viscosity	$\bar{\mu}_{eff}$	5.04	6.27	5.37	4.76
dimensionless parameters		B001	B002	F001	L001
Reynolds number (systole)	Re_D^{sys}	3468	2009	4150	3566
Reynolds number (diastole)	Re_D^{dia}	1588	939	1750	2294
Womersley number (systole)	Wo_D^{sys}	25	20	27	25
Womersley number (diastole)	Wo_D^{dia}	28	24	36	31
analysis of pumping		B001	B002	F001	L001
pV work	A_{pV}	1.46	1.25	1.84	1.51
power	P_{pV}	1.41	1.02	2.4	1.89
ejection fraction	EF	62	54	61	56
mixing parameter	M_1	38	42	33	39.5
	M_4	4	5	2	3
$\rightarrow$ mixing time	$t_{b,20}$	1.23	2.14	0.93	1.01
dimensionless pumping	O	$3.25 \cdot 10^6$	$4.44 \cdot 10^6$	$3.13 \cdot 10^6$	$3.52 \cdot 10^6$

Table 4.2. Anatomical and physiological data from healthy volunteers (units as in Table 4.1), averaged healthy reference value $O_r = 3.4 \cdot 10^6$

time, whereas in KaHMo MRT this region has to be completed generically. However, the necessary MRT image data are not yet continuously available. Comparison of the change in volume for KaHMo FSI and KaHMo MRT is shown in Figure 4.21. The deviation in the end-diastolic volume is around 5%. Comparison of the reference volume before the atrium contraction also

indicates only a minor deviation. However, if we consider the end-systolic volumes, the discrepancy here is around 15%. The cause of this can be found in the incipient interaction effects.

Although the enclosed area of the p-V diagram is almost identical as a measure of the work done, the volume deviation is expressed by a shift to the right, as shown. Furthermore, it can be seen that both model assumptions come from the same pressure level at the start of the filling phase. However, whereas the specification of the fluid space motion in this phase has to cope with a fluctuation in the pressure, the coupled solution indicates an absolutely uniform relation between pressure and volume. This fact is visible particularly in the final atrium contraction. Whereas the solution with KaHMo MRT here reacts to the expected drop in relative pressure, the pressure boundary condition in KaHMo FSI acts to level out this change. During the contraction phase, both models move synchronously, which confirms the assumption that the contraction phase can be represented well by specification of the fluid space motion. However, looking more closely it becomes clear that the pressure drop of the coupled solution begins earlier and accounts for more kPa. The combination of pressure change and modelled contraction is the cause of the present discrepancy in the end-systolic volume.

The fluid expelled at the reduced cycle time T_0 causes an inertia effect that can lead to a strongly negative relative pressure. This effect is indeed physical, but it can become numerically over-emphasized by the partitioned coupling. A real heart reacts to this effect also with inertia and thereby acts to retard the exiting column of fluid. In addition, the muscle structure at this time is in a phase of extreme stress, which, in contrast to the contraction specification used here, additionally stiffens the ventricle. If we compare the resulting ejection fraction and the stroke volume of KaHMo FSI and KaHMo MRT, a discrepancy of only 3%-4% is found.

The three-dimensional flow structure in the healthy human ventricle L001 indicates the characteristic features of Figure 2.2. Figure 4.22 shows a comparison

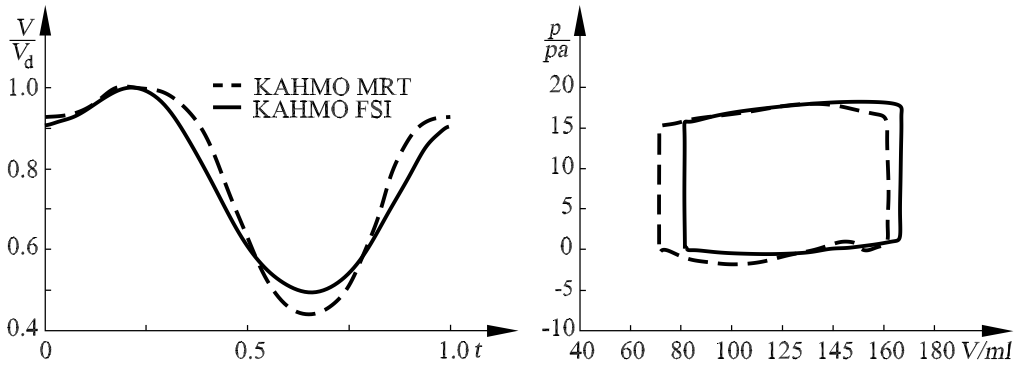

Fig. 4.21. Comparison of the change in pressure and volume for KaHMo FSI and KaHMo MRT

of the simulation results achieved with KaHMo FSI and with KaHMo MRT. The filling phase in both solution indicates the onset of the torus-shaped ring vortex F caused by the intake jet in the ventricle. The blood that was earlier at rest is locally set into motion with a high velocity. Here the difference in modelling of the ventricle basis becomes evident. The onset of the ring vortex in KaHMo MRT is greatly influenced by the aortic channel, whose shape plays an important role as the diastole progresses. The corresponding region of the reference geometry in KaHMo FSI is less extended, as necessitated by the model, so that here a relatively free ring vortex arises. Consequentially, further progression of the filling phase can be seen in Figure 4.22, affected by the dominant asymmetric growth of the left side of the vortex. It is seen that the solution of KaHMo MRT penetrates deeper into the ventricle than the same solution of KaHMo FSI. This fact is explained by the comparison of the change of volume shown in Figure 4.21. In KaHMo MRT the filling phase begins in a more restrained manner, but then in the mid filling phase it is characterized by a larger negative slope. The comparatively deeper penetration of the incoming blood is therefore due to the temporary volume flux and the associated kinetic energy.

As the process continues, the left part of the vortex continues to expand, whereby the right-hand part is pressed against the wall and moves towards

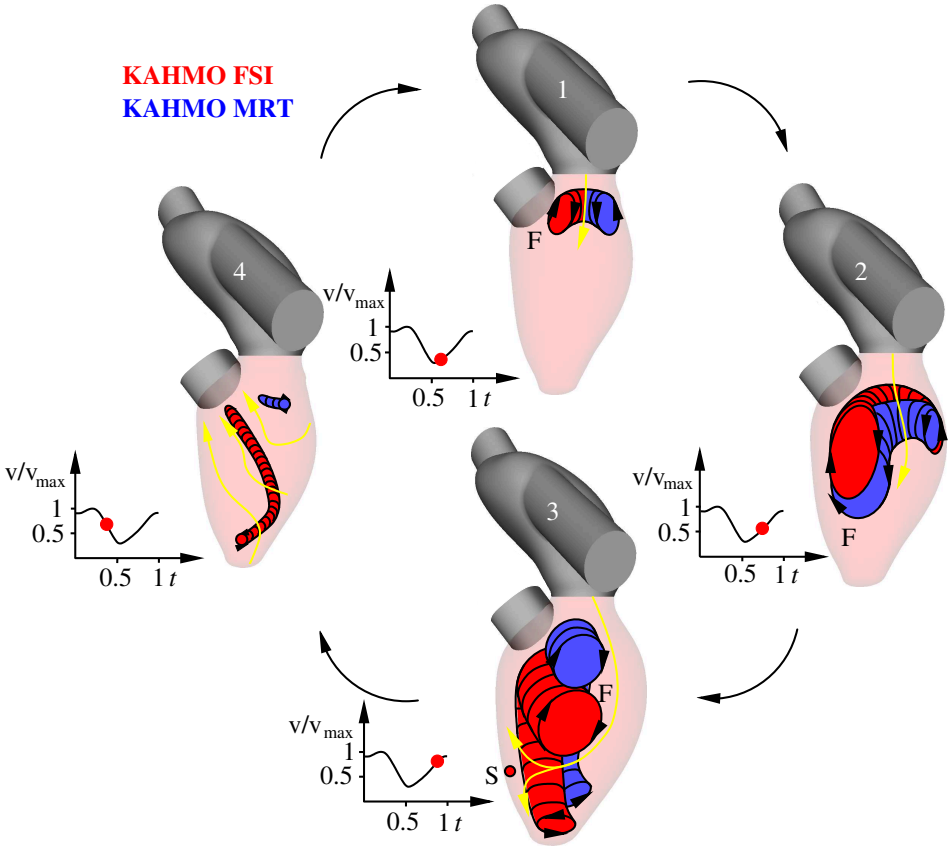

Fig. 4.22. Comparison of the three-dimensional flow structure in the ventricle L001

the apex of the heart. The tilting of the ring vortex takes place over a relatively short stretch of time and progresses in the clockwise direction. If one moves in the center of the vortex from the middle towards the apex of the heart, the path initially leads along the wall towards the base of the heart. The flow therefore has a preferred direction that permits energetically favorable expulsion from the ventricle. The vortex structures that arise are still scattered and are identified with small kinetic energy in the previous flow field of the filling phase.

Recent KaHMo FSI simulations in the healthy human ventricle B001 (Mühlhausen (2011)) show corresponding results regarding the three-dimensional flow structure and dimensionless flow parameters of Table 4.2 (see Figure 4.23).

4.3.2 Pathological Applications

Figure 4.24 shows individual images in the long-axis section of the systole and diastole of the MRT image data F001 for the healthy reference ventricle and F002 and F003 for two patients with an aneurysm before and after surgery, as well as for F003 after four months' regeneration time. The cause of an increase in size of the left ventricle of the patient is a lack of blood flow because of deposits in particular in the branches of the coronary arteries. The scarred, dead, necrotic regions of the myocardium do not take part in the pumping work of the ventricle. In order still to maintain the pumping power for circulation, the heart reacts with an increased pumping volume. In the course of time the ventricle increases so much that it no longer fits in the chest cavity and must be reduced in size by means of surgical ventricular construction. Thus the simulation results attained with the KaHMo heart model provide the cardiac surgeon with an indication of optimal patient-specific ventricle geometry to be achieved by surgery, and also permit quantitative evaluation of the reconstruction results with respect to fluid mechanical losses.

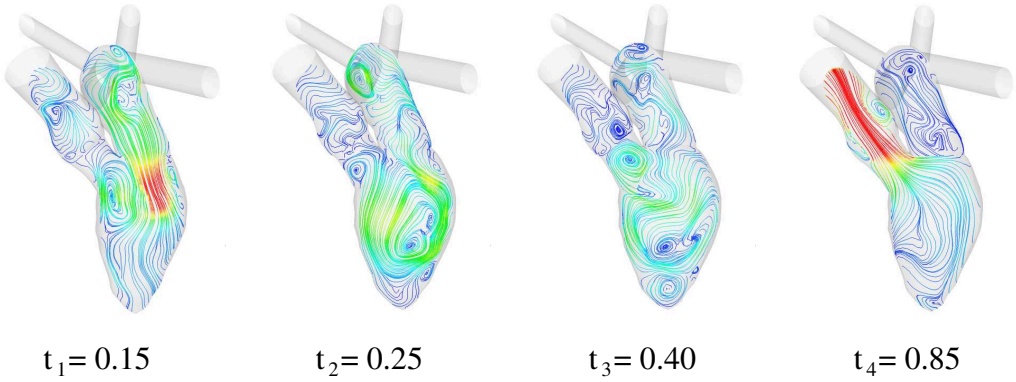

Fig. 4.23. Flow structure in the long axis plane of ventricle B001

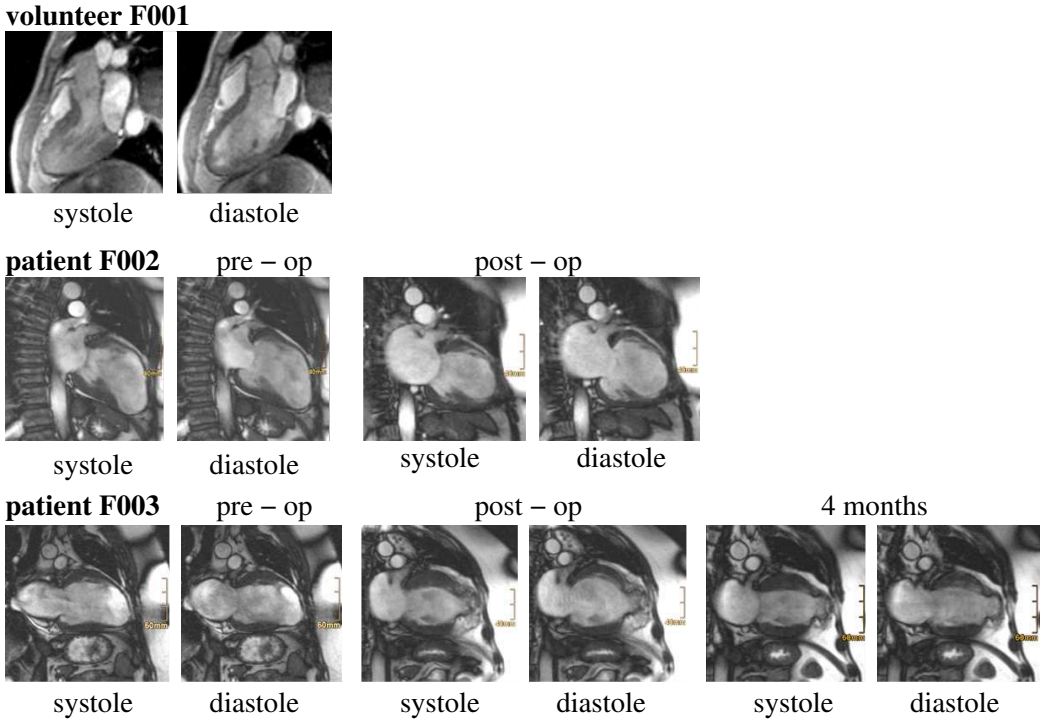

Fig. 4.24. MRT image data of the healthy ventricle F001 and of patients F002 and F003 before and after ventricular reconstruction

Figures 4.25 and 4.26 show the simulation results in long-axis section attained with KaHMo MRT. The figure shows three-dimensional streamlines, projected streamlines in the long-axis section and the magnitude of the velocity according to the color scale. The three-dimensional flow structure of the healthy ventricle F001 corresponds to Figure 4.22 for the similarly healthy ventricle L001. The same figure also shows the simulations of Figure 4.2 for the third reference ventricle B001 including the simulation of the atrium flow with the four approaches. Following a heart attack, both patients shown suffered from the same pathological symptoms and underwent surgical reconstruction of the ventricle and bypass surgery to improve the supply to the coronary vessels.

The flow calculation for both patients shows that at the beginning of the diastole the intake jet arises downstream of the mitral valve with the characteristic ring vortex, but as the diastole continues, because the ventricle vortex is increased and no longer conical, a strongly asymmetric ring vortex forms and the turning into the ventricle apex does not happen. Thus, during the systole the time sequence of the expulsion of the blood vortex, as in the healthy ventricle, is no longer assured. This is expressed as a smaller ejection fraction, namely $E = 15\%$ for patient F002 and also $E = 15\%$ for patient F003. By ventricular reconstruction the ventricle volume of the patients was reduced by one quarter to one third. In patient F002 a spherically symmetric ball-shaped ventricle geometry was selected and for patient F003 an elongated geometric, but without use of the shaper described in the next section.

patients:						
model paramaters		F002 pre	F002 post	F003 pre	F003 post	F003 4 months
mitral valve diameter	D_M	25.04	25.04	24.00	24.00	24.00
mitral valve surface	A_M	492.28	492.28	475.00	475.00	475.00
atrial pressure	p_M	6.1	6.9	7.5	7.5	7.5
aortic valve diameter	D_A	20.65	20.65	21.80	21.80	21.80
aortic valve surface	A_A	334.78	334.78	372.00	372.00	372.00
aortic pressure	p_A	129	134	89	103	102
density	ρ_B	1008				
analysis of volumes		F002 pre	F002 post	F003 pre	F003 post	F003 4 months
end systolic volume	V_{sys}	148.43	105.80	214.00	155.00	126.00
end diastolic volume	V_{dia}	175.25	128.54	253.00	208.00	176.00
stroke volume	V_S	26.82	22.74	39.00	54.00	50.00
total cycle time	T_0	0.91	0.833	0.833	0.583	0.632
pulse	HR	66	72	72	103	95
systolic time	t_{sys}	0.37	0.34	0.33	0.256	0.304
diastolic time	t_{dia}	0.54	0.49	0.50	0.327	0.328
mean flow values		F002 pre	F002 post	F003 pre	F003 post	F003 4 months
mean velocity (systole)	$\bar{v}_{sys}$	0.22	0.20	0.32	0.56	0.45
mean velocity (diastole)	$\bar{v}_{dia}$	0.10	0.09	0.16	0.35	0.32
mean viscosity	$\bar{\mu}_{eff}$	7.56	7.46	7.32	5.47	5.78
dimensionless paramaters		F002 pre	F002 post	F003 pre	F003 post	F003 4 months
Reynolds number (systole)	Re_D^{sys}	596	557	944	2266	1692
Reynolds number (diastole)	Re_D^{dia}	337	319	554	1570	1389
Womersley number (systole)	Wo_D^{sys}	20	21	22	31	29
Womersley number (diastole)	Wo_D^{dia}	24	25	25	35	32
analysis of pumping		F002 pre	F002 post	F003 pre	F003 post	F003 4 months
pV work	A_{pV}	0.40	0.34	0.47	0.75	0.68
power	P_{pV}	0.44	0.41	0.56	1.29	1.08
ejection fraction	EF	15	18	15	26	29
mixing parameter	M_1	82	80	86	67	67
	M_4	44	39	56	23	15
$\rightarrow$ mixing time	$t_{b,20}$	6.77	5.41	9.13	2.52	2.14
dimensionless pumping	O	$1.33 \cdot 10^7$	$1.09 \cdot 10^7$	$1.5 \cdot 10^7$	$6.4 \cdot 10^6$	$5.0 \cdot 10^6$

Table 4.3. Anatomical and physiological data from patients (units as in Table 4.1)

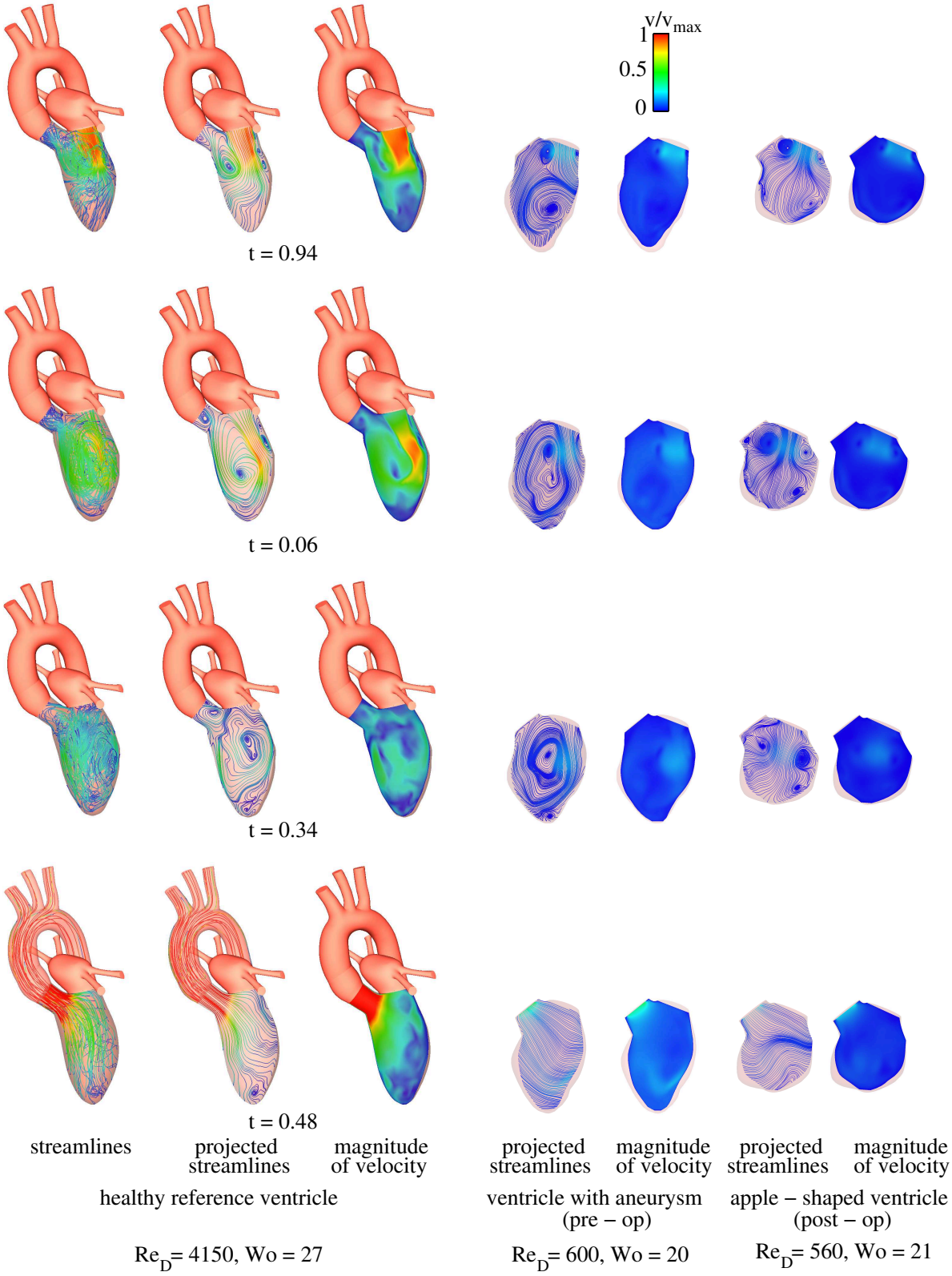

Fig. 4.25. KaHMo MRT results of the ventricular flow of volunteer F001 and patient F002

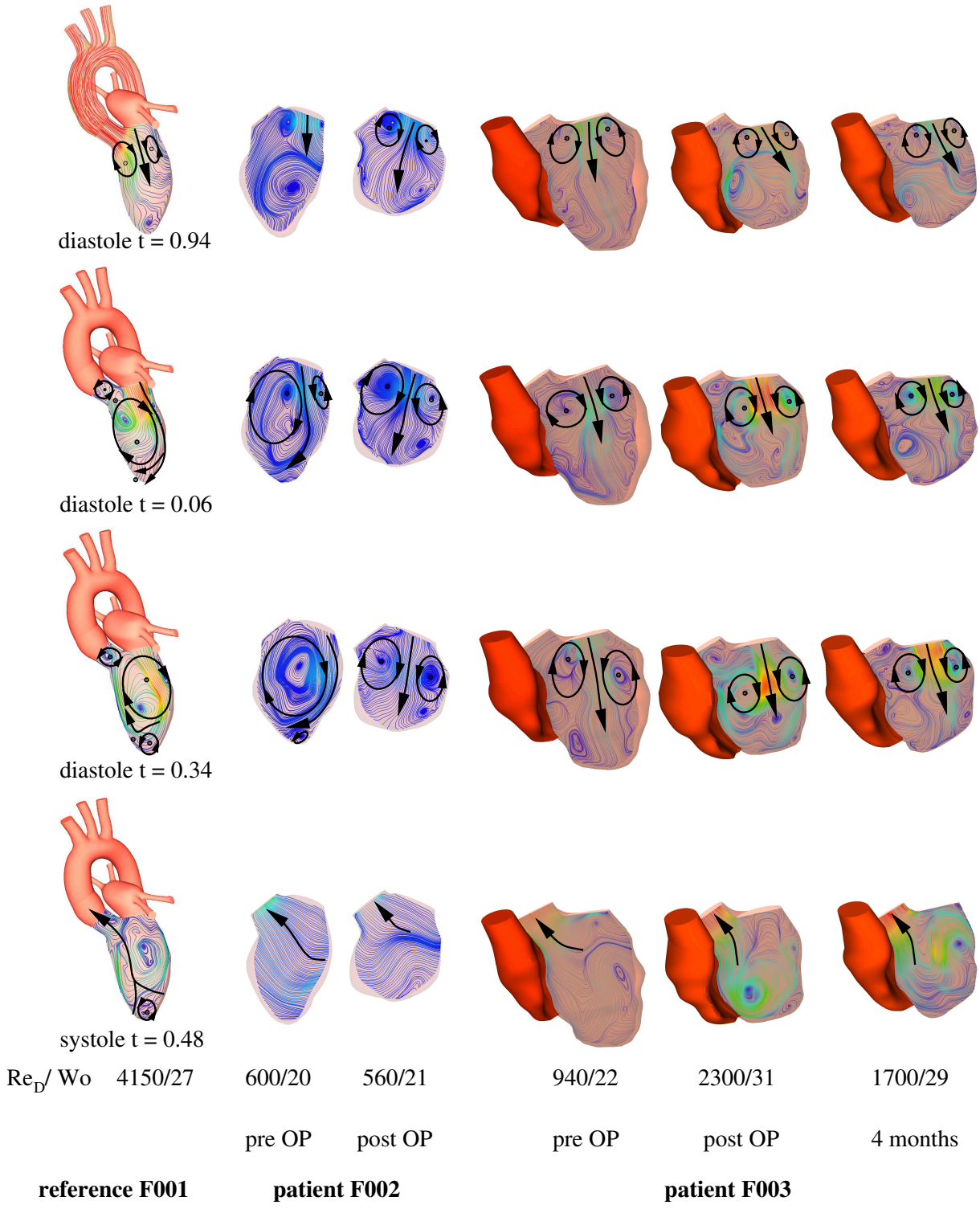

Fig. 4.26. Flow structure of the ventricular flow of volunteer F001 and patients F002 and F003

The streamline images (after surgery) of Figure 4.26 show that the ball-shaped ventricle geometry has the greatest flow losses. A stagnation point flow forms during the diastole, accompanied by an ejection fraction reduced to $E = 15\%$. The reconstructed ventricle geometry of patient F003, which is elongated but not conical, improves the ejection fraction to $E = 26\%$, which, after four months' regeneration time for the patient, increases to $E = 29\%$. However, the streamline images after four months' regeneration time make it clear that, as for patient F003, the flow that occurs is almost stagnation point flow, but with a smaller velocity, and the turning of the ring vortex into the apex of the ventricle does not take place. However, the somewhat elongated ventricle shape permits a more efficient ejection of the blood into the aortic channel during the systole, especially after four months' regeneration time. From this we may conclude that a ventricular reconstruction with a shaper geometry modelled on the conical healthy ventricle delivers the best post-operative fluid mechanical values.

4.4 Latest Developments & Possible Enhancement

4.4.1 Ongoing KaHMo Research

The overall mission of KaHMo is represented by its patient-specific applicability. The final step towards this goal has been achieved recently by Mühlhausen et al. (2011) and the implementation of subject-specific myocard information with adopted fibre orientation. While the focus of KaHMo is still on providing a fluid-mechanics understanding of cardiovascular disease, the complexity of the human heart required both surface and volume coupling interfaces that allow the modularly application of fluid-structure interaction approaches and therefore the potential of integrating total heart function.

Advances in Medical Imaging such as Echocardiography (ECG) and Magnetic Resonance Imaging (MRI) allow accurate measurement of cardiac geometry, wall motion and inflow conditions and provide high resolution data sets for characterising individual patients. This in turn will support a paradigm shift away from predefined clinical indices determining treatment options and a move towards true personalisation of care based on imaging and modelling an individuals specific physiology. In order to improve a model of whole heart fluid mechanics a fluid-solid coupled valve model integrated in KaHMo represents a challenge that will be become possible in future considering the increasing amount of high-performance computing. Although KaHMo's coupling algorithm is able to handle valve opening simulations for simplified test cases, an implemented approach has to take different time scales of valvular

and ventricular motion into account. The challenge of merging the cultures of leading edge simulation research with real world clinical implementation should not be underestimated. However, through the successful integration of 2D projected valve models based on clinical imaging and patient record data into KaHMo, we believe that KaHMo can significantly and positively impact on both clinical outcomes and medical practice.

4.4.2 MR-based 4D Flow & Pressure Estimation

The results of KaHMo analysis models provide important insight into subject-specific cardiovascular fluid mechanics in order to guide diagnosis and therapy planning. In cooperation with medical physicists and clinicians, these results can be used as comparison to modern 4D flow imaging techniques. Subject-specific flow measurement can also be used for computational stand-alone models that can, in turn, provide important input to KaHMo-like models. In this chapter we want to demonstrate how 4D-flow information can be used to calculate subject-specific relative pressure fields as boundary condition for cardiovascular fluid-solid coupled models.

Data Acquisition and Processing:

To understand the complex dependency of subject-specific blood flow and soft tissue interaction, the non-invasive evaluation of cardiovascular velocity and relative pressure fields is of significant value. Time-resolved 3D Phase Contrast MRI (4D-PC-MRI) represents an emerging technology that detects patient-specific blood-flow velocities. The velocity input for the pressure estimation is

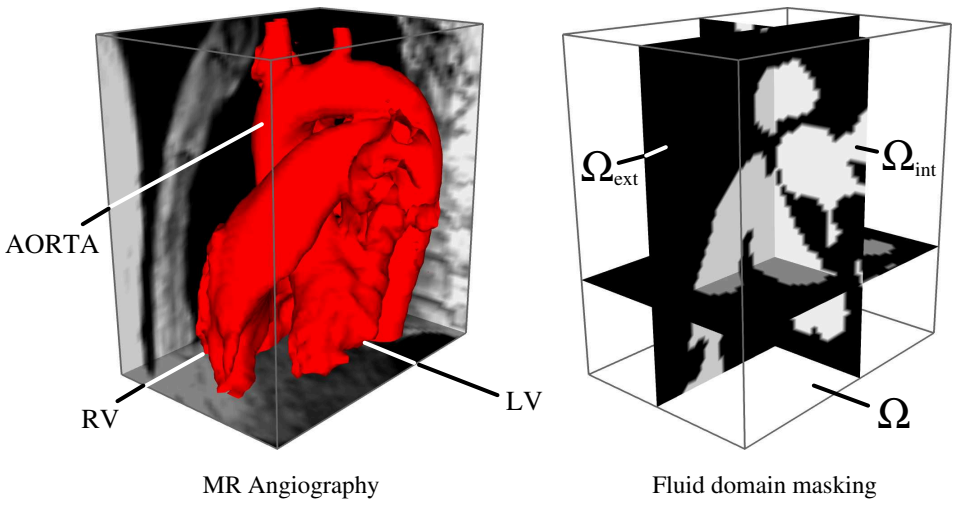

Fig. 4.1. Angiography inside imaging space Ω (left) provides mean fluid domain needed for $\Omega_{ext}/\Omega_{int}$ masking (right).

provided by phase-contrast MR imaging, a technique that allows blood flow velocity to be measured and post-processed non-invasively (Magnetom Trio, Siemens AG, Erlangen, Germany).

In order to allow for a robust and accurate estimation result, 4D flow data with three-directional velocity encoding and covering the whole heart fluid domain were be acquired for this approach with the following settings: spatial resolution 2.95x2.50x2.90mm^3, temporal resolution 38.4ms, velocity encoding 150cm/s, and 17 time frames per cardiac cycle. Initial raw data normally contains magnitude and three-dimensional phase information for each voxel of the initial imaging space. Voxel-based phase shifts can be directly transformed into velocity vectors which marks the starting point for our cardiovascular pressure estimation.

Figure 4.1 represents the imaging space Ω derived directly from the 4D flow MR sequence. The entire space can now be separated into the fluid domain Ω_{int} as well as the surrounding areas Ω_{ext}.

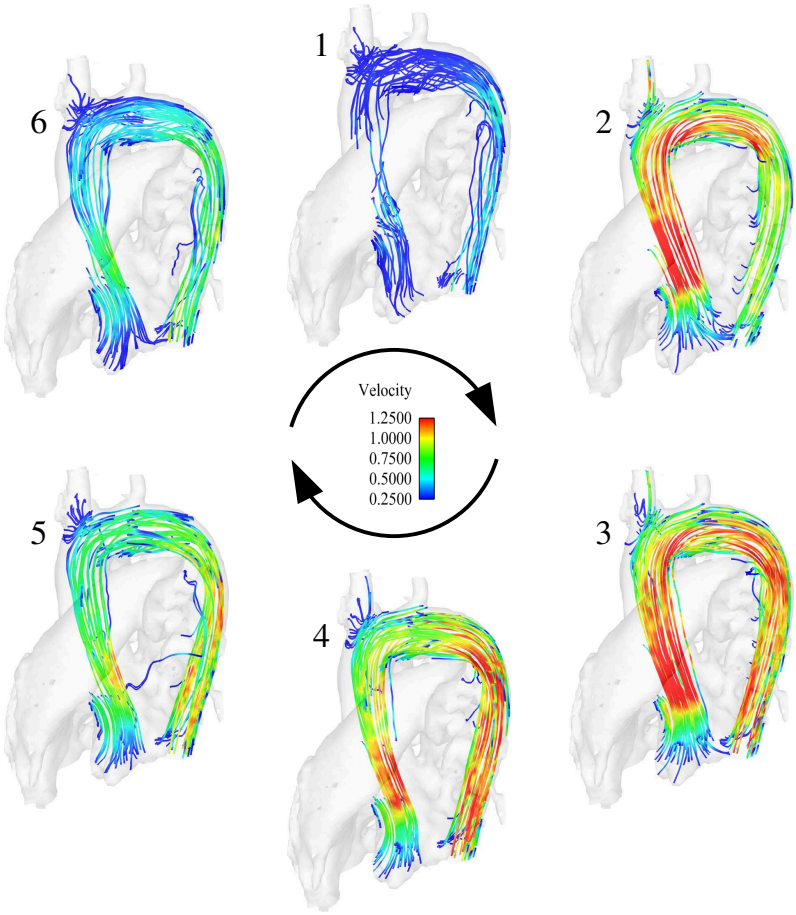

Fig. 4.2. Input velocity field (1.-6.: early to late systole).

Although the pressure estimation approach presented in this work can be independently applied to any spatially distributed velocity field, we follow the data-processing steps defined by *Velomap* a Matlab (The MathWorks, Inc.) based pre-processing tool developed by the Diagnostic Radiology Department, University of Freiburg, Germany. Figure 4.2 represents the 4D flow field at different time-frames of the cardiac cycle as the starting point of the later pressure estimation process.

Flow Field Mapping:

The methodology for providing a correct pressure estimation result has been implemented in the open source software environment OpenCMISS, described in Section 3.3, and applied to clinically relevant test cases (Krittian et al. (2011)). The pressure estimation theory is based on the continuum mechanics principles of mass and momentum conservation. The underlying equations can be used to derive and discretise the *PPE* foundations needed for the pressure estimation process presented. In order to mathematically describe the relative pressure caused by the dynamic, three-dimensional, viscous and often highly complex character of cardiovascular blood flow, we need to consider the complete formulation of the dynamic, incompressible, and viscous Navier-Stokes equations:

$$\rho \left(\frac{\partial \boldsymbol{v}}{\partial t} + (\boldsymbol{v} \cdot \nabla)\boldsymbol{v} \right) = \boldsymbol{f} - \nabla p + \mu \triangle \boldsymbol{v}. \tag{4.1}$$

By transforming a given incompressible flow field $\boldsymbol{v}$ into the corresponding pressure distribution p, we expect the velocity field to satisfy the divergence-free condition $\nabla \cdot \boldsymbol{v} \stackrel{!}{=} 0$. Following *Newton's second law*, the relative pressure distribution can be seen as a consequence of transient and convective momentum, viscous resistance and volume forces. In this case, the only unknown for the Navier-Stokes equations set is represented by the pressure gradient. However, obtaining a pressure distribution from its gradient is not straight-forward. In order to include smoothing options and to avoid boundary condition sensitivities, we have chosen to start with a higher-order pressure derivative which yields the *PPE* problem as follows:

$$\triangle p = \nabla \cdot \boldsymbol{b}. \tag{4.2}$$

with

$$\boldsymbol{b} = \boldsymbol{f} + \mu \triangle \boldsymbol{v} - \rho \left(\frac{\partial \boldsymbol{v}}{\partial t} + (\boldsymbol{v} \cdot \nabla)\boldsymbol{v} \right). \tag{4.3}$$

In order to solve for cardiovascular pressure fields, especially *finite difference approaches* have been used in the past driven by so-called *Neumann boundary conditions*, which are often sensitive and hard to determine. In this section we want to highlight the advantages of the finite element technique for discretising the PPE problem within the cardiovascular pressure estimation process.

We introduce a *specialised mapping approach* to the field of cardiovascular pressure estimation, driven by volume sources rather than surface fluxes. This not only avoids the usage of gradient boundary conditions but also allows a reduction of the computational domain. We start with the weak formulation of Equation (4.2) which is obtained by multiplication by the finite element

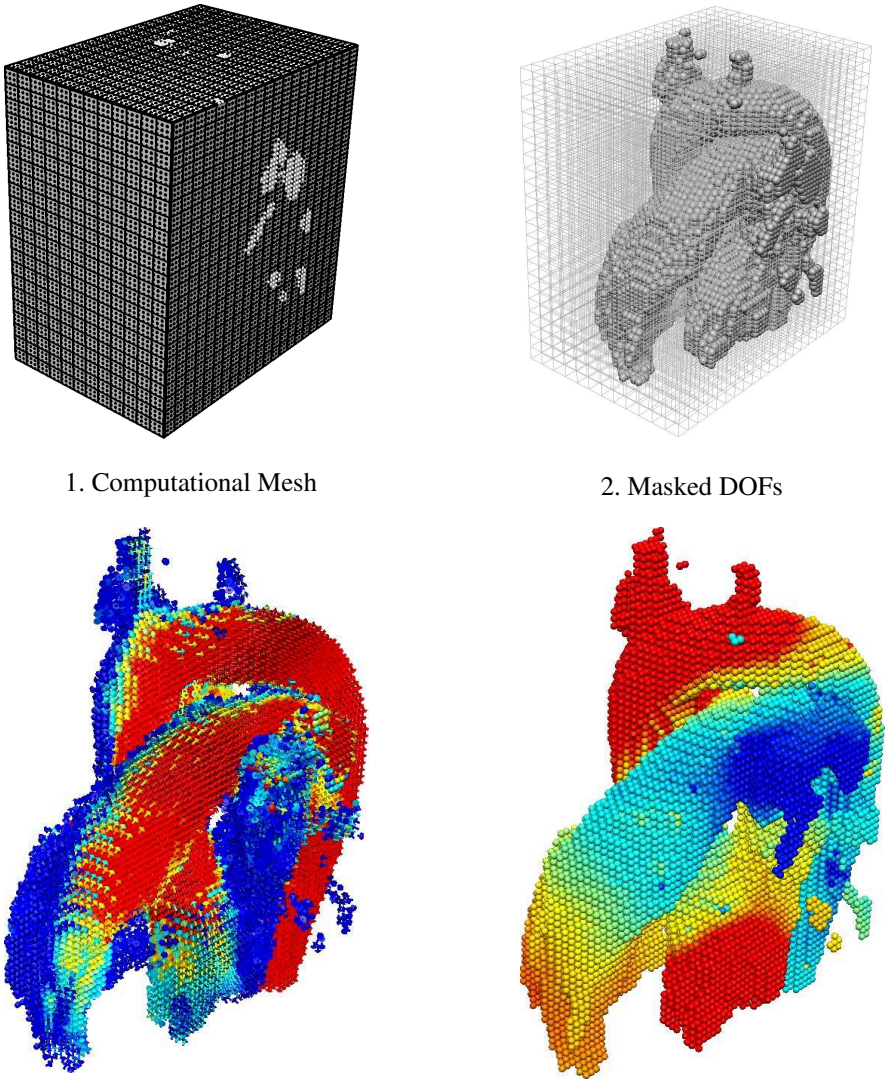

Fig. 4.3. Data processing from imaging space to pressure evaluation *(red - high magnitude, blue - low magnitude).*

test function φ and subsequent integration over the computational domain Ω

$$\int_{\Omega} (\nabla \cdot \nabla p)\, \varphi \; d\Omega = \int_{\Omega} (\nabla \cdot \boldsymbol{b})\, \varphi \; d\Omega. \tag{4.4}$$

An advantage for the pressure estimation approach is now based on applying *Gauss' theorem* to both the left-hand and right-hand side of Equation (4.4). This allows the elimination of surface integrated terms and we can thus formulate our fundamental finite element *PPE* equation. Following this approach, the resulting pressure is driven only by its source term distribution and no boundary gradients need to be applied

$$\int_{\Omega} \nabla p \cdot \nabla \varphi \; d\Omega = \int_{\Omega} \boldsymbol{b} \cdot \nabla \varphi \; d\Omega. \tag{4.5}$$

The scalar function φ represents the finite element test functions. The left-hand side of Equation (4.5) results in a stiffness matrix $\boldsymbol{K}$, the right-hand side into a source vector $\boldsymbol{s}$. For the general purpose of cardiovascular pressure estimation, we characterise the embedded velocity fields by introducing the element-based labelling factor κ into Equation (4.5) which yields:

$$\tilde{K}_{mn} p_n = \kappa s_m, \tag{4.6}$$

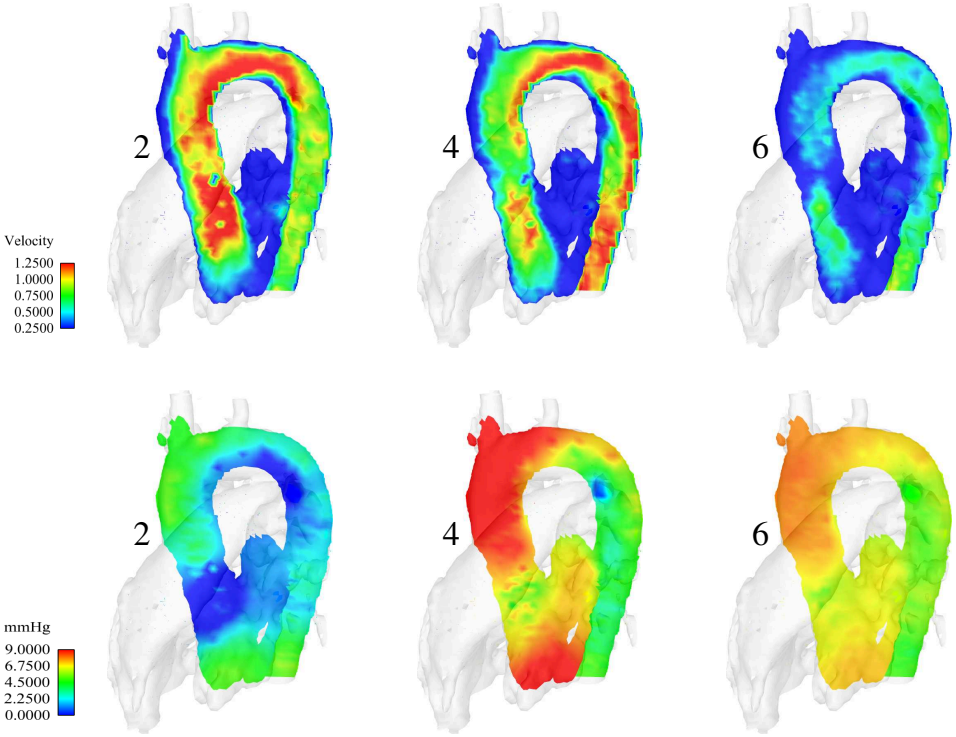

Fig. 4.4. Velocity and pressure magnitudes on cutting planes (1.-6.: Early to late systole).

where

$$\tilde{K}_{mn} = \int_{\Omega} \kappa \left(\nabla p \cdot \nabla \varphi \right) d\Omega, \tag{4.7}$$

Assuming a velocity screen procedure that results in a discretised domain Ω containing both the fluid domain of interest Ω_{int} and the surrounding area Ω_{ext}, we can now use κ to perform the *PPE* computation without extra segmentation or mesh adaptation where $\kappa = 1$ on Ω_{int} and $\kappa = 0$ on Ω_{ext}. Masking information may be treated as piecewise constant or, alternatively, evaluated and scaled with $0 < \kappa < 1$. This avoids the propagation of Ω_{int}-source signals to Ω_{ext} and any external influence from Ω_{ext} on Ω_{int}.

Non-invasive Pressure Estimation:

Figure 4.3 shows the workflow summary as a graphical abstract. As a first step, the computational mesh is derived directly from the MR imaging space resolution (1.). Directly from the 4D flow information the inside/outside masking can be performed allowing a clear separation of fluid domain and surrounding areas (2.). The identified velocity field (3.) can then be used to calculate the relative pressure field information (4.) over the whole cardiac cycle. This information can now be fed back to fluid-solid coupled computational approaches in order to allow for more realistic pressure boundary conditions. To date, this represents a unique way to identify pressure fields in a non-invasive manner. Figure 4.4 shows the corresponding velocity and pressure fields and emphasizes the value of non-invasive pressure information in order to classify both healthy and abnormal cardiovascular pressure distributions.

5 Discussion

Cardiovascular diseases are among the most frequent diseases of modern civilization. In 2010, in Germany alone, 400000 people died as a consequence of diseases of the cardiovascular system. Depending on the severity of the disease, the medical treatment of cardiac diseases ranges from medical treatment to surgical intervention, whether it is minimally invasive with catheters or heart surgery on a beating heart, up to replacement of a diseased heart with a transplant. However, there are not enough donor hearts available to treat patients, so that fluid mechanical supplementary systems for the heart are necessary to bridge the gap. Alternatively, organ-retaining cardiac surgery with reconstruction of a ventricle is also carried out. In the framework of the international STICH study (**S**urgical **T**reatment of **I**schemic **H**eart Failure), Doenst et al. (2009), it is being investigated if the reconstruction of a ventricle offers a survival advantage compared to conventional cardiac therapy. With this study, for the first time, the KaHMo heart model is used together with MRT, CT and ultrasonic diagnostic methods for therapy planning and fluid mechanical evaluation of cardiac surgery.

5.1 Model Conclusions

The cause of an increase in the left human ventricle is, as already described, a lack of blood flow through the coronary vessels because of deposits, particularly in the branchings of the coronary arteries. Figure 5.1 shows the front view of the coronary arteries, through which 4% of the blood of the systemic circulation flows, as well as the regions of the ventricle myocardium disrupted by a heart attack. The ischemic regions of the myocardium, which are undersupplied with oxygen, are shown in white. The necrotic regions, in which the muscle cells of the myocardium have died and become scarred over, are shaded gray; these do not contribute to the contraction of the ventricle. During polarization of the myocardium, the picture of a healthy ECG known from Figure

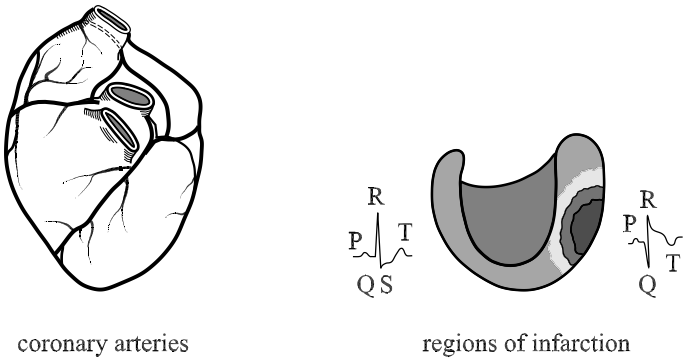

Fig. 5.1. Coronary arteries and heart attack regions of the left ventricle

2.3 is replaced by a negative T-wave. The effect of this is that, during repolarization in the subendocardial regions, a field strength vector arises, directed outwards in the opposite direction, and this generates a positive T-wave in the ECG.

The scarred, dead, necrotic regions of the myocardium do not take part in the pumping work of the ventricle. Therefore in order to be able to maintain the supply for the circulation, the heart reacts with an increase in the pump volume. In the course of time the ventricle increases in size to such a degree that it no longer fits in the chest cavity and must be operated on. The usual surgical method is *ventricular reconstruction*, which is medically evaluated in the STICH study mentioned above. One evaluation criterion is that approximately the flow of the healthy heart shown in Figure 4.22 is found, with flow losses as small as possible, after the ventricular reconstruction at a smaller ventricle volume.

Figure 5.2 shows plastic models of the left ventricle with the muscle fiber orientations of Figure 5.1, as well as sketches of the associated ventricle volumes. The left-hand picture shows the healthy conical ventricle with spiral-shaped

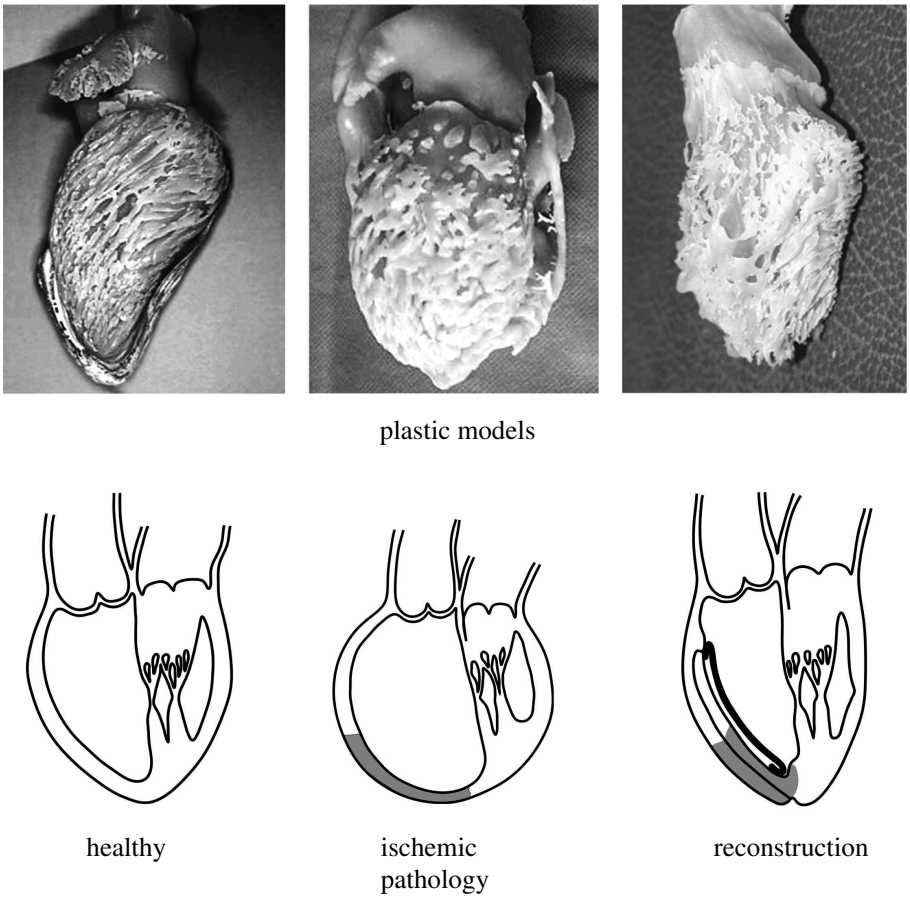

Fig. 5.2. Plastic models of the left ventricle and sketches of the ventricle volume

fiber orientation of the muscle cells. The ischemic pathological ventricle, which has formed a bulging of the myocardium together with an aneurysm, indicates an intensified horizontal fiber orientation, which is partially reversed in surgical ventricular reconstruction. In ventricular reconstruction a part of the ischemic tissue is removed and joined with a so-called patch to create again a conical ventricle, now reduced in size. The individual phases of such ventricular reconstruction are shown in Figure 5.3. Before every ventricular reconstruction, the heart surgeon must consider which ventricle geometry would be most suitable for the given ischemic and necrotic regions of the myocardium to maintain the circulation. In addition to reconstruction of the myocardial muscle fiber layers, the flow in the ventricle is of main concern. The KaHMo heart model is used prior to the planning of a cardiac operation and the fluid mechanical evaluation of the results of surgery. A shaper, as shown in the lower Figure 5.3, is generally used for ventricular reconstruction, whose flow is calculated with KaHMo FSI.

Figure 5.4 shows the geometry of the shaper, which has a volume of 120 ml. The flow-structure coupled fluid calculation of Figure 5.5 shows that all characteristics of the healthy ventricle of Figure 4.22 have been achieved. Therefore

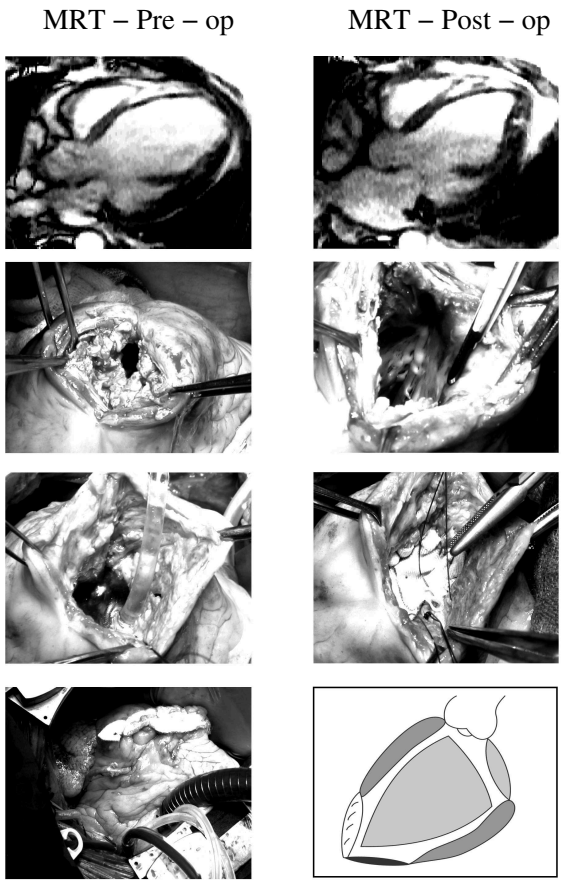

Fig. 5.3. Ventricular reconstruction, Doenst et al. (2009)

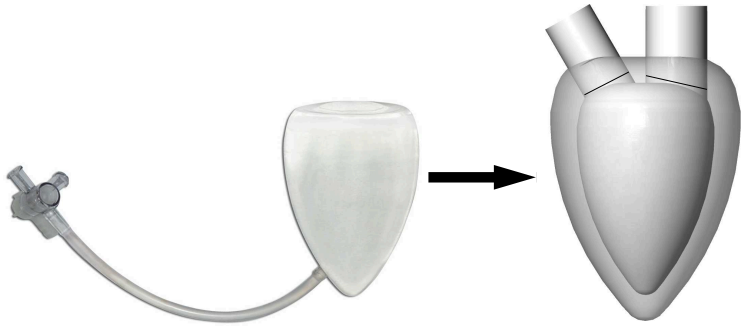

Fig. 5.4. Geometry of the shaper

a ventricular reconstruction with the given shaper geometry is the more efficient solution from a fluid-mechanical point of view.

In addition to the characteristic quantities of the dimensionless Navier-Stokes equation (3.4), Re_D and Wo are defined as further dimensionless characteristic numbers for the medical evaluation of the ventricle flow. The ejection fraction

$$E = \frac{V_\mathrm{s}}{V_\mathrm{d}} \tag{5.1}$$

is the ratio of the stroke volume V_s to that of the end-diastolic volume V_d. It indicates the percentage of the ventricle volume expelled into the aortic channel. In a healthy heart $E = 62\%$.

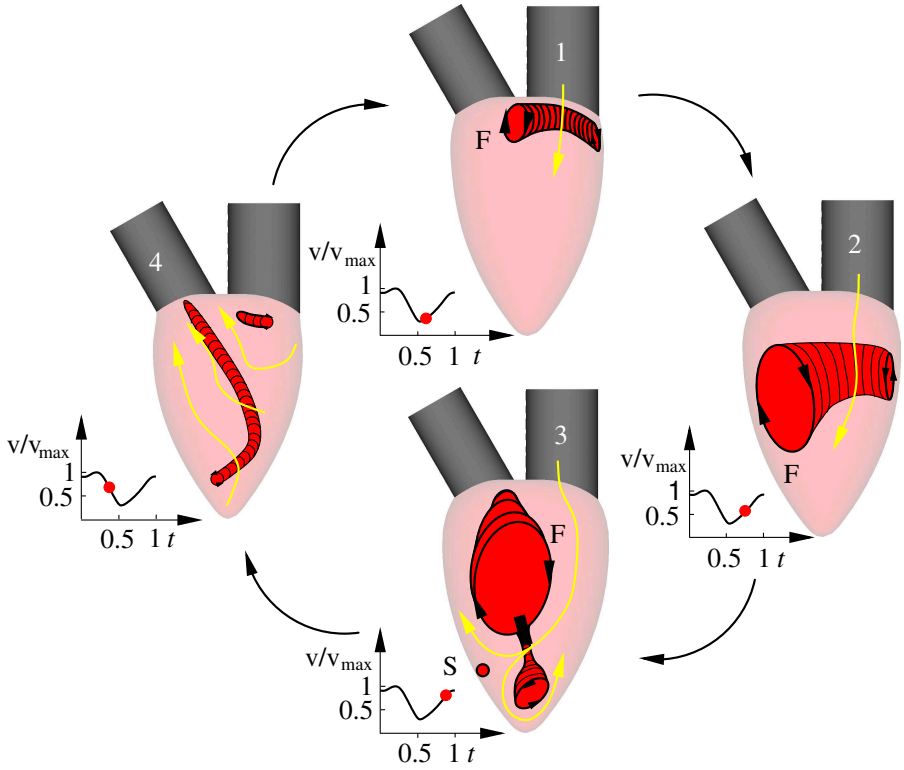

Fig. 5.5. Three-dimensional flow structure in the shaper

Another way of characterizing the flow in the ventricle is by means of the mixing parameter M of the blood in the ventricle.

$$M = (1 - \mathrm{E})^n \quad . \tag{5.2}$$

E is the ejection fraction (5.1) and n is the number of cardiac cycles that must pass until the blood in the ventricle is fully exchanged. In the simulations, a scalar is initialized at the mitral valve to represent the mixing of the old blood in the ventricle with the new blood flowing in.

The values for the patient-specific data sets of Section 4.3 are set out in Tables 3.2 and 3.3.

With the ventricle pumping work A_p, which is calculated from the p-V diagram of Figure 4.21, the mixing time of the blood in the ventricle t_b in general over $2 - 3$ pump cycles, the effective viscosity of the blood μ_eff (2.5) and the stroke volume V_s, a dimensionless pumping work can be defined:

$$O = \frac{A_\mathrm{p} \cdot t_\mathrm{b}}{\mu_\mathrm{eff} \cdot V_\mathrm{s}} \quad , \tag{5.3}$$

where $A_\mathrm{p} \cdot t_\mathrm{b}/\mu_\mathrm{eff}$ has the dimension of a volume and O is a ratio of volumes. If the patient has suffered a heart attack, the pumping work of the ventricle decreases and the mixing time of the blood increases. The dimensionless pumping work assumes larger values than those of a healthy heart.

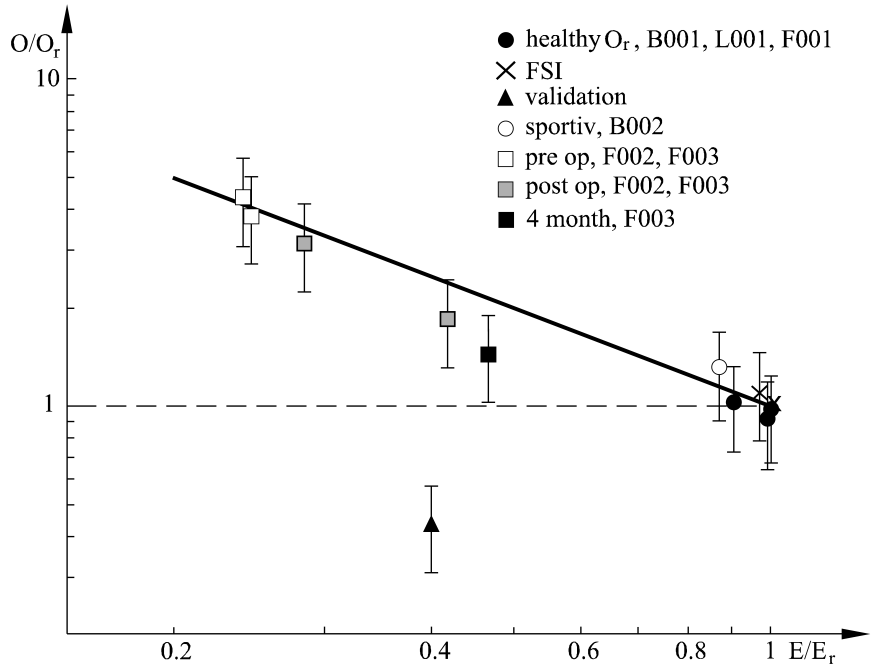

Fig. 5.6. Dependence of dimensionless pumping work O/O_r on the ejection fraction E/E_r, reference values $O_\mathrm{r} = 34 \cdot 10^6$, $E_\mathrm{r} = 62\%$

Figure 5.6 plots the dimensionless pumping work O relative to the reference value of the healthy ventricle O_r for the patients with aneurysm, before and after ventricular reconstruction and after four months' regeneration time, over the ejection fraction E, relative to the reference value E_r, respectively the Womersley number W_O or the Reynolds number Re_D. On a plot, with logarithmic scales on both axes a straight line is found, with the linear power law

$$\frac{O}{O_\mathrm{r}} = \left(\frac{E}{\mathrm{E_r}}\right)^{-1} \quad . \tag{5.4}$$

The heart of an athlete also has an increased value of the dimensionless pumping work and is approximately the value of the regenerated operated ventricle. As the diagram in Figure 5.6 shows, with the dimensionless pumping work and the power law (5.4), a quantitative fluid mechanical evaluation can be carried out for a patient before and after surgery. In this it is assumed that the Womersley number Wo is approximately constant.

5.2 Outlook & Further Developments

Further development of the KaHMo FSI heart model for patient-specific application requires the adaptation of the structure modelling of the myocardium and further development of the fiber bound model. The material model must take into account regions locally damaged by heart attack. The degree of detail of the KaHMo FSI heart model ranges from the modelling of the layer composition and the fiber orientation to the investigation of the passive and active behavior of material. Even biochemical (O_2 saturation) and electrophysiological points of view are taken into account on the path to a unified model of the heart.

The material law used in the framework of the existing, transversal isotropic fiber bound model will be modelled anisotropically and thus will take account of the three-dimensional layer composition of the myocardium. In addition, computational routines developed will permit the extension, which until now has been specified globally, to be influenced locally, or its activation potential to be included upstream in the routine. The necessary temporal influencing takes place by means of the inclusion of extended user-defined routines. This leads to new interfaces, such as the need to take into account the O_2 saturation. The influence of locally dead regions, which can be analyzed already today, can be extended continuously and continually. With this consideration it is justified to extend a hybrid contraction model that reflects the phenomenon of wall thickening better, and thus permits a corrected rendering of the stress distribution in the myocardium wall. The entirety of the passive and active material properties thus follow as before with the energy function $W = W_\mathrm{passive} + W_\mathrm{active}$.

The anisotropic extension of the passive material law is accompanied by the similarly anisotropic active contraction. Estimation of the inertial effects of the flow and structure requires that this enhancement be limited to the modelling and simulation of the flow.

Using MRT imaging methods such as MRT tagging, a diffusion method or the tissue phase mapping method, further patient-specific data are available, which can be directly included in the extended structure model. Thanks to the partitioned modelling of KaHMo FSI it is possible to integrate individual elements into the existing model without further complications.

Analysis of the flow pictures, such as that of Figure 4.25, shows that the vortex formation in the aortic channel is over-emphasized in the current KaHMo models. Further development of the mitral flap model projected onto the valve plane is necessary. The valve flaps controlled passively by the pressure are also calculated in a flow-structure coupled manner. They follow the flow approximately, and are not influenced by the structure inertia, and close the aortic channel partially during the diastole;a consequence of this is a dominance of the asymmetric intake vortex in the ventricle.

Whereas 4D flow information are generally accessible, there has been no systematic way of immediate calculation of the corresponding pressure field. To our knowledge, this is the first time that measured velocity data have been used to identify volume source distributions that in return represent the driving force of an underlying pressure estimation process. The methodology developed is in good agreement with state-of-the-art verification studies published elsewhere. In terms of current model limitations we want to distinguish between potential improvements both data-based and methodological. Only high-quality data input results in accurate representation of corresponding pressure fields. Certain limits of noise can be restrained by projection enhancement techniques but require more sophisticated analysis in future.

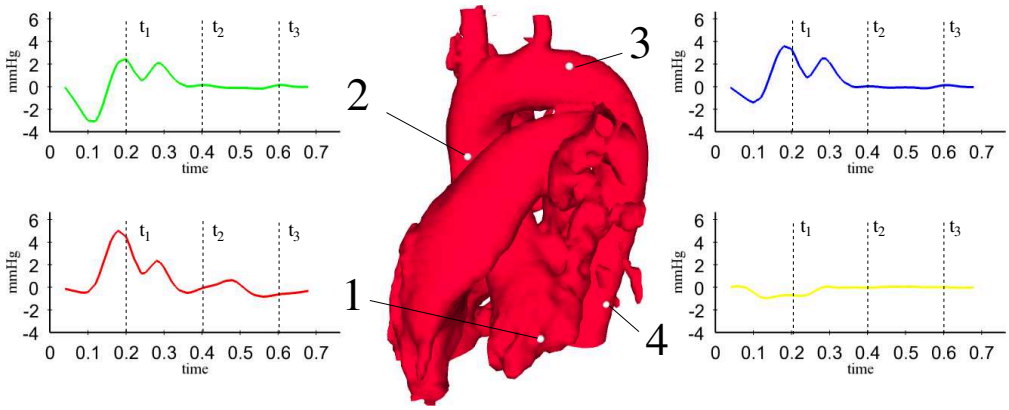

Fig. 5.7. Local relative pressure dynamics (1.-6.: Early to late systole).

In order to support the quality of incoming data, additional features have been integrated successfully such as the enforcement of the divergence-free state or the projection on a *C1* continuous space. The divergence-free condition of the velocity field is of the utmost importance, in both theoretical and computational fluid dynamics. Any divergence-free velocity field induces a computable pressure field which ensures a divergence-free acceleration, which is then also computable. Future work will focus on the validation of our approach based on MR phantom studies as well as combined 4D flow and pressure catheter measurement data. More sophisticated projection methods will give more insight into imaging data quality and flow-sensitive 4D flow conservation in particular. The methodology as well as the first real-world application on a healthy human dataset represent an important step towards patient-specific pressure evaluation. This process is not only important for direct evaluation of respective health conditions but also provide indirect input to more sophisticated multi-physics analysis.

Moreover, Figure 5.7 shows the potential value of relative pressure estimation not only to enhance existing computational approaches but also directly as subject-specific analysis tool. The level of relative pressure field can also take place in future dimensionless parameters that can now be defined.

To simulate the patient-specific flow in the heart with the motion of the KaHMo MRT heart model prescribed, the images of one cardiac cycle from an MRT tomography are used. Extraction of the fluid space surfaces for each of the 20 phases is carried out using a semi-automatic segmentation program. The software uses a medium heart model, which consists of many triangular surface cells. This is manually adapted to the gray values of the DICOM data for the first phase and after that automatically seeks the boundaries of the fluid space for all further phases. In this manner 20 surface grids of atrium and ventricle are found, which describe the motion of the heart.

In order to be able to specify this motion in the simulation software, the topology of the computational grid in each phase must be identical to that in the others. This means that information about the neighborhood between calls and nodes remains the same. Thus it becomes possible to approximate the volume change by means of a shifting of the nodes.

Further development of the software packet for unstructured volume grids with a remeshing option would permit the volume of the heart to be linked with tetrahedral cells and the motion to be realized only by means of topologically identical triangular surface grids. On the one hand this opens new possibilities for further development with respect to precision of detail and a modular construction. On the other hand it provides a direct interface to semi-automatic segmentation, as the extracted surfaces already consist of topologically iden-

tical triangular cells.

However, at present these are still too rough for the generation of the volume grid and are too imprecise in the flap and atrium regions, so that they cannot be directly implemented into the software and so must be manually adapted. On the one hand this affects the precision of the data and on the other hand the time needed to prepare such a set of data is very great. In the future, efforts will be made to improve the segmentation tool to a finer triangulation of the surface and to avoid artifacts and cell overlapping, corresponding to the quality criteria provided by the software program. This permits the KaHMo heart model to be integrated in a completely automatized manner into the MRT tomography and provides cardiologists and cardiac surgeons with a complete packet.

Acknowledgements

This work was made possible by the enthusiastic collaboration of T. Schenkel, S. Donisi, M. Reik, M. Malvè, K. Spiegel, M. Perschall, S. Höttges, S. Ruck and M. Mühlhausen of the Institute for Fluid Mechanics at the University of Karlsruhe. We appreciate the support of B. Jung, S. Flacke, A. Kovacs and S. Nitzsche for taking the MRT images at the University Hospitals of Freiburg, Bonn and Leipzig, as well as H. Barschdorf and C. Lorenz for converting the images at the Philips Research Laboratories Hamburg. D. Liepsch and T. Schmid are thanked for carrying out the validation experiment at Munich University of Applied Sciences. The authors would also like to acknowledge their collaboration with F. Beyersdorf from the Department of Cardiovascular Surgery at the University Hospital Freiburg, W. Schiller from the Department of Cardiovascular Surgery at the University Hospital Bonn, and T. Doenst from the Department of Cardiovascular Surgery at the University Hospital Leipzig, who provided important impulses with their medical advice.

Furthermore, the authors want to express their gratitude to all the people who have contributed to the OpenCMISS project (www.opencmiss.org) during the last couple of years. The tools developed represent valuable input to the whole computational cardiology community and KaHMo in particular. Among others we want to mention the input from P. Hunter and C. Bradley (Auckland Bioengineering Institute) and N. Smith (University of Oxford and King's College London). The non-invasive pressure estimation was kindly supported by 4D flow input from M. Markl (University of Freiburg) and P. Kilner (Imperial College and Royal Bromption Hospital London).

K. Asfaw, S. Hasecic and K. Fritsch-Kirchner are thanked for the manuscript work. Part of this work was supported by the Deutsche Forschungsgesellschaft, DFG grant number Oe 86-24.

References

Baccani, B., Domenichini F., Pedrizzetti, G., 2003. *Model and influence of mitral valve opening during the left ventricular filling*. J. Biomech., **36**, 335-361

Baccani, B., Domenichini F., Pedrizzetti, G., 2002. *Vortex dynamics in a model left ventricle during filling*. Eur. J. Mech. B/Fluids, **21**, 527-543

Baccani, B., Domenichini F., Pedrizzetti, G., Tonti, G., 2002. *Fluid dynamics of the left ventricular filling in dilated cardiomyopathie*. J. Biomech., **35, 5**, 665-671

Bradley C., Bowery A., Britten R., Budelmann V., Camara O., Christie R., Cookson A., Frangi A., Gamage T.B., Heidlauf T., Krittian S., Ladd D., Little C., Mithraratne K., Nash M., Nickerson D., Nielsen P., Nordbø Ø., Omholt S., Pashaei A., Paterson D., Rajagopal V., Reeve A., Röhrle O., Safaei S., Sebastián R., Stegöfer M., Wu T., Yu T., Zhang H., Hunter P., 2011. *OpenCMISS: A multi-physics & multi-scale computational infrastructure for the VPH/Physiome project* . Prog Biophys Mol Biol., submitted

Cheng, Y., Oertel, H., Schenkel, T., 2004. *Fluid-structure coupled cfd simulation of the left ventricular flow during filling phase*. Ann. Biomed. Eng., **33(5)**, 567-576

Dijkstra E.W., 1959. *A Note on Two Problems in Connexion with Graphs*. Num. Math., **1**, 269–271

Doenst T., Spiegel K., Reik M., Markl M., Hennig J., Nitzsche S., Beyersdorf F., Oertel H., 2009 *Fluid-Dynamic Modelling of the Human Left Ventricle – Metholology and Application to Surgical Ventricular Reconstruction. Fluid-structure coupled cfd simulation of the left ventricular flow during filling phase*. Ann. Thoracic. Surg., **87**, 1187-1195

Domenichini F., Pedrizzetti G., Baccani B., 2005 *Three-dimensional filling flow into a model left ventricle*. J. Fluid Mech., **539**, 179–198

Ecabert O., Smith, N., 2008. *euHeart: integrated cardiac care using patient-specific cardiovascular modeling - A project based on biophysics aims to improve the diagnosis, planning, and treatment of cardiovascular disease.*. Biomedical Optics & Medical Imaging, SPIE Newsroom. DOI: 10.1117/2.1200804.1126

Fung Y.C., 1997. *Biomechanics: Circulation*. 2nd edn., Springer-Verlag, Berlin, Heidelberg, New York.

Glass L., Hunter P., McCulloch A., 1991. *Theory of Heart: Biomechanics, Biophysics, and Nonlinear Dynamics of Cardiac Function*. Springer-Verlag, Berlin, Heidelberg, New York.

Guyton A.C., Coleman T.G., Granger H.J., 1972. *Circulation: Overall Regulation*. Ann. Rev. Physiologie, **34**, 13–46

Handke M., Jahnke C., Heinrichs G., Schlegel J., Vos C., Schmitt D., Bode C., Geibel A., 2003. *New Three-Dimensional Echocardiographic System Using Digital Radiofrequency Data-Visualization and Quantitative Analysis of Aortic Valve Dynamics With High Resolution*. Circulation, **107**, 2876–2879

Holzapfel G., Gasser T., Ogden R., 2000. *A New Constitutive Framework for Arterial Wall Mechanics and a Comparative Study of Material Models*. J. of Elasticity, **61**, 1–48

Houlind K.C., Sloth E., Oyre S., Kim W.Y., Pedersen E.M., Jorgensen H.S., Hasenkam J.M., 1994 *Three-dimensional visualization of velocity profiles in the human main pulmonary artery with magnetic resonance phase-velocity mapping*. American Heart Journal, **128**, 1130–1138

Hunter P.J., McCulloch A.D., ter Keurs H.E.D.J., 1998. *Modelling the Mechanical Properties of Cardiac Muscle*. Progr. in Biophysics and Molecular Biology, **69**, 289–331

Hunter P.J., Nash M.P., Sands G.B., 1996. *Computational Electromechanics of the Heart*. In: Computational Biology of the Heart. Eds. Panfilov A.V., Holden A.V., John Wiley & Sons, Chichester, New York, 345–407

Hunter P.J., Smaill B.H., Nielsen P.M.F., LeGrice I.J., 1996. *A Mathematical Model of Cardiac Anatomy*. In: Computational Biology of the Heart. Eds. Panfilov A.V., Holden A.V., John Wiley & Sons, Chichester, New York, 171–215

Jones T.N., Netaxas D.N., 1998. *Patient-specific analysis of left ventricular blood flow*. Computer Science 1496, Springer Verlag, 154–166

Jung B., Kreher, B., Markl, M., Henning, J., 2006. *Visualization of Tissue Velocity Data from Cardiac Wall Motion Measurements with Myocardial Fiber Tracking*. European J. of Cardio-Thoracic Surgery, **29**, 158-164

Kilner P.J., Yang G.-Z., Wilkes A.J., Mohiaddin R.H., Firmin D.N., Yacoub M.H., 2000. *Asymmetric redirection of flow through the heart*. Nature, **404**, 759–761

Kim W.Y., Walker P.G., Pedersen E.M., Poulsen J.K, Oyre S., Houlind K., Yoganathan A.P., 1995. *Left ventricular blood flow patterns in normal subjects: A quantitative analysis by three-dimensional magnetic resonance velocity mapping*. JACC, **26**, 224–238

Krittian S., 2009. *Modellierung der kardialen Strömung-Struktur-Wechselwirkung*. PhD Thesis, Karlsruhe Institute of Technology / University of Karlsruhe (TH)

Krittian S., Oertel H., Janoske U., Böhlke T., 2010. *Partitioned fluid-solid coupling for cardiovascular blood flow: left-ventricular fluid mechanics*. Ann Biomed Eng., **38(4)**, 1426-1441

Krittian S., Schenkel T., Janoske U., Oertel H., 2010. *Partitioned fluid-solid coupling for cardiovascular blood flow: validation study of pressure-driven fluid-domain deformation*. Ann Biomed Eng., **38(8)**, 2676-2689

Krittian S., Bock J., Michler C., Nordsletten D., Bradley C., Lamata P., Pitcher A., Kilner P., Markl M., Smith N., 2011. *A finite-element approach to the direct computation of relative cardiovascular pressure from time-resolved MR velocity data*. Med Image Anal., submitted

Laurien E., Oertel H., 2011. *Numerische Strömungsmechanik*. 4th edn., Vieweg + Teubner Verlag, Wiesbaden

Lemon J.D., Yoganathan A.P., 2000. *Three-Dimensional Computational Model*

of Left Heart Diastolic Function with Fluid-Structure Interaction. J. of Biomech. Eng., **122**, 109–117

Liepsch D., Moravec S., Baumgart R.,1992. *Some flow visualization and laser-doppler velocity measurements in a true-to-scale elastic model of a human aortic arch — A new model technique*. Biorheology, **29**, 563–680

Long Q., Merrifield R., Yang G.-Z., Xu X.Y., Killner P.J., Firmin D.N., 2003. *The influence of inflow boundary conditions on intra left ventricle flow predictions*. J. of Biomech. Eng., **125**, 922–927

McQueen D.M., Peskin C.S., 2001. *Heart Simulation by an Immersed Boundary Method with Formal Second Order Accuracy and Reduced Numerical Viscosity*. In: Mechanics for a New Millennium, Proceedings of the 20th ICTAM, Chicago, Illinois. Eds. Aref H., Phillips, J.W., Kluwer Academic Publishers, Dordrecht, Norwell, Massachusetts

Mortensen E.N.,Barrett W.A., 1998. *Interactive Segmentation with Intelligent Scissors*. Graphical Models and Image Processing, **60**, **5**, 349–384

Mühlhausen M.P., 2011. *Strömung-struktur-gekoppelte Modellierung und Simulation des menschlichen Herzens*. PhD Thesis, Karlsruhe Institute of Technology

Nakamura M.S., Wada T., Mikami A., Kitabatake, Karino T., 2003. *Computational study on the evolution of an intraventricular vortical flow during early diastole for the interpretation of color m-mode doppler echocardiogramms*. Biomech. Model. Mechanobiol., **2**, **1**, 59–73

Nash M. P., Hunter P.J., 2000. *Computational mechanics of the heart*. J. of Elasticity, **61**, 113–141

Naujokat E., Kiencke U., 2000. *Neuronal and Hormonal Cardiac Control Processes in a Model of the Human Circulatory System*. Int J. of Bioelectromagnetism, **2**, **2**, 1–7

Nordsletten D., Kay D., Smith N., 2009. *A non-conforming monolithic finite element method for problems of coupled mechanics*. J. Comput. Phys., **229(20)**, 7571-7593

Nordsletten D.A., Niederer S.A., Nash M.P., Hunter P.J., Smith N.P., 2010 *Coupling multi-physics models to cardiac mechanics*. Prog Biophys Mol Biol., **104(1-3)**, 77-88

Nordsletten D., McCormick M., Kilner P.J., Hunter P., Kay D. and Smith N.P., 2011. *Fluidsolid coupling for the investigation of diastolic and systolic human left ventricular function*. Int J. Numer. Method. Biomed. Eng., **27**

Oertel H., 2004. *Biofluid Mechanics of Blood Circulation*. In: Prandtl Essentials of Fluid Mechanics. Ed. Oertel H., Springer-Verlag, New York

Oertel H., 2009. *Biofluid Mechanics*. In: Prandtl Essentials of Fluid Mechanics. Ed. Oertel H., Springer-Verlag, New York

Oertel H., 2008. *Bioströmungsmechanik*. In: Prandtl Führer durch die Strömungslehre. Ed. Oertel H., Vieweg + Teubner Verlag, Wiesbaden

Oertel H., Ruck S., 2011. *Bioströmungsmechanik*. 2nd edition, Vieweg + Teubner Verlag, Wiesbaden

Oertel H., 2005. *Modelling the Human Cardiac Fluid Mechanics*. 1st edn.,

University Press, Karlsruhe
Oertel H., Spiegel K., Donisi S., 2006. *Modelling the Human Cardiac Fluid Mechanics*. 2nd edn., University Press, Karlsruhe
Oertel H., Krittian S.B.S., Spiegel K., 2009. *Modelling the Human Cardiac Fluid Mechanics*. 3rd edn., University Press, Karlsruhe
Oertel H., Böhle M., Reviol T., 2011. *Strömungsmechanik*. 6th edn., Vieweg + Teubner Verlag, Wiesbaden
Pedrizzetti G., Domenichini F., 2005. *Nature optimizes the swirling flow in the human left ventricle*. Physical Review Letters., **95**
Perktold K., Resch M., Florian H., 1991. *Pulsatile non–Newtonian Flow Characteristics in a Three-dimensional Human Carotid Bifurcation Model*. J. of Biomech. Eng., **113**, 464–475
Peskin C.S., McQueen D.M., 1997. *Fluid Dynamics of the Heart and its Valves*. In: Case Studies in Mathematical Modeling — Ecology, Physiology, and Cell Biology. Eds. Othmer H.G., Adler F.R., Lewis M.A., Dallon J.C., Prentice-Hall, Englewood Cliffs, New Jersey, 309–337
Pullan A.J., Buist M.L., Cheng L.K., 2005. *Mathematically modelling the electrical activity of the heart*. World scientific
Reik M., Meyrowitz G., Schwarz M., Donisi S., Schenkel T., 2005 *A 1D circulation model as boundary condition for a 3D simulation of a pumping human ventricle*. JIFMBE Proceedings, EMBEC 2005, Prague
Reul H., Talukder N., Mueller E.W., 1981. *Fluid mechanics of the natural mitral valve*. J. of Biomech. Eng., **14**, **14**,361–372
Robb J. S., Robb R.C., 1942. *The normal heart: Anatomy and Physiology of the Structural Units*. Am. Heart J., **23**, 455–467
Saber N.R., Gosman A.D., Wood N.B., Kilner P.J., Charrier C.L., Firmin D.N.,2001 *Computational flow modeling of the left ventricle based on in vivo mri data: Initial experience*. Ann. Biomed. Eng., **29**, **4**, 275–283
Saber N.R., Gosman A.D., Wood N.B., Merrifield R.D., Yang G.-Z., Charrier C.L., Gatehouse P.D., Firmin D.N.,2003 *Progress towards patient-specific computational flow modeling of the left heart via combination of magnetic resonance imaging with computational fluid dynamics*. Ann. Biomed. Eng., **31**, **1**, 42–52
Schenkel T., Reik M., Malvè M., Markl M., Jung B., Oertel H., 2009 *MRI based CFD analysis of flow in a human left ventricle*. Ann. Biomed. Eng., **37**, **3**, 503-515
Schenkel T., Krittian S., Mühlhausen M.-P., Oertel H., 2010 *Hemodynamics and Fluid-Structure-Interaction in a Virtual Heart*. it - Information Technology, **52(5)**, 250-257
Schmid T., Stock M., Donisi S., Schiller W., Liepsch D., Laschka B., Hirzinger G., Welz A., Oertel H.,2005 *Development and verifikation of ventricle-shaped chambers for the DLR assist device*. Artif. Organs, **28**, **9**, 875
Schmid T., Spiegel K., Balasso A., Stock M., Schenkel T., Liepsch D., Oertel H., Welz A., Schiller W., 2009. *In Vitro Validation of a Numerical Model of Ventricular Flow by Particle Image Velocimetry*. Biorheology J., in prepa-

ration

Smith N., de Vecchi A., McCormick M., Nordsletten D., Camara O., Frangi A.F., Delingette H., Sermesant M., Relan J., Ayache N., Krueger M.W., Schulze W.H.W., Hose R., Valverde I., Beerbaum P., Staicu C., Siebes M., Spaan J., Hunter P., Weese J., Lehmann J., Chapelle D., Rezavi R., 2011. *euHeart: personalized and integrated cardiac care using patient-specific cardiovascular modelling*. Interface Focus, **1(3)**, 349-364

Schwarz R., 2003. *Semiautomatische Segmentierung des linken Herzventrikels für Strömungssimulationen*. Techn. Report, Fraunhofer-Institut für Angewandte Informationstechnik, Sankt Augustin, 1–6

Vierendeels, J., Riemslagh, A., Dick, E., 1999. *Computer simulation of left ventricular filling flow*. Comput. Cardiol., **26**, 177-180

Vierendeels, J., Riemslagh, A., Dick, E., Verdonck, P. 2000. *Computer simulation of intraventricular flow and pressure gradients during diasole*. J. of Biomech. Eng., **122**, 667-674

Walker P.G., Cranney G.B., Grimes R.Y., Delatore J., Rectenwald J., Pohost G.M., Yoganathan A.P.,1996 *Three-dimensional reconstruction of the flow in a human left heart by using magnetic resonance phase velocity encoding*. Ann. Biomed. Eng., **24**, **1**, 139–147

Watanabe H., Hisada T., Sugiura S., Okada J., Fukunari H., 2002. *Computer Simulation of Blood Flow, Left Ventricular Wall Motion and their Interrelationship by Fluid-Structure Interaction Finite Element Method*. JSME, C, **45**, **4**, 1003–1012

Watanabe H., Sugiura H.Sh., Kafuku H., Hisada T.S., 2004. *Multiphysics simulation of left ventricular filling dynamics using fluid-structure interaction finite element method*. Biophysical J., **87**, 2074–2085

ISBN 978-3-86644-794-3